MATERIALS SELECTION AND EVALUATION OF CU-W PARTICULATE COMPOSITES FOR EXTREME ELECTRICAL CONTACTS

A Dissertation
Presented to
The Academic Faculty

By

Bobby Gene Watkins, II

In Partial Fulfillment
Of the Requirements for the Degree
Doctor of Philosophy in Mechanical Engineering

Georgia Institute of Technology

May, 2011

MATERIALS SELECTION AND EVALUATION OF CU-W PARTICULATE COMPOSITES FOR EXTREME ELECTRICAL CONTACTS

Approved by:

Dr. Richard W. Neu, Co-Advisor
George W. Woodruff School of
Mechanical Engineering,
School of Materials Science and
Engineering
Georgia Institute of Technology

Dr. Richard S. Cowan, Co-Advisor
Manufacturing Research Center
Georgia Institute of Technology

Dr. Scott Bair
George W. Woodruff School of
Mechanical Engineering
Georgia Institute of Technology

Dr. Steven Danyluk
George W. Woodruff School of
Mechanical Engineering
Georgia Institute of Technology

Dr. W. Steven Johnson
School of Materials Science and
Engineering,
George W. Woodruff School of
Mechanical Engineering
Georgia Institute of Technology

Date Approved: January 18, 2011

ACKNOWLEDGEMENTS

TABLE OF CONTENTS

LIST OF TABLES

LIST OF FIGURES

Summary

Materials for extreme electrical contacts need to have high electrical conductivity coupled with good structural properties. Potential applications include motor contacts, high power switches, and the components of electromagnetic launch (EML) systems. The lack of durability experienced with these contact materials limits service life. Due to extreme current densities coupled with the local sliding, electrical contact surfaces can degrade due to a one or more wear mechanisms, including adhesive wear and thermally-assisted wear associated with extreme local Joule heating.

A systematic materials selection procedure was developed to identify and compare candidate materials that would be more durable for these types of applications. The most promising materials identified on the Pareto frontier are tungsten alloys. Moreover, several possible candidate monolithic materials as well as hybrid materials that could potentially be even better, filling the "white spaces" on the material property charts, were identified. A couple of these potential candidate materials were obtained and evaluated. These included copper-tungsten W-Cu, "self-lubricating" graphite-impregnated Cu, and Gr-W-Cu composites with different volume fractions of the constituents. The structure-property relations were determined through mechanical and electrical resistivity testing. A unique test protocol for exposing mechanical test specimens to extreme current densities up to 1.2 GA/m^2 was developed and used to evaluate these candidate materials.

The design of materials including optimizing the microstructure attributes for these applications can potentially be accelerated by using micromechanics modeling and other materials design tools coupled with systematic mechanical and tribological

experiments. In this study, physics- and micromechanics-based models were used to correlate properties to the volume fraction of the tungsten. These properties included elastic modulus, hardness, tensile strength, and electrical resistivity. The elastic response of the W-Cu is accurately captured. The yield strength is effectively modeled across the entire range of W volume fraction by taking into account a transition in the dominant strengthening mechanisms with increasing W volume fraction. The electrical conductivity is accurately modeled to within 10% error.

Chapter 1: Introduction

Materials for extreme electrical contacts need to have high electrical conductivity coupled with good structural properties. Potential applications include motor contacts, high power switches, and the components of electromagnetic launch (EML) systems. The lack of durability of these contact materials limits service life. Due to extreme current densities coupled with the local sliding, electrical contact surfaces can degrade due to a one or more wear mechanisms, including adhesive wear and thermally-assisted wear associated with extreme local Joule heating. To understand the nature of these extreme contacts, two of these applications are described in more detail.

1.1 Electromagnetic Launcher

An EML system is comprised of two parallel metal conductors known as rails, and a movable conducting metal armature, as shown in Figure 1 (from Ref. [1]). An electric current is introduced at the end of one of the rails and generates a magnetic field around the rail as the current travels along the length of the rail. The conducting armature provides a conducting path, leading the current back along the second rail. This current also generates a magnetic field that is in the same direction and is added to the field from the first rail. The interaction of the current and the magnetic field produces a force, called the Lorentz force, which is perpendicular to the magnetic field and to the current [2]. This force causes the projectile to speed up as it moves down the rails. The magnitude of the force by which the projectile is accelerated is a function of the amount of current flow through the rails into the projectile.

1
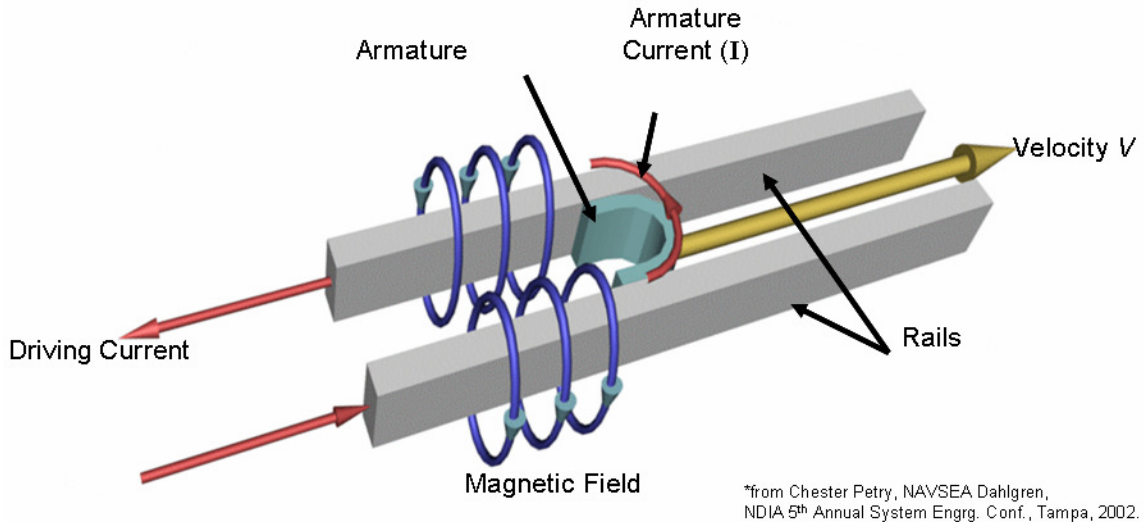
Figure 1: Basic Configuration of Simple Railgun and Projectile [1]

Transient contacts in EM railguns operate under conditions that surpass the limits of desirable metal-metal contact for efficient and reliable performance. Operation parameter levels, such as high current densities approaching 1 GA/m^2, loading, and sliding velocities cause the current carrying capacity of the contacts to be exceeded. The electrical interface "transitions" from a low (<1 volt) to high (>30 volts) voltage contact [2]. Arcing, due to the interface transition, initiates the onset of armature and rail degradation during the launch. The desired 2 km/s sliding velocities in conjunction with high contact pressures needed to prevent arcing give rise to significant frictional effects resulting in heating and wear. This heating, in addition to the Joule heating due to the large current capacities, can lead to loss of structural integrity in EM railgun components. Recent research has also identified contributions to transition by magnetic blow-off forces [1].

Practical EML implementation is severely hindered by the aforementioned undesirable mechanisms associated with EM railgun hypervelocity launches. The effects of these phenomena cause unacceptably short bore life [1], [3]. The bore is detrimentally

affected by the high temperature and high pressure gas that is generated through the plasma medium of electrical conduction [4]. Even in the velocity ranges without transition, the issue of material deposition or transfer must be addressed through the use of materials that possess adequate tribological and mechanical properties (e.g. strength, hardness, electrical and thermal conductivity, corrosion resistance, coefficient of friction, and lubrication properties) in order to truly realize practical EM implementation [5].

1.2 High Power Electric Switches

Switches are a well known component in electrical systems. The purpose of the switch is to either complete a circuit or redirect current flow. The simplest electromechanical switch is the single-pole configuration comprised of a stationary and a movable contact. The switch is operated to complete or break an electrical circuit by having the contacts touching or separated. High power switches are required to efficiently sustain high current densities reliably for extended duty cycles. In the disconnecting and connecting events, mechanical properties are particularly critical to mitigate the deleterious effects of arcing, wear mechanisms, and elevated temperatures [6], [7].

High power systems magnify the aforementioned methods of contact degradation. Examples of these applications include switchgears and power switching. High energy arcing produces elevated temperatures and very concentrated surface damage [8]. Several methods utilized to minimize arcing place more stringent demands on the mechanical properties of the contacts. Several material properties must be considered in the design of cost-effective and reliable operation of these extreme electrical contacts, particularly for an extended number of switch cycles [9], [10]. Requirements for

3

increased efficiency advancements and power handling capacities have created a demand for more capable contact material solutions [11]. The optimization of tribological properties must be coupled with considerations of mechanical and conductivity material properties.

1.3 Focus of this Research

A systematic materials selection procedure was developed to identify and compare candidate materials that would be more durable for these types of applications. Moreover, several possible candidate monolithic materials as well as hybrid materials that could potentially be even better, filling the "white spaces" on the material property charts, were identified. A couple of these potential candidate materials were obtained and evaluated. These included copper-tungsten W-Cu, "self-lubricating" graphite-impregnated Cu, and Gr-W-Cu composites with different volume fractions of the constituents. The structure-property relations were determined through mechanical and electrical resistivity testing. A unique test protocol for exposing mechanical test specimens to extreme current densities up to 1.2 GA/m^2 was developed and used to evaluate these candidate materials.

The design of materials including optimizing the microstructure attributes for these applications can potentially be accelerated by using micromechanics modeling and other materials design tools coupled with systematic mechanical and tribological experiments. In this study, physics- and micromechanics-based models were used to correlate properties to the volume fraction of the tungsten. These properties included elastic modulus, hardness, tensile strength, and electrical resistivity.

4

Chapter 2: Materials Selection Using the Ashby Method

2.1 Introduction

Conventional methods for material selection have relied on experience based selection approaches. This results in limited material solution space exploration. There are significantly more robust and comprehensive material selection processes to ensure complete consideration and optimal selection of material system solutions. This chapter presents the procedure of the Ashby material selection method [12]. As a case study, the selection of the rail material in an electromagnetic launcher (EML) is considered. Material selections will be considered for the Archard's and melt erosion wear mechanisms at rail surfaces. This effort is spurred by recent post-mortem observations of rail surfaces that suggest two distinctly different wear mechanisms may be occurring at different locations along the rail surfaces. This selection process will examine elementary materials as well as complex material systems (e.g. composites, exotic materials, and alternate configurations).

2.1.1 Derivation of Performance and Material Indices

The Ashby method is founded on systematically relating material performance requirements to quantifiable material properties. The first step involves developing a translation table, shown in Figure 2. The translation table identifies the function, constraints, objective, and free variables of the material selection. The function entry specifies the component and its desired purpose. For this exercise, we desire a highly durable, wear-resistant material that can conduct extreme currents. The constraints list all

the requirements that must be met in addition to the primary functions. In the material

selection process, the constraints are used to screen out those solutions that cannot work.

For example, fracture toughness is pertinent to the service environment. Tremendous

shock is experienced as the armature is accelerated the length of the bore. We need to

screen out those solutions that have unacceptably low fracture toughness, or in other

words are "too brittle." A conventionally accepted minimum fracture toughness

threshold for engineering practices is 15 MPa $m^{1/2}$. High service temperature is

necessary to withstand the localized zones of Coulomb and Joule heating. Recent

numerical modeling analyses [4] have yielded results that indicate near surface regions of

elevated temperatures. In efforts to ensure reliable intimate armature-rail interface

contact, extreme preloads are initiated as the armature is loaded into the breech. The

constraint of high elastic yield limit and sufficient stiffness needs to be met. A robust

material that will withstand these loadings without plastic deformation is necessary for

consideration.

Function	Wear Resistant-Conductive EML Rail
Constraints	High melting point High strength High thermal conductivity Sufficient Toughness Corrosion resistance in marine environment No to low toxicity
Objective	Maximize wear resistance Minimize power loss due to Joule heating
Free Variable	Choice of Material

Figure 2: Translation Table for Wear Mechanisms

The objectives identified in the translation table are the performance metrics used to rank potential solutions that have passed the screening using the constraints. For each objective, a performance equation is derived that either needs to be minimized or maximized. Examples of objectives include minimize cost, minimize mass, minimize deflection, minimize electrical resistivity, wear volume removal, and so on. The material that best meets the objective is selected as the optimal solution. In the case of multiple objectives, which are often conflicting, a set of pareto-optimal solutions is identified, usually graphically. The free variables refer to design inputs that have not been explicitly specified (e.g. material choice, geometrical parameters such as the width of the rail, etc.). Most materials selection problems have multiple objectives. For rail material, the primary objectives are to select a material with maximum wear resistance and minimum electrical dissipation due to Joule heating. A performance equation is derived for each objective.

Due to the observations of two distinct wear mechanisms, a performance equation will be derived to relate each type of wear mechanism with the pertinent material property. First, a performance equation for maximizing wear resistance is derived based upon wear mechanisms dominated by the hardness of the material. Wear is characterized by Archard's wear equation,

$$W = \frac{KN}{H} \tag{1}$$

where W is the wear volume per unit sliding length, N is the normal load, and H is hardness of the bodies assessing the wear.

The second performance equation is derived assuming wear mechanisms are related to thermally assisted melt erosion mechanisms; particularly, current melt erosion.

An example of this type of wear is characterized by localized melting, viscous flow, and recasting near the rail surface. The melt erosion of a conducting slab under an applied current density has been related to several loading parameters and material properties [13]-[18]. Loading parameters include magnetic field magnitude, current density, and geometrical configuration factors. Material properties relevant in the approximation of melt erosion include magnetic diffusivity, latent heat, specific heat, density, melting temperature, and electrical resistivity. The onset of melting is assumed to initiate when the energy required to achieve melting (i.e. the left term of energy balance equation) is reached due to the thermal energy input of Joule heating (i.e. the right term of energy balance equation). An energy balance [19] is used to relate the material properties to the loading parameters by

$$E_m = \rho_m c_v (T_m - T_o) + L_m = \rho \int_0^t \left(\frac{-\partial H_z(x,t)}{\partial x} \right)^2 dt \tag{2}$$

where E_m is the melting energy per unit volume, ρ_m is the mass density of the semi-infinite conducting slab material, c_v is the specific heat, L_m is the latent heat of melting, ρ is the electrical resistivity, T_m and T_o are the melting and initial temperatures, respectively. The integrand in this equation is the current density due to the magnetic field. H_z is the vertical component of the applied magnetic field, H, in the conducting slab, as illustrated in Figure 3.
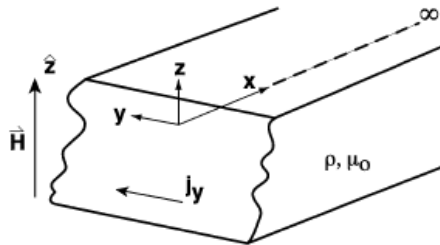
Figure 3: A vertically oriented magnetic field, H, is applied to the surface of a semi-infinite conducting half-space

The exact relationship between the melt and wear rate is highly dependent on the details of the armature-rail interface and loading parameters. On this premise, a second performance equation to maximize wear resistance is assumed to be inversely proportional to the energy required to induce melting,

$$W \propto \frac{1}{E_m} \tag{3}$$

For all other material properties and loading parameters being held consistent, it is concluded from equation 2 that the onset of melting is delayed for a material with a higher melting temperature. The maximum service temperature, as defined in CES EduPack, is the maximum temperature a material can be exposed to for an extended period of time before oxidation, excessive creep, loss of strength, or chemical changes occur. The CES EduPack software is presented in detail in the next section. This material property is utilized instead of the melting temperature as a means to ensure robust selection of durable candidate material solutions. The maximum service temperature is selected because it ranges roughly by a factor of five for candidate materials; however the density and specific heat capacity only range by factors of two and three, respectively.

In both wear performance expressions, the objective is to minimize the wear equation. Hence, these equations represent the performance equations for minimizing wear rate. To determine the material index component for this objective, the material properties component of these equations are identified,

$$\text{Wear Mechanism 1 } M_{1,a} = \frac{1}{H} \tag{4}$$

$$\text{Wear Mechanism 2} \quad M_{1,b} \propto \frac{1}{T_{max}} \tag{5}$$

where it is desired that M_1 be minimized.

To minimize power loss due to Joule heating, power dissipation in the rail is the basis for deriving the performance equation. In resistive circuits, dissipated power is given by

$$P = I^2 R \tag{6}$$

where I and R are current and resistance, respectively. The resistance of the rail component is given by

$$R = \frac{\rho L}{A} \tag{7}$$

where ρ, L, and A are electrical resistivity of the rail material, length of the rail between which the resistance is measured, and the uniform cross-section area of the rail, respectively. Combining Eq. (3) and (4), the second performance equation is given by

$$P_2 = \frac{I^2 L \rho}{A} \tag{8}$$

The material index is the part of the performance equation that contains material properties,

$$M_2 = \rho \tag{9}$$

which is to be minimized. Hence, to reduce the power loss, the electrical resistivity of the material needs to be minimized.

2.1.2 Displaying the Results

This exercise involves two conflicting objectives. Therefore, the first step is to find the set of possible candidate materials along the Pareto frontier. To identify the

10

Pareto frontier, a plot of M_1 versus M_2 is generated using the CES EduPack software [20], developed by Granta Design Limited (www.grantadesign.com). This is a unique software package designed to aid the engineer in material selection as well as help identify possible hybrid material solutions and processing possibilities. The software uses several databases, from elementary databases such as the MMPDS aerospace (formerly MIL-HDBK-5), MIL-HDBK-17 (composites), and CAMPUS and IDES databases for plastic materials as well as others established by Granta Design. The two databases used in this study are EduPack Level 2 and Level 3. EduPack Level 2 database consists of 98 elementary materials. A more extensive selection process can be obtained using the EduPack Level 3 database in CES EduPack. This database consists of 2920 materials, roughly representing over 98% of the readily available materials used in engineering systems today. This database includes all classes of materials including metals, ceramics, polymers, elastomers, natural materials and some hybrid solutions such as carbon fiber reinforced polymer (CFRP) composites.

The material databases are unique in that all properties are provided including general properties (i.e., density and cost), mechanical properties, electrical properties, thermal properties, optical properties, durability properties, production cost, and ecological considerations all in a structured quantifiable format. In addition, a processing database gives critical information concerning shaping, joining, and surface treatments that can be used in the material selection process.

The materials are typically represented by ellipses on the Ashby plots. The coloring of the ellipse identifies the classification of the material family (e.g. metal and alloys, composites, polymers, technical ceramics, and etc.). The elliptical shape

11

represents the potential variation in material properties. Grey-shaded material envelopes would represent materials that failed the screening process, while the color-filled envelopes represent materials that passed.

The Level 2 database is utilized to evaluate any potential solutions. This initial inspection is completed to capture a broad survey of potential candidates. No screening constraints are imposed at this point to ensure full solution space exploration. The resulting plots for hardness versus electrical resistivity and maximum service temperature versus electrical resistivity are presented in Figure 4 and Figure 5, respectively. The ideal materials are located in the lower left part of these plots along the Pareto frontier shown. The set of Pareto-optimal solutions are those most interesting materials that lie near the Pareto frontier curve shown in Figure 6 and Figure 7, which show the lower left part of Figure 4 and Figure 5, respectively. The two primary objectives are plotted such that the ideal material is located in the lower left region of the plot. A subset of potential material solutions that are near the region defined by minimization of M_1 and M_2 is presented in Figure 6 and Figure 7. The set of Pareto frontier solutions for wear controlled by hardness based on the EduPack Level 2 database include tungsten carbides, tungsten alloys, nickel, high carbon steel, low alloy steel, aluminum alloys, copper, zinc, and Al-SiC composites. The set of Pareto frontier candidates for wear associated with melt erosion include aluminum alloys, nickel, steel alloy, tungsten carbides, and tungsten alloys, as shown in Figure 7. Hardened copper (C110 H04) is commonly used for the rail material today. As seen in these figures, this hardened copper is a non-dominated solution, i.e., one along the Pareto frontier, for both wear considerations, suggesting it is a viable solution. However, hardened copper gives much more value to high conductivity

12

instead of wear resistance, the latter being more critical for durability. Tungsten alloys standout as highly promising candidates due to their reasonably good conductivity combined with refractory properties that provide good wear resistance particularly for wear associated with melt erosion. Tungsten carbide exhibits good wear performance when Archard's wear model captures the wear mechanism.
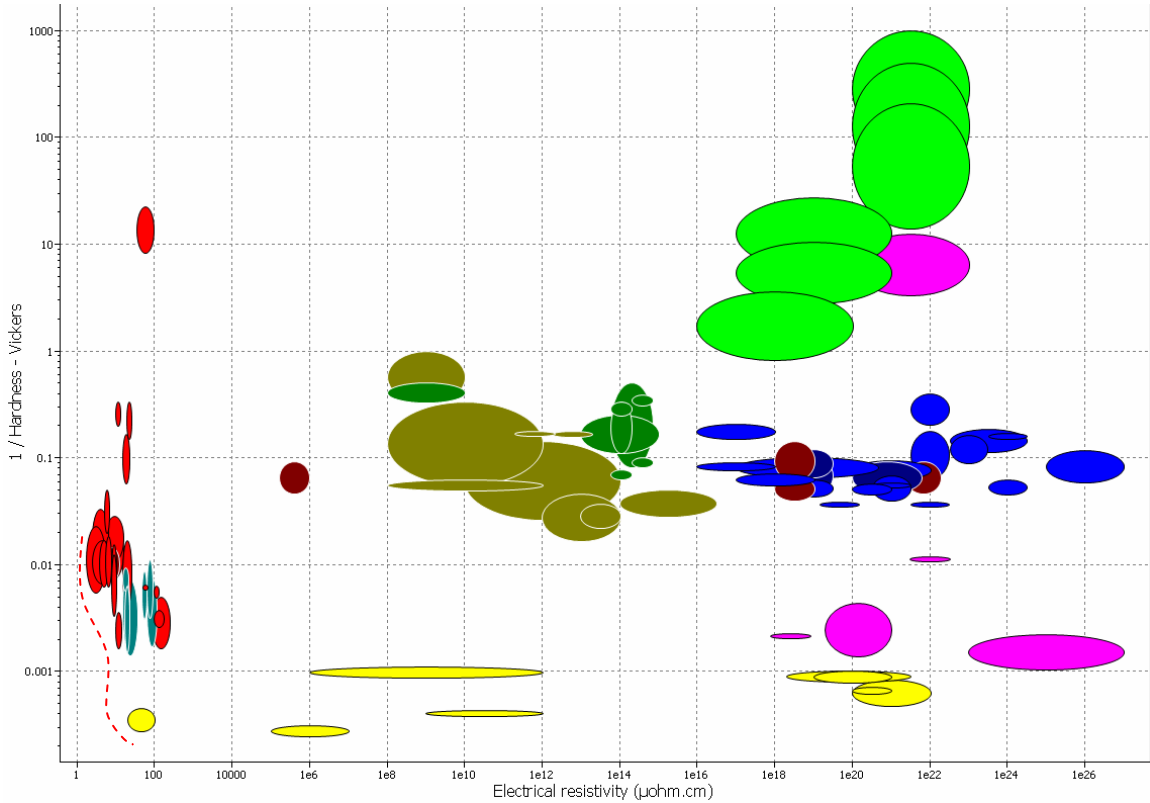
Figure 4: Display of objectives M_1 (1/H) vs. M_2 showing all CES EduPack Level 2 materials [20].
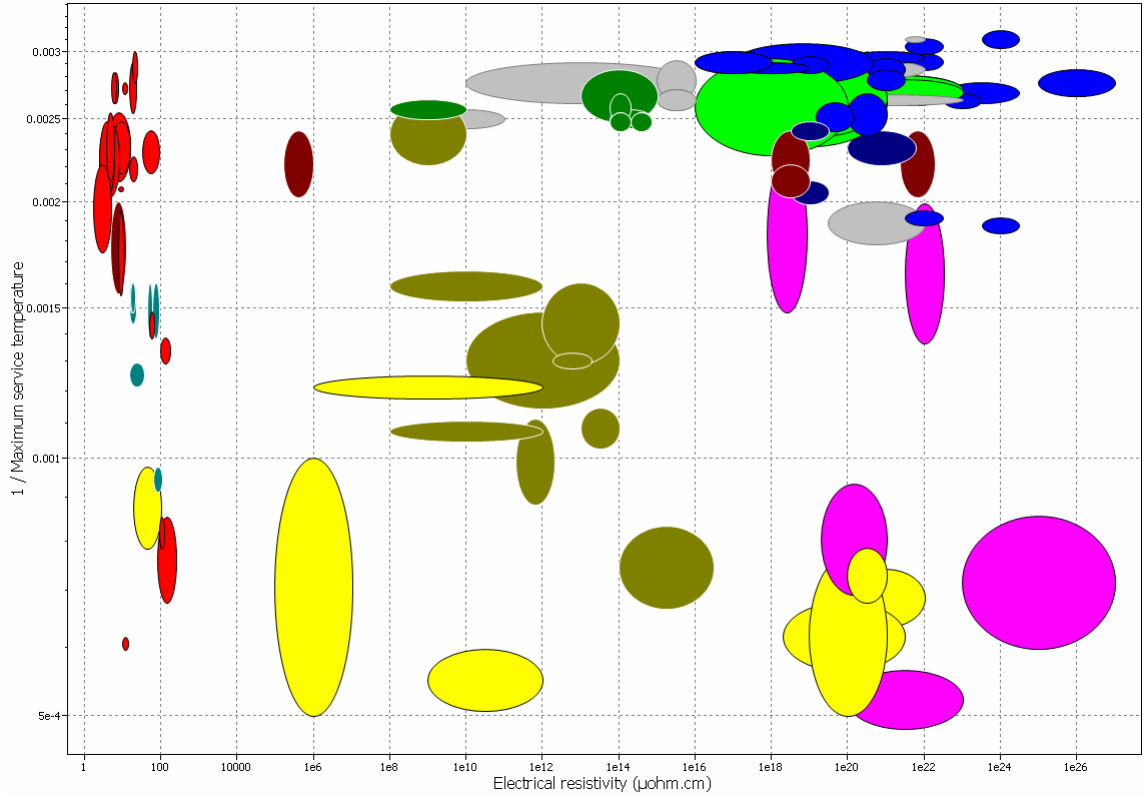
Figure 5: Display of objectives M$_1$ (1/T$_{max.}$) vs. M$_2$ showing all CES EduPack Level 2 materials [20].
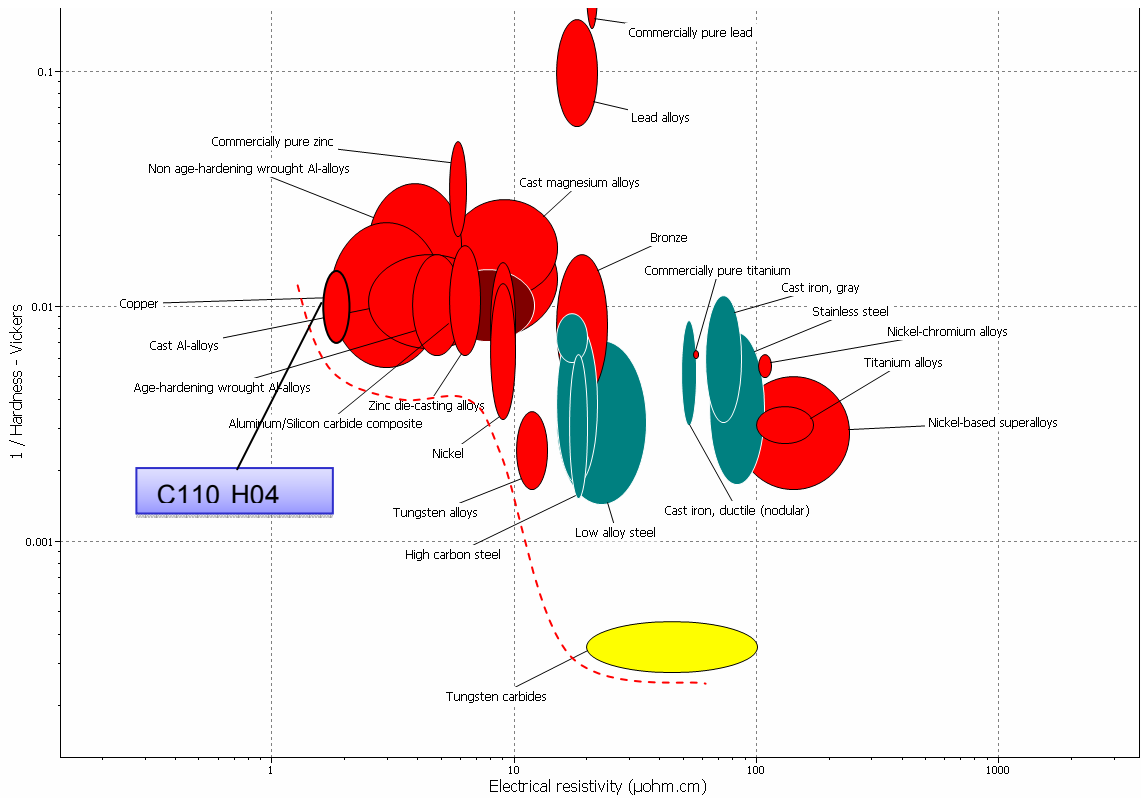
Figure 6: Display of objectives M$_1$ (1/H) vs. M$_2$ showing a subset of CES EduPack Level 2 materials close to the ideal material [20].
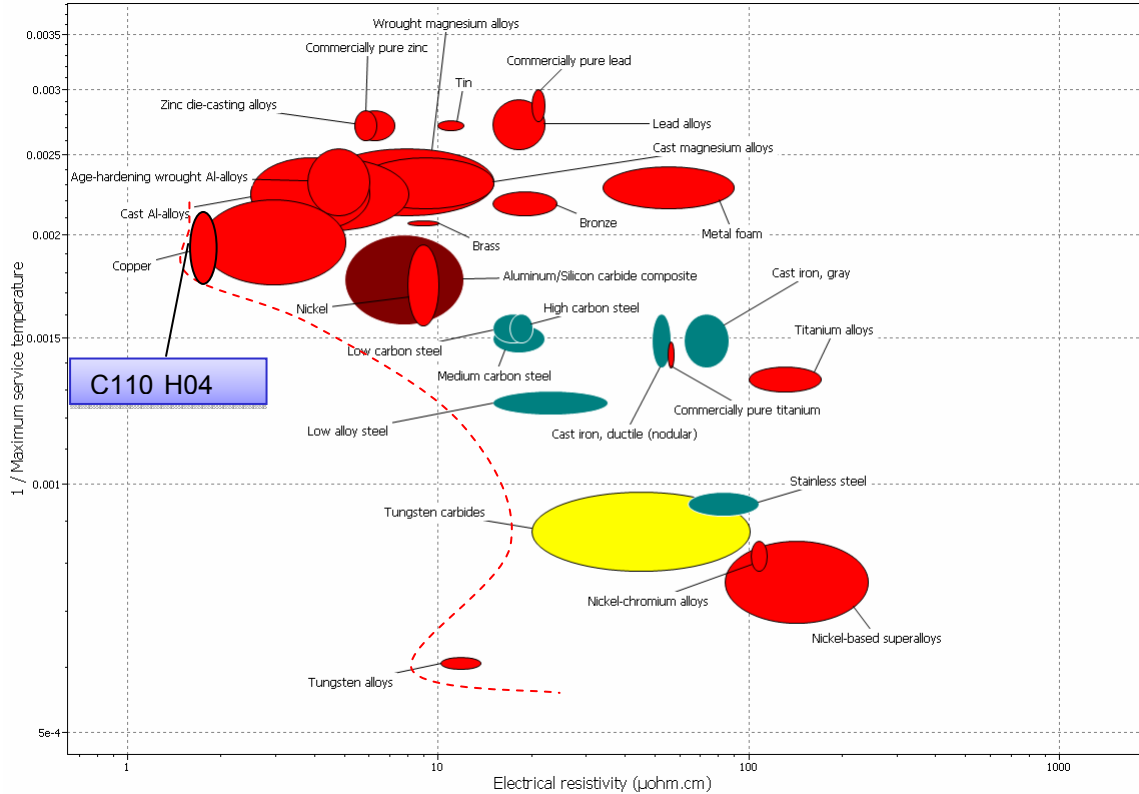
Figure 7: Display of objectives M_1 ($1/T_{max.}$) vs. M_2 showing a subset of CES EduPack Level 2 materials close to the ideal material [20].

A more exhaustive search of candidate materials was conducted using the Level 3 database. Since this database contains many more materials, screening constraints were first applied by setting the limits on properties based on the constraints identified in the translation table. In this step the main goal is to screen out those materials that will absolutely not be suitable so to have a smaller subset of potential solutions. A screenshot of this step from CES EduPack is shown in Figure 8. Here, 423 materials pass out of the complete set of 2920 materials when the preliminary constraints are applied. It is critical to not be too restrictive to ensure consideration of all feasible solutions. Marginal solutions should not be completely screened out at this stage since they may potentially be used in a hybrid solution discussed later. The objective is to screen out just those that

16

absolutely will not work. The constraints illustrated in Figure 7 represent minimal mechanical properties to basic structural requirements.
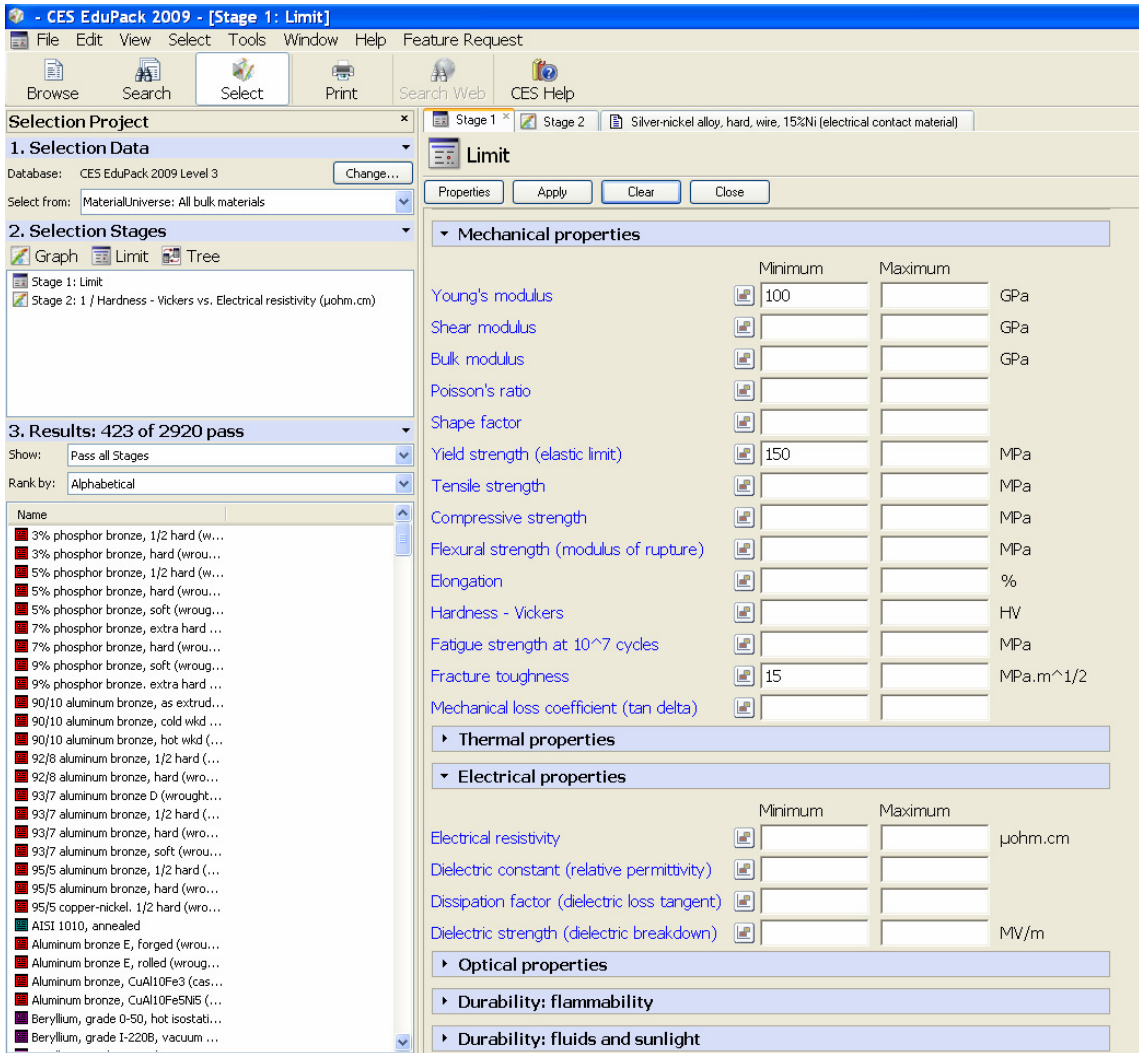
Figure 8: CES EduPack 2009 display of results after application of screening constraints [20].

The next step (Stage 2) is to graph the conflicting objectives of, M_1 versus M_2, shown for all materials in the database. The candidate materials, assuming Archard's wear mechanism operate, are shown in Figure 9. Due to the limited understanding of the melt erosion wear mechanism in these extreme electrical contacts, no quantitative constraints are applied for the EduPack Level 3 results. This approach will ensure that no potential solutions are erroneously screened out. The resulting material trade-off chart

based on the melt erosion wear mechanism is shown in Figure 10. The enlargement of

the lower left region of these charts are shown in Figure 11 and Figure 12, for Archard's

and melt erosion wear, respectively. The set of viable candidates are those materials that

lie near the Pareto frontier curve.
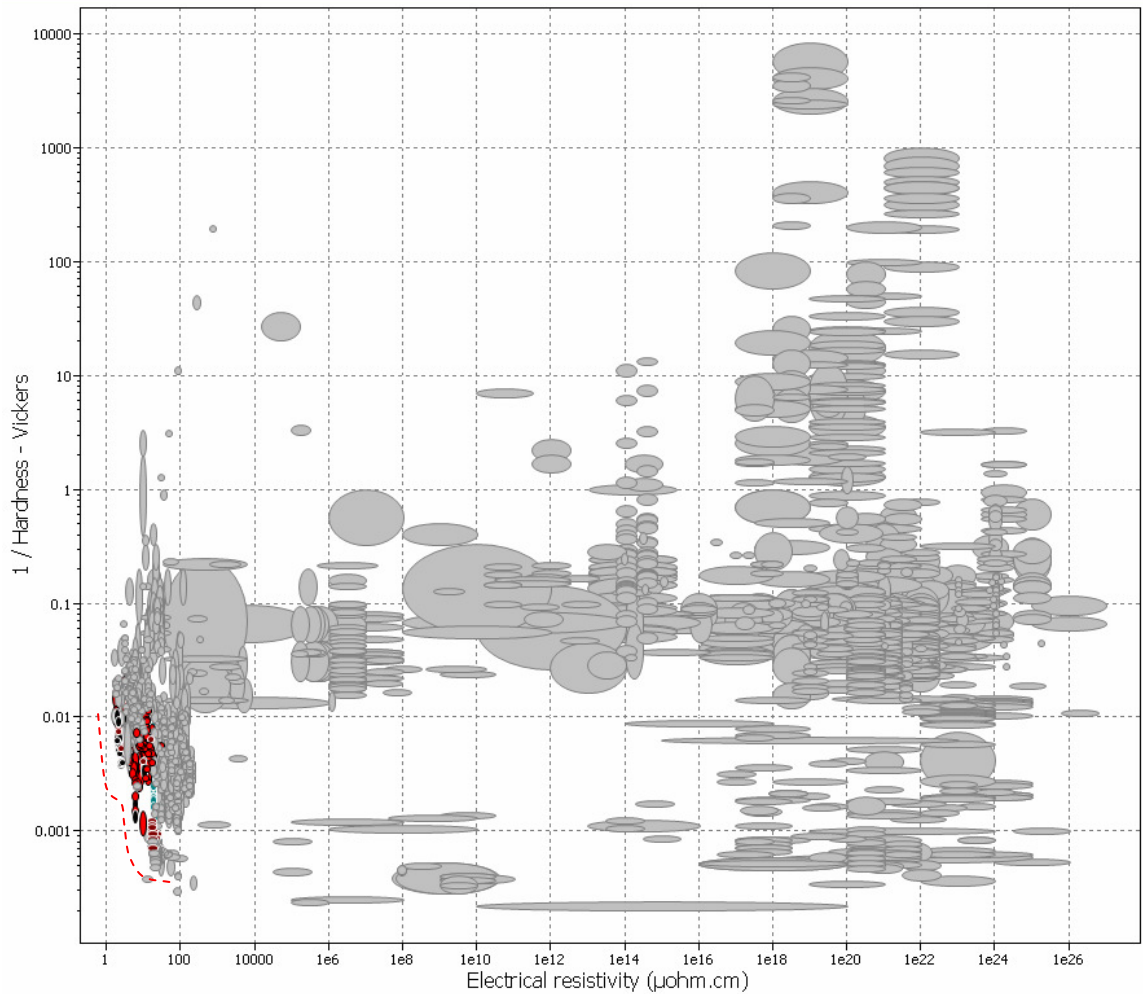
Figure 9: Display of objectives M_1 (1/H) vs. M_2 showing all CES EduPack Level 3 materials [20].
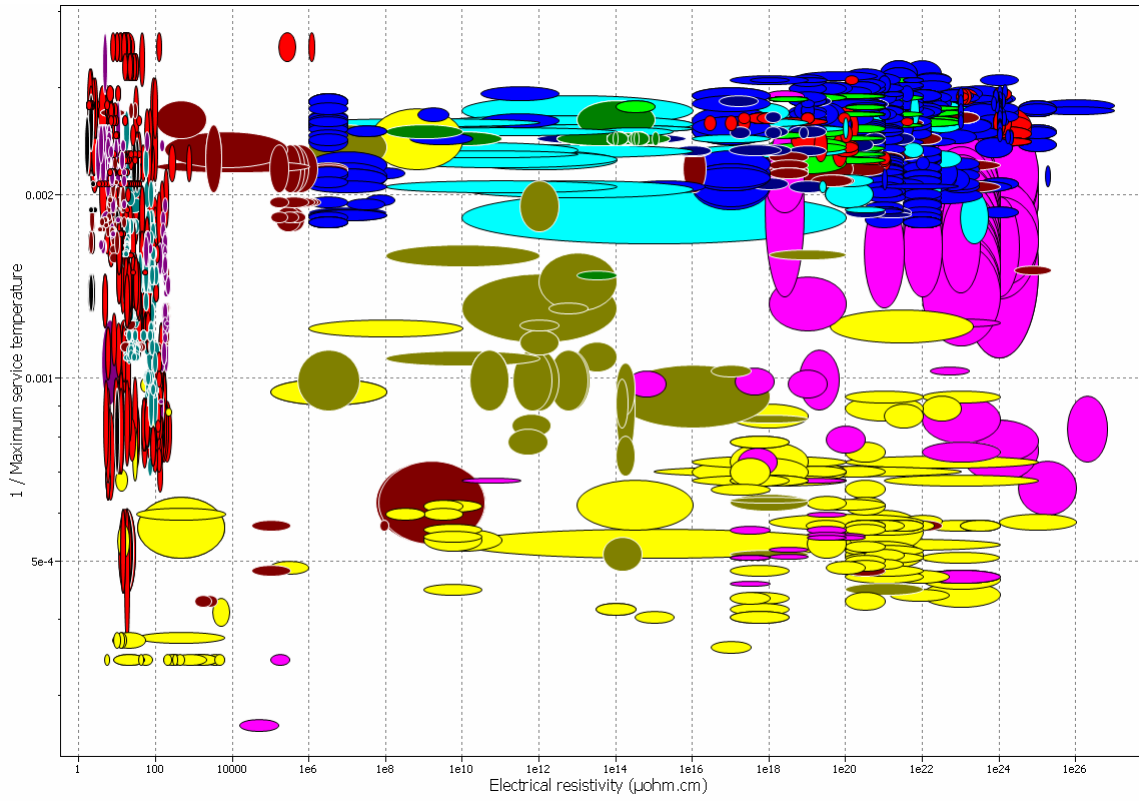
Figure 10: Display of objectives M_1 ($1/T_{max}$) vs. M_2 showing all CES EduPack Level 3 materials [20].
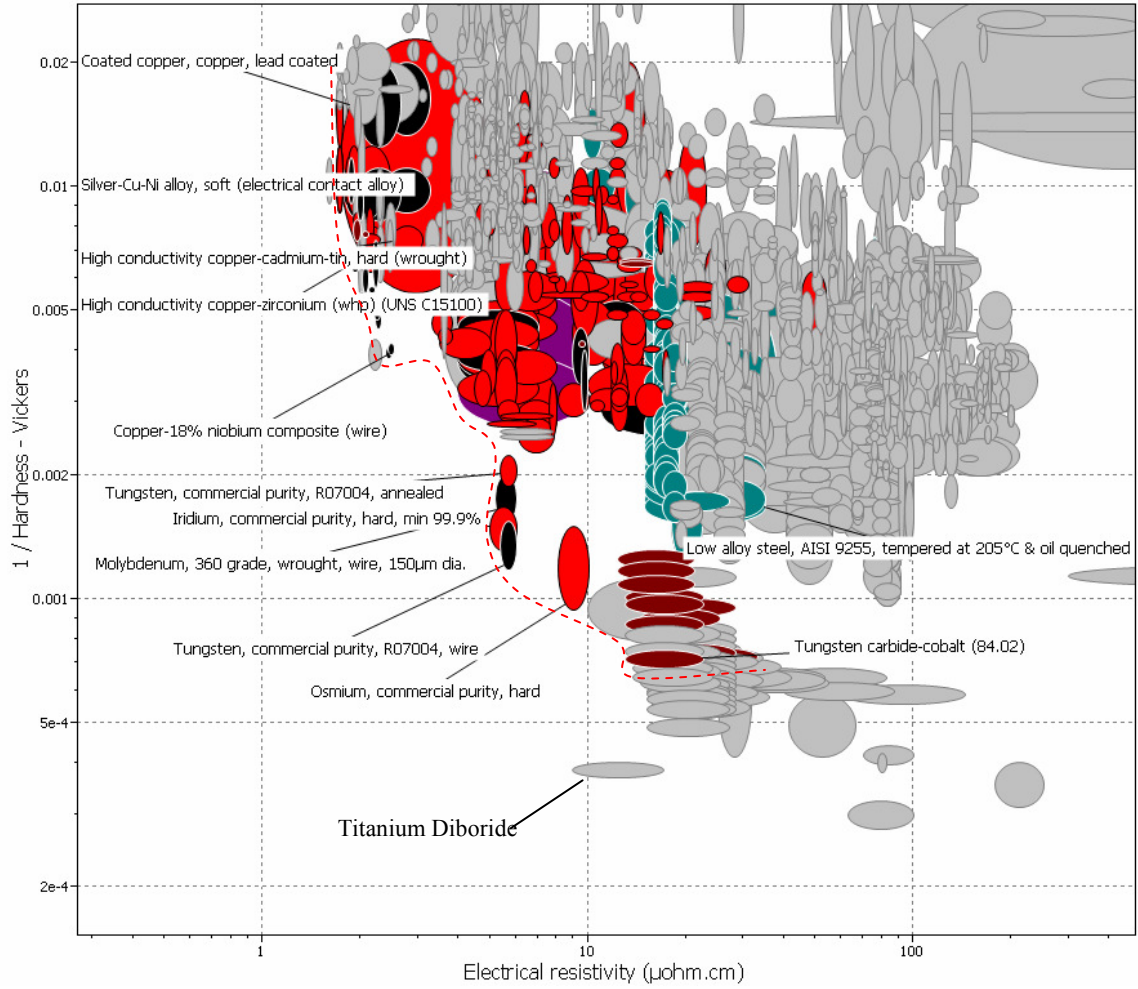
Figure 11: Display of objectives M$_1$ (1/H) vs. M$_2$ showing a subset of CES EduPack Level 3 materials close to the ideal material [20].
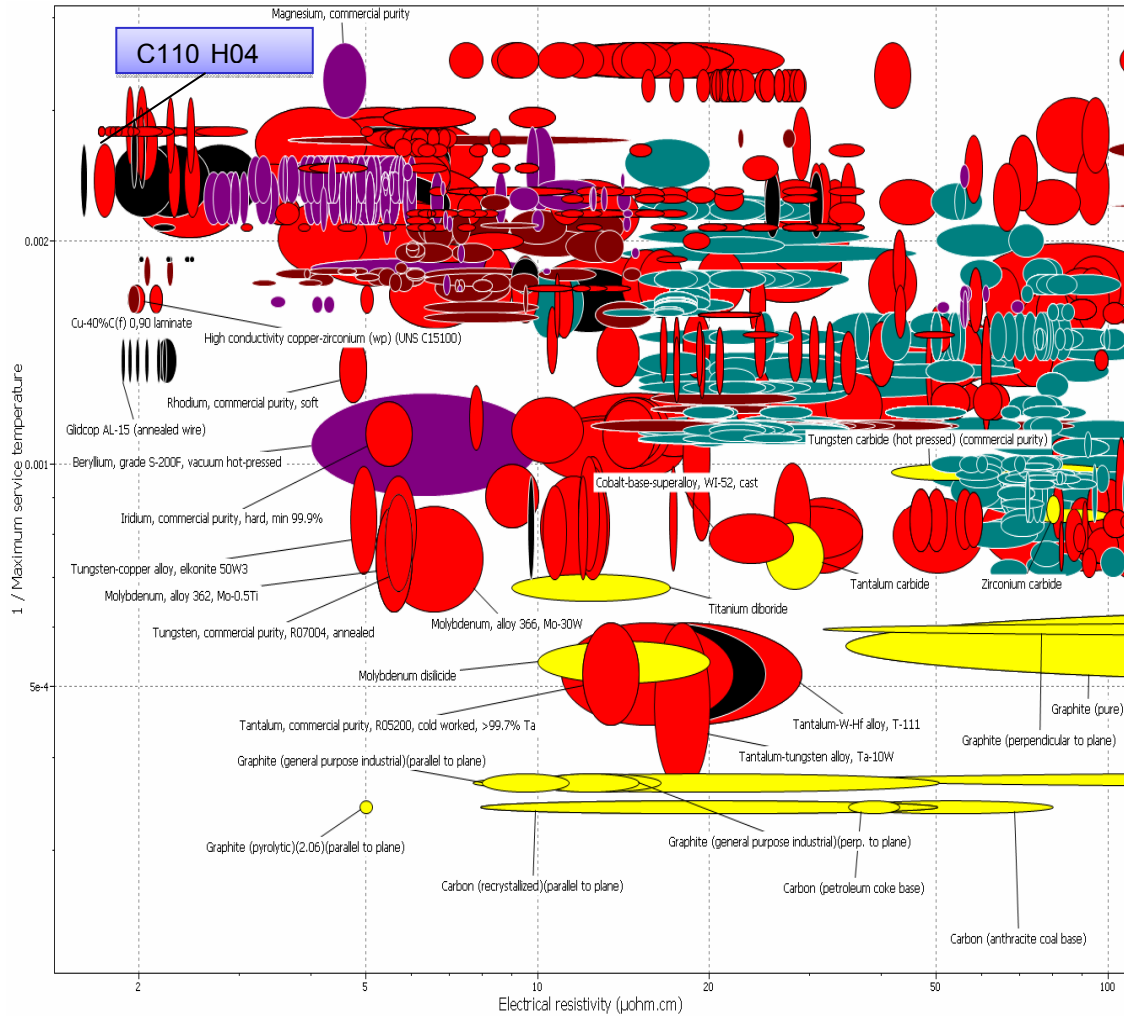
Figure 12: Display of objectives $M_1(1/T_{max})$ vs. M_2 showing a subset of CES EduPack Level 3 materials close to the ideal material [20].

As seen in these figures, the hardened copper, C110 H04, is still non-dominated solution for both wear considerations even with the expanded database, suggesting it is a viable solution. However, experience of using pure Cu in these extreme contact applications suggests that the durability in terms of the capability for repeated contacts is not satisfactory [1], [3]. So while C110 H04 meets one of the metrics well, it does not sufficiently meet the wear resistance metric. It suggests we need to consider trade-offs between resistivity and wear resistance. Additional conventional candidates along the

Pareto frontier shown in Figure 11 are tungsten, Molybdenum, Cu-Ag composites, copper alloys, copper composites, and tungsten carbides. Several promising materials, such as tungsten carbide and titanium diboride, with high hardness are screened out due to low fracture toughness. However, these materials may still be of interest as constituent materials in a hybrid configuration. For example, these materials could serves as particulate constituents within a composite comprised of a tough matrix material. The incorporation of hybrid materials and alternative configurations will be detailed later.

Figure 12 reveals that tungsten carbide is actually a dominated solution when including the additional materials in the Level 3 database. Tungsten, tantalum, molybdenum, their respective composites, and carbides are some of materials that are in the Pareto set that can sustain high maximum service temperature. In particular, tungsten-copper alloys (e.g., Elkonite), molybdenum alloys, and tantalum-tungsten alloys are materials with exceptional refractory properties. These materials are in the Pareto frontier set for both Archard's and melt erosion wear considerations. Graphite appears to be a promising solution; however, the orientation of the graphite is shown to have a significant effect on the electrical resistivity properties (e.g. order of magnitude difference when perpendicular to plane).
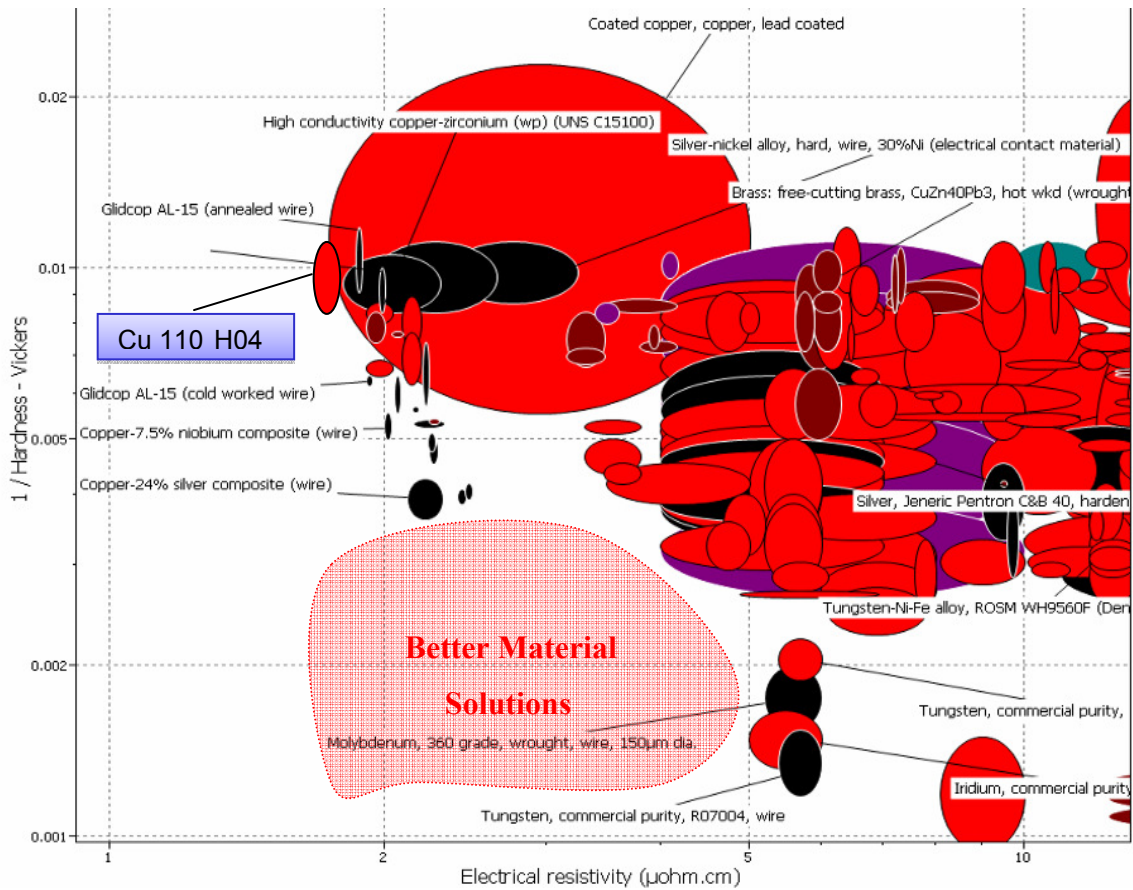
Figure 13: Zoomed in display of objectives M_1 (1/H) vs. M_2 showing a subset of CES EduPack Level 3 materials close to the ideal material [20].

An ideal material would be one located in the lower left "white space" region where none presently exist as shown in Figure 11 and Figure 12. These open regions can often be filled by hybrid material solutions. Hence, the focus of materials selection needs to be redirected to designing a hybrid material that may be much better than any of the materials currently in the Pareto set.

Identification of the desired material location for hardness driven wear considerations is highlighted in Figure 13. For example, these charts suggest that a viable hybrid solution could involve copper (Cu) and tungsten (W) as shown in Figure 14. The location of the properties of a particular hybrid solution depends on the volume fractions

23

of the constituents and the configuration. Presently, new hybrid solutions are not shown

explicitly on plots generated by CES EduPack, but possible solutions can easily be

surmised from these plots.
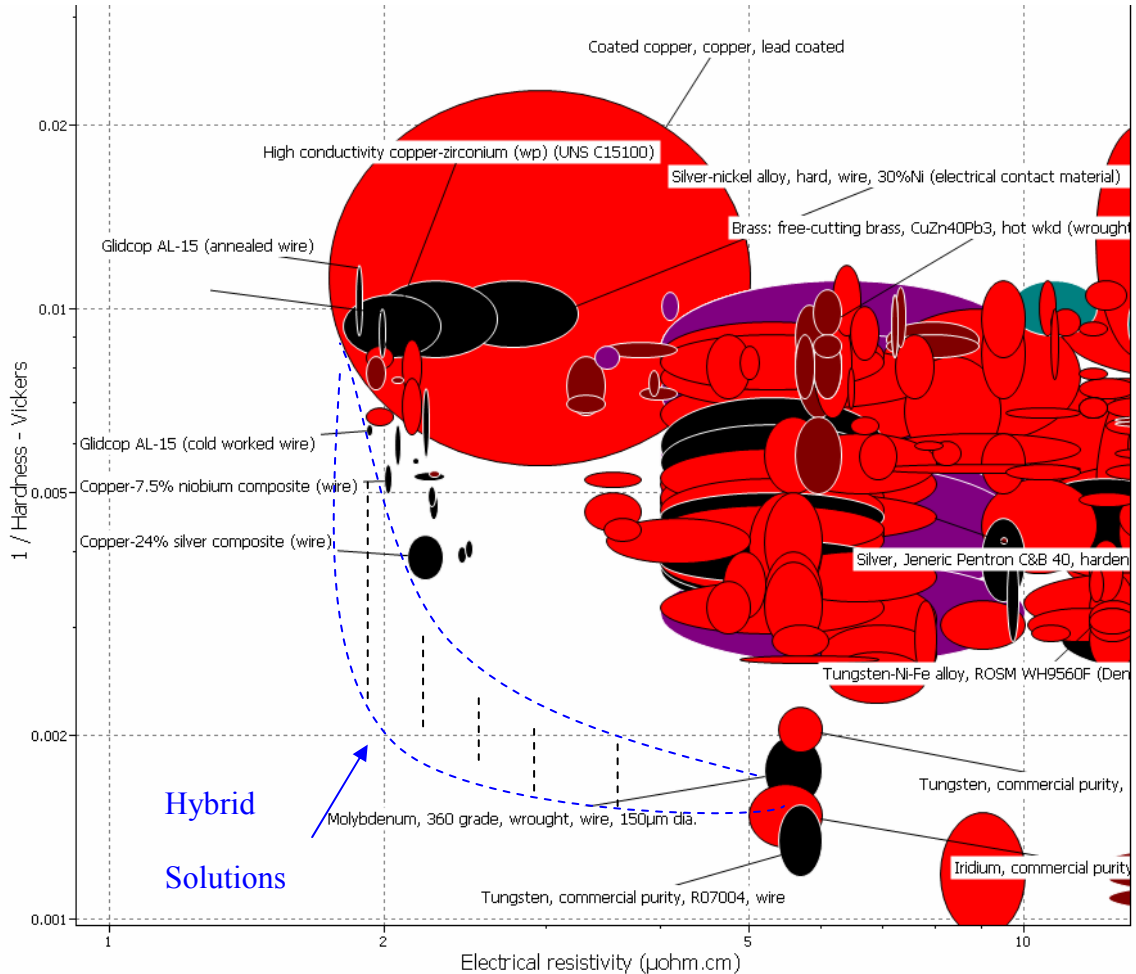
Figure 14: Potential hybrid solutions of Cu and W [20].

2.2 Configuration Considerations

For this solution, two hybrid configurations appear to be most viable: a

composite hybrid or an open-face sandwich hybrid. The composite hybrid could be a

particulate composite having dispersed particles of W throughout the ductile conductive

matrix Cu as shown in Figure 15. The properties of these hybrid materials can be tailored

through manipulation of microstructure attributes such as volume fraction, particle sizes,

and particle morphology. Potential increases in wear performance can be attained

through increasing concentration of the harder constituent for Archard's wear

mechanism. Higher concentrations of a refractory constituent potentially would reduce

the effects of melt erosion wear. Simultaneously, electrical conductivity could be

maintained through sufficient volume fraction of the conductive constituent.

Conductive carbide based constituents are presented in Figure 16. Tantalum

carbide, tungsten carbide-cobalt, tungsten carbide, molybdenum disilicide ($MoSi_2$), and

titanium diboride (TiB_2) are examples of candidates along the Pareto frontier that might

be used as hard particles in a particulate composite configuration. In addition,

molybdenum, graphite, Ta-W-Hf alloys, Ta-W alloys, and tantalum, $MoSi_2$, and TiB_2 are

identified in Figure 17 as candidates in the Pareto set that considers the trade-off between

electrical conductivity and resistance to the melt erosion wear mechanism. This

observation suggests these materials could be considered as constituents in a hybrid

solution aimed at improving the resistance to wear.
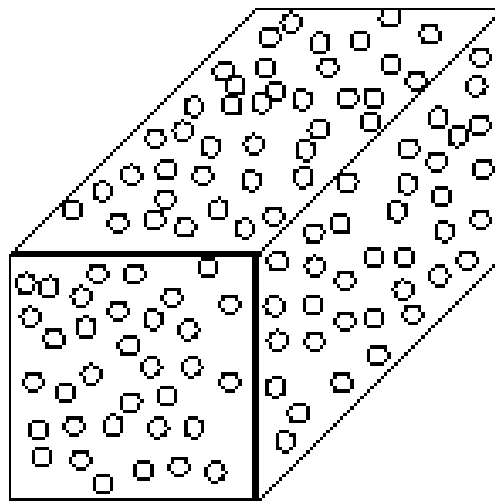
Figure 15: Particulate reinforced composite hybrid solution.

25
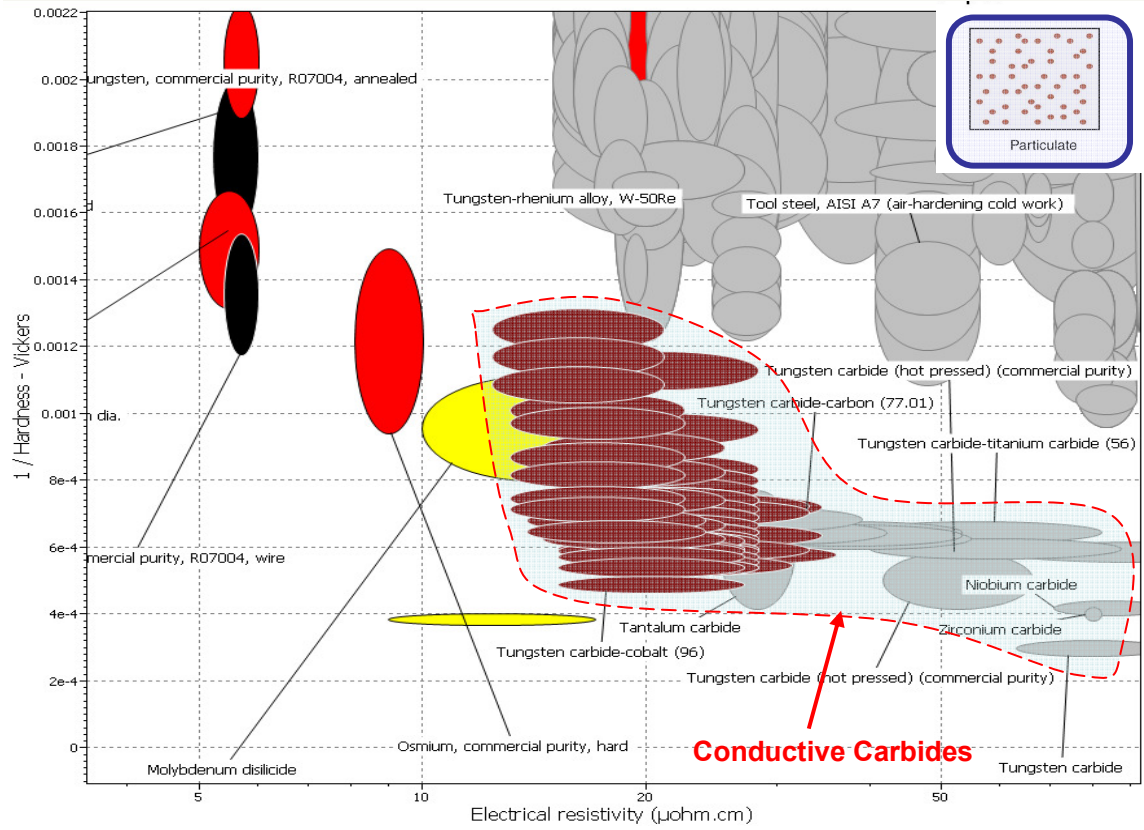
Figure 16: Display of relatively conductive carbides in CES EduPack Level 3 database [20]
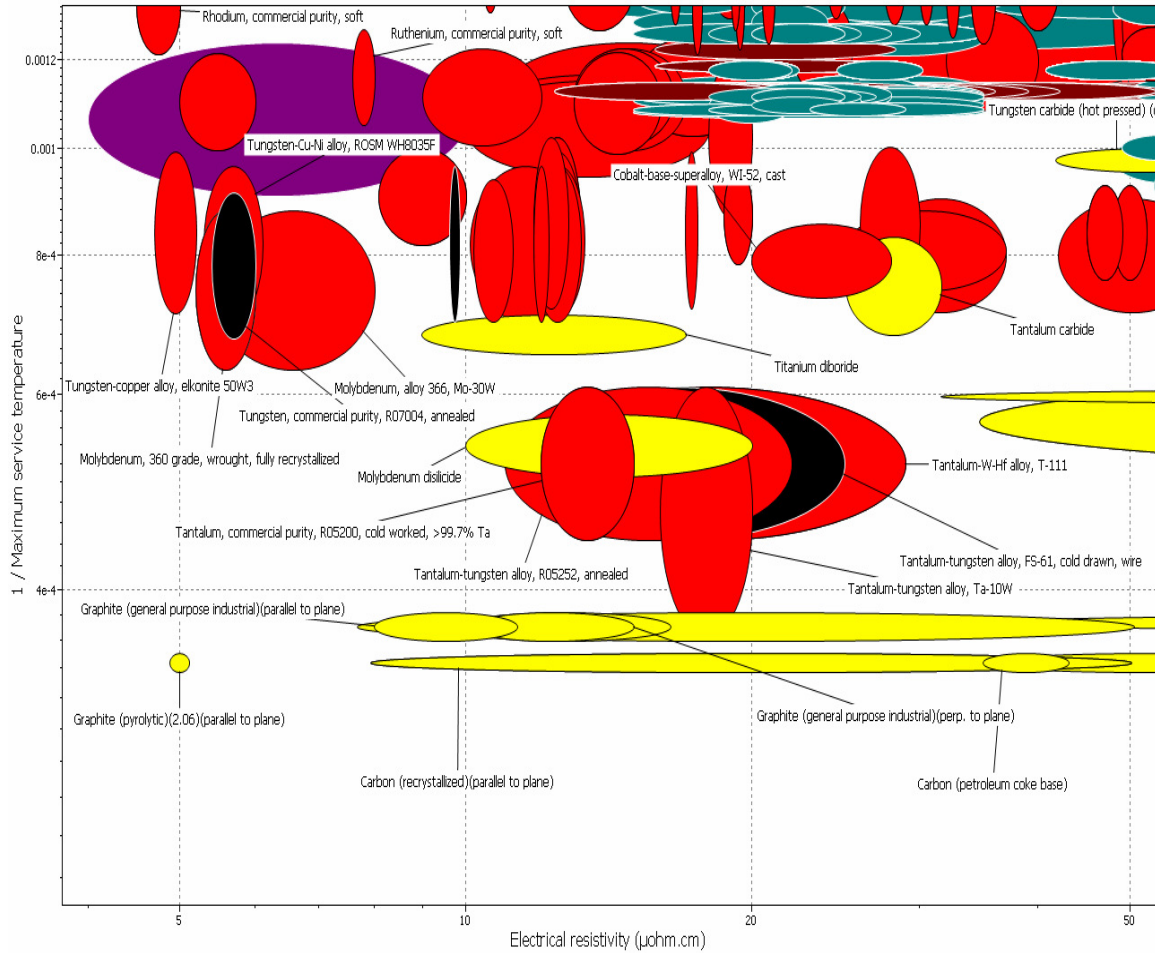
Figure 17: Display of relatively conductive refractory candidate constituents in CES EduPack Level 3 database [20]

Another possible hybrid solution is an "open-faced" sandwich construction as shown in Figure 18. An open-face sandwich structure is one that utilizes a coating or cladding. Here it is desirable for the coating or cladding to have high hardness and/or high service temperature properties to minimize the wear rate while maintaining relatively good conductive properties. Potential coating materials are shown in Figure 19 for Archard's wear mechanisms and in Figure 20 for maximum service temperature. Coating or cladding would need to be perfectly bonded to the conductive substrate so there is electrical conductivity and no interfacial failure. The coating also must not contain any porosity since this could increase resistivity and reduce structural integrity.

27

To facilitate interfacial adhesion strength, optimization for thermal diffusivity and conductivity, and substrate-coating matching of the coefficient of thermal expansion (CTE), the coating will need to be optimized. Attributes that can be varied through processing optimization include varying coating thickness, deposition method, composite coatings, tailored functional grading, and substrate surface engineering. Proper selection of the aforementioned parameters will potentially permit the tailoring of the coating/cladding physical, mechanical, and electrical properties.
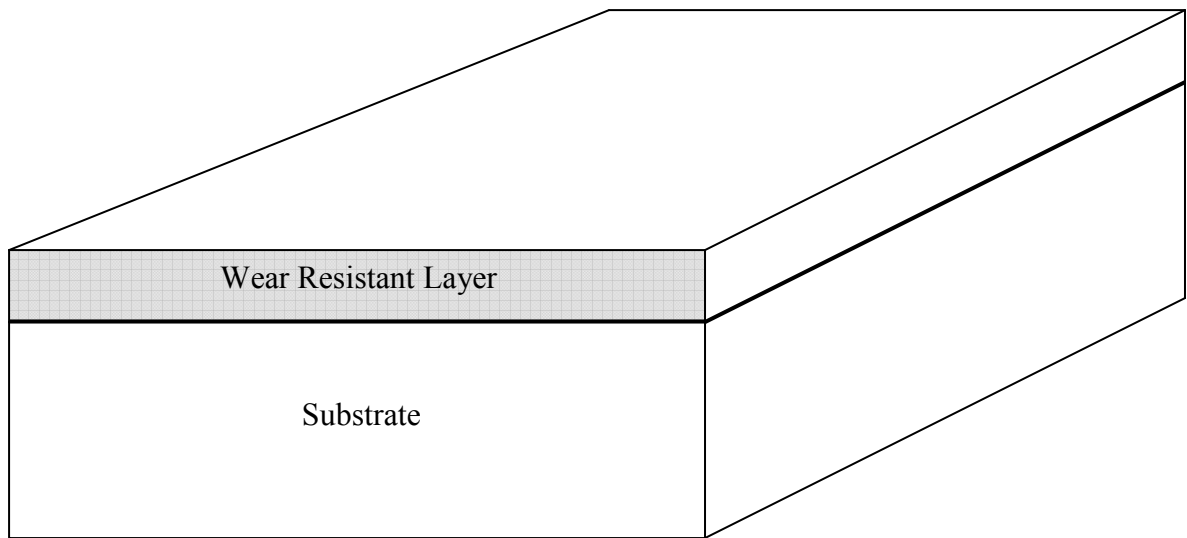
Figure 18: Open-faced sandwich hybrid solution.
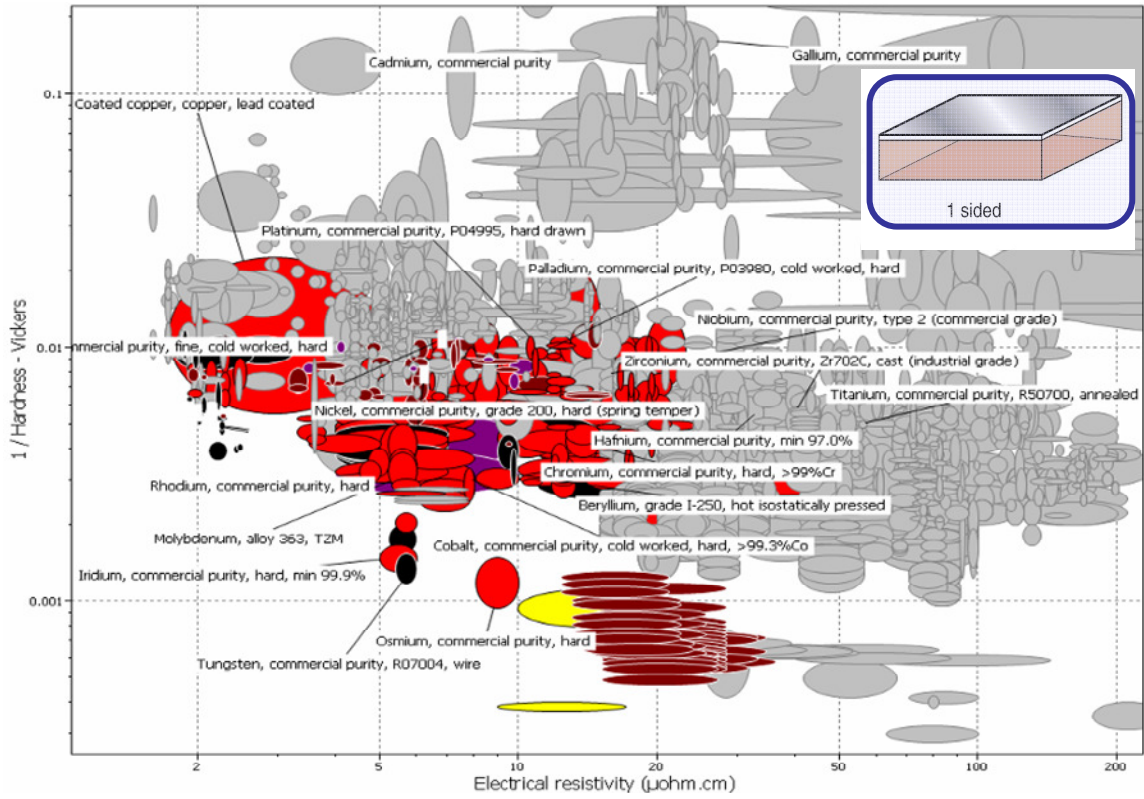
Figure 19: Preliminary candidate coating materials evaluated against Archard's wear mechanisms [20]
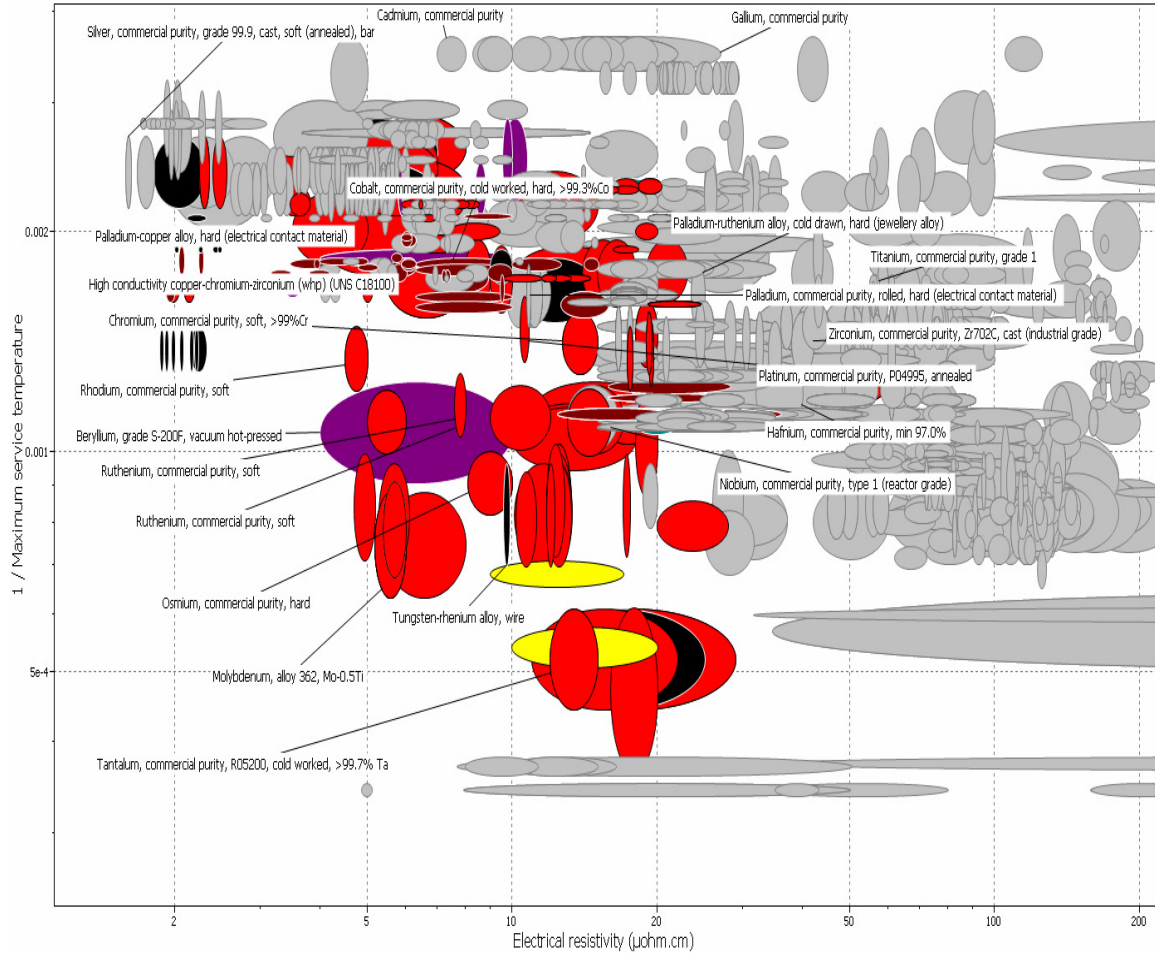
Figure 20: Preliminary candidate coating materials evaluated against melt erosion wear mechanisms [20]

2.3 Refractory Metals

If the melt erosion wear mechanism is prevalent, refractory metals, either monolithic or as a component of a hybrid solution, are potentially viable. Hence, it is worthwhile to investigate refractory metals in more detail. Besides tungsten, other possible refractory metals include tantalum, molybdenum, and iridium based on Figure 21 and Figure 22. Since a potential a potential hybrid solution may be a combination of copper and the refractory, a critical consideration in the evaluation of these materials is the nature of their interactions with copper at elevated temperatures. Secondary phase formations in the melt volume could potentially cause embrittlement as well as increases

30

in electrical conductivity. Phase diagrams are presented for each material to assess

potential reactions. Regarding tungsten, no intermetallics form between W-Cu as shown

in Figure 23.
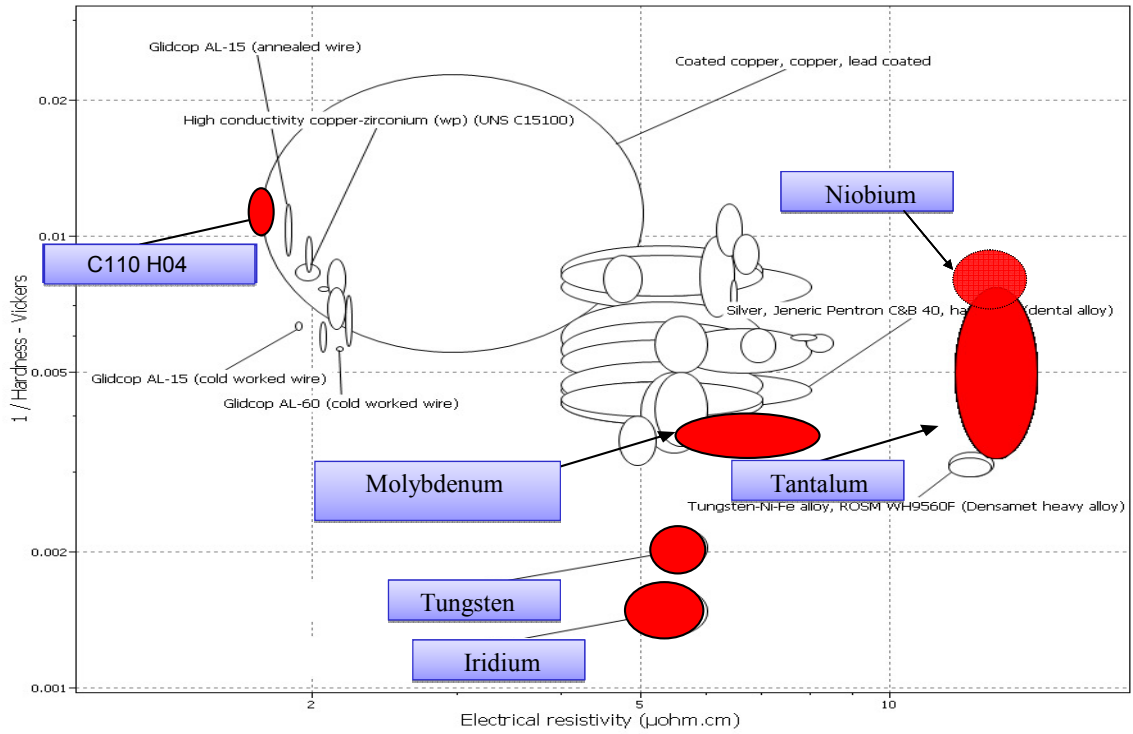
Figure 21: Ashby Chart Showing Refractory Metals for Archard's wear optimization [20]
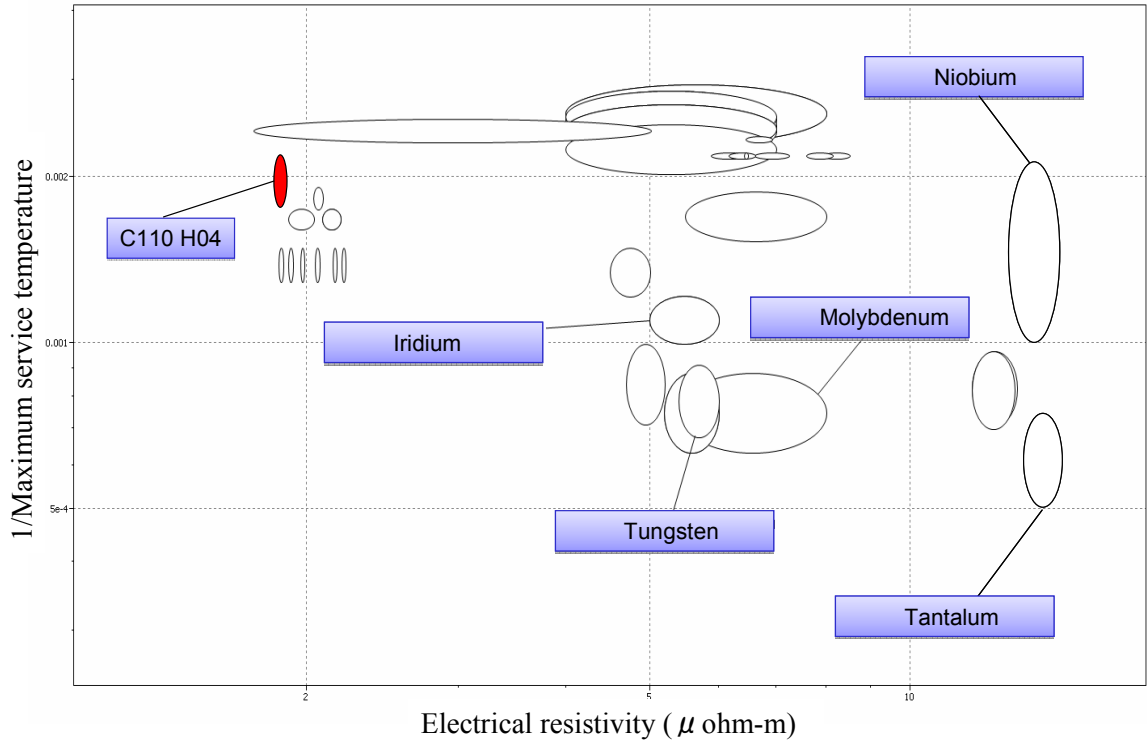
Figure 22: Ashby Chart Showing Refractory Metals for melt erosion wear optimization [20]
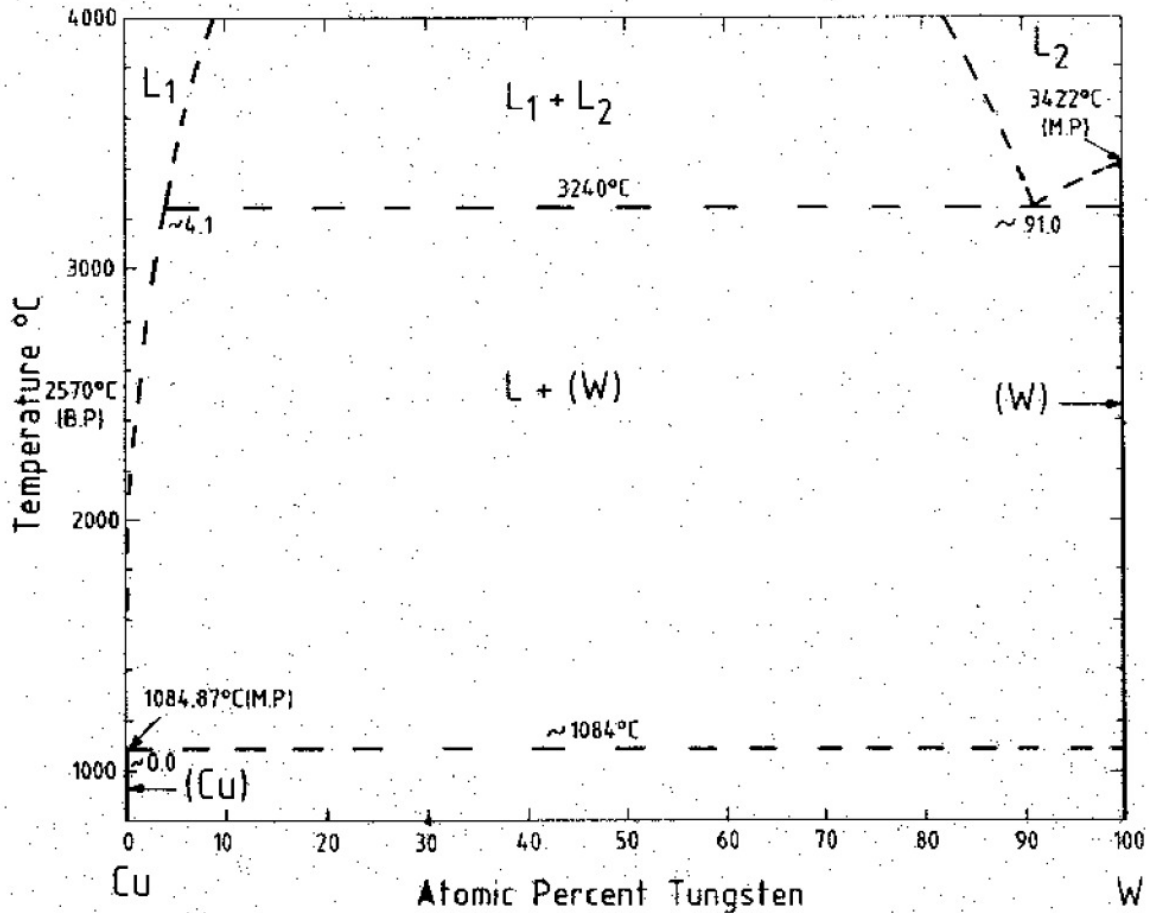
Figure 23: Copper-Tungsten Equilibrium Phase Diagram [21]

If all of these refractory metals are in the Pareto set, then the better candidate may be the lower cost solution, an additional screening constraint that can be applied. Relevant mechanical properties, density, cost, and relative cost comparison with tungsten are shown in Table 1. Maximum service temperature ranges are based on the values given in the CES EduPack database. Each alternative refractory metal is discussed further in the following sections.

Table 1: Material Cost and relevant material properties [20]

Material	Young's Modulus (GPa)	Fracture Toughness (MPa-m$^{1/2}$)	Yield Strength (MPa)	Max. Service Temp. (°C)	Density (kg/m^3)	Cost ($/kg)	Ratio of Cost Relative to Tungsten
C110 H4	131	50	280	90	8950	3.2	0.09
Tungsten	345	135	1515	825-1210	19300	36.5	1.0
Tantalum	182.5	120	702.5	1370-1980	16500	487.5	13
Molybdenum	325	30	517.5	867-1310	10100	38.0	1.04
Iridium	535	135	1025	550-730	22400	13150	360
Niobium	105	105	95	547-737	8600	228.5	6.3

2.3.1 Tantalum

Tantalum has higher electrical resistivity and lower hardness than tungsten. This material has slightly better high temperature properties than tungsten, but is nearly three times more resistive. The phase diagram shows that no intermetallic compound will form with copper. Tantalum is nearly 15% less dense than tungsten. The relative cost of tantalum is approximately thirteen times that of tungsten. Young's modulus and yield strength properties for tantalum are nearly 50% less than tungsten. This further reduces the practical consideration of tantalum as a beneficial composite material constituent of the hybrid material.
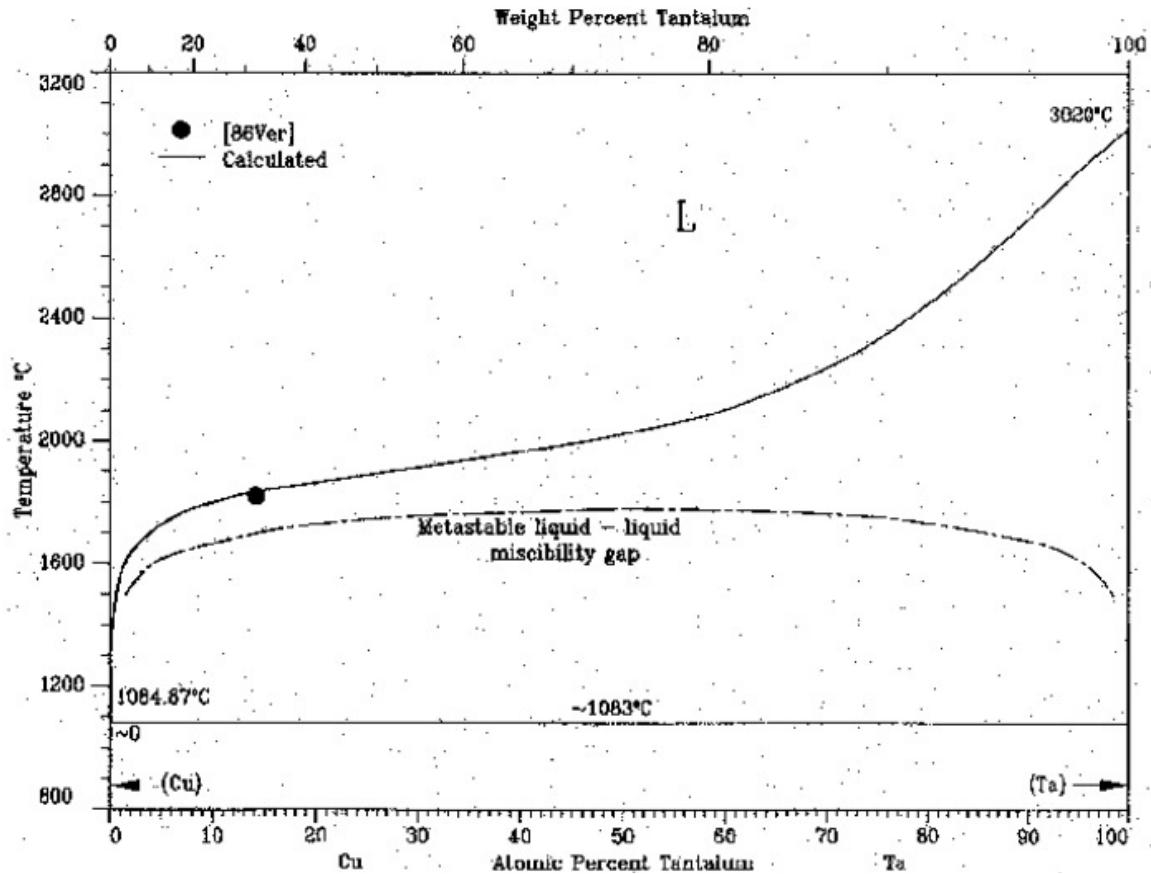
Figure 24: Copper-Tantalum Equilibrium Phase Diagram [22]

2.3.2 Molybdenum

Molybdenum appears to be a promising constituent in a hybrid material based on the analysis of hardness and electrical conductivity. Its electrical resistivity and maximum service temperature are approximately equivalent to tungsten; however, its hardness is nearly half that of tungsten. The phase diagram shows that no intermetallic compound will form with copper. The density of molybdenum is approximately half that of tungsten. The cost of molybdenum is comparable to that of tungsten; however, the fracture toughness and yield strength of molybdenum are approximately a third of tungsten.

35
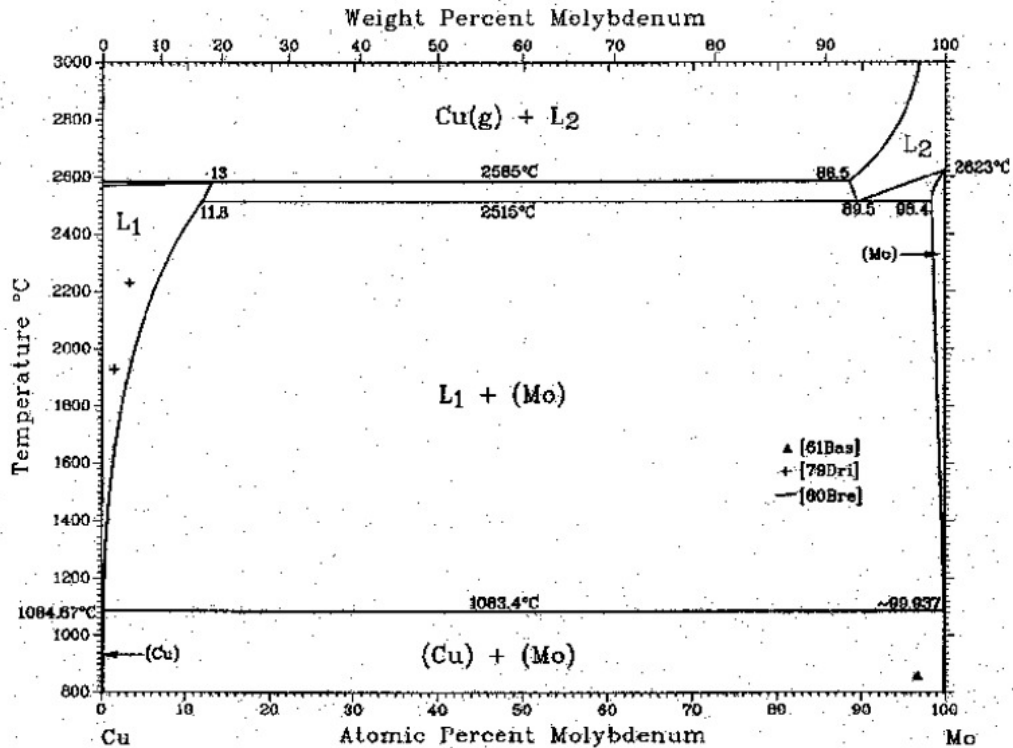
Figure 25: Copper-Molybdenum Equilibrium Phase Diagram [23]

2.3.3 Iridium

Iridium has higher hardness values and electrical resistivity comparable to tungsten and molybdenum. The maximum service temperature of this material is less than that of tungsten. The elastic modulus is greater than tungsten. Iridium and tungsten densities are comparable. However, the practical implementation of Iridium is significantly limited by the high toxicity of this material and its extremely high cost.

2.3.4 Niobium

Compared to the other refractory metals, niobium is a dominated solution on the trade-off plot shown in Figure 21. Its electrical resistivity is nearly three times larger than tungsten. Justification for niobium as a constituent material is further undermined by hardness values comparable to copper, so there is no gain in hardness. Comparison of

36

the maximum service temperatures in Figure 22 reveals that the maximum service temperature for niobium is 50-70% less than tungsten. The density of niobium is less than half that of tungsten. Consideration of toxicity and cost factors further exclude niobium as a copper composite material. Tungsten's yield strength is more than fifteen times greater than that of niobium. The phase diagram shows that no intermetallic compound will form with copper.
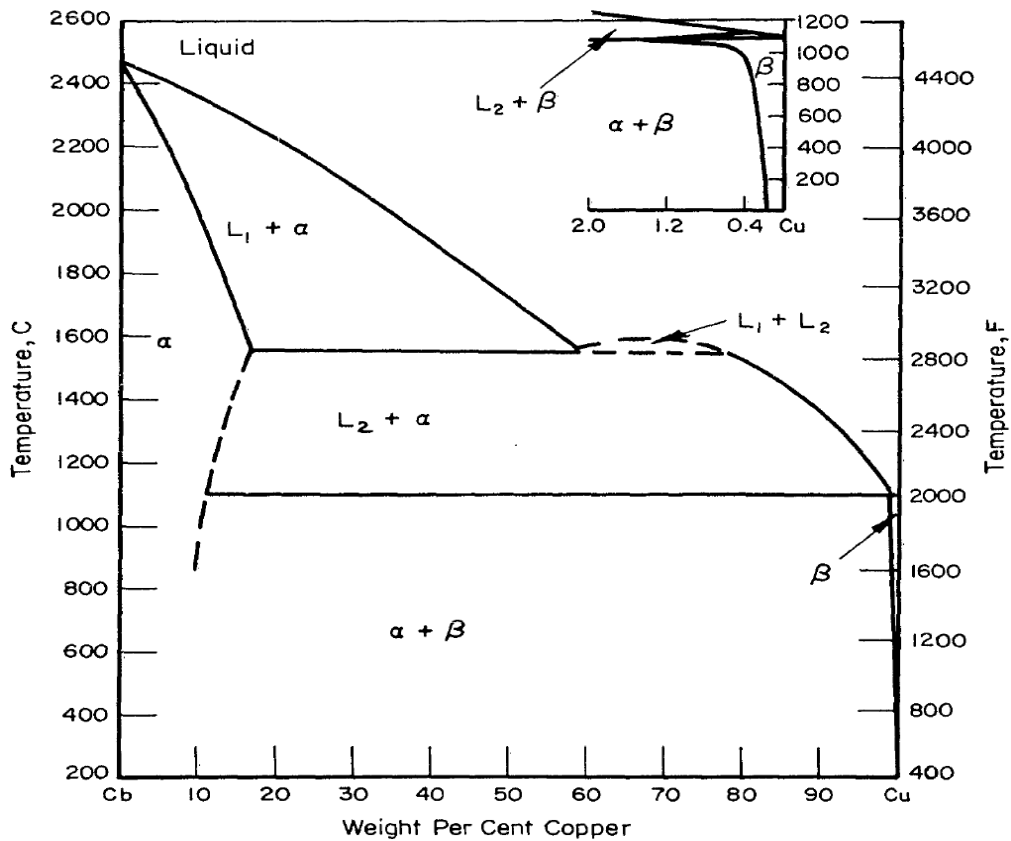
Figure 26: Copper-Niobium Equilibrium Phase Diagram [24]

2.4 Conclusions

- The primary conflicting objectives for extreme electrical contacts are maximizing wear resistance and minimizing Joule heating, which leads to minimizing electrical resistivity. Two possible models for maximizing wear resistance were identified and used to derive material indexes: (i) Archard's wear and (ii)

37

thermally assisted melt erosion. Tungsten alloys are non-dominated solutions for both wear mechanisms; consequently, these alloys are particularly promising for extreme electrical contact applications.

- To fill the "white spaces" of the Ashby material charts, opportunities of designing a hybrid material may offer significant improvement. Potential configurations include particulate composites, "open-faced" sandwich (coating, cladding), or layered structures. Property curves for hybrid material solutions plotted on Ashby plots suggest that potential performance increases of nearly an order of magnitude are possible based upon the projected wear properties of these composites compared to those of hardened copper.

- Plots of material metrics representing these conflicting objectives suggest that hardened copper and tungsten alloys are in the Pareto set (i.e., each is a non-dominated solution) for both wear mechanisms. The hardened copper values minimize electrical resistivity well, while tungsten alloys may be a better compromise between increased wear resistance while maintaining minimal electrical resistivity. Tungsten alloys are approximately four times more resistive than hardened copper, but they possess hardness and maximum service temperature increases by factors of three and seven, respectively. Tungsten carbide is 15 times harder than copper, while increasing resistivity by a factor of six. This suggests that one may be able to use tungsten alloys or even tungsten carbide to obtain greater durability if an increase in electrical resistivity is permissible.

- Analysis utilizing the EduPack Level 3 database provides a Pareto set of candidates that potentially provide a reasonable trade-off of minimal electrical resistivity and good wear resistance. If wear is controlled by hardness then, tungsten, molybdenum, copper-silver composites, copper alloys, and titanium diboride lie along the Pareto frontier, the materials with the best trade-off of properties for these two conflicting objectives. If wear is controlled by thermally-assisted melt erosion, then tungsten, molybdenum alloys, tantalum, tungsten alloys, tantalum alloys, copper alloys, copper-based composites, and molybdenum disilicide are potential candidates for mitigating the thermally-induced surface degradation.

- Several alternative configurations combining copper with another material were considered for extreme electrical contacts. Alternative configurations of coatings and particulate composites are suggested. Tungsten, cobalt, hafnium, tantalum, and molybdenum are particularly promising coatings/claddings due to their refractory and hardness properties. Several relatively conductive carbide reinforcements are identified as potential particulate constituents. Tantalum, tungsten, and tungsten-cobalt carbides are highlighted for their combination of hardness and conductivity properties. Tantalum, tantalum-tungsten, molybdenum alloys are non-dominated solutions for maximum service temperature. Molybdenum disilicide and titanium diboride are nearly non-dominated for both wear considerations.

- Comparison of widely utilized refractory materials (i.e., molybdenum, tantalum, iridium, and niobium) for hardness and maximum service temperature shows that

tungsten is nearly a non-dominated solution for both. It is slightly dominated by

iridium for hardness, but it only costs a fraction of iridium. So, tungsten is the

most viable choice as a refractory constituent in a hybrid material, with

molybdenum secondary.

Chapter 3: Literature Review on Cu-Matrix Composites

The materials selection study suggested that a hybrid material, filling the "white spaces" on the material property charts, could be even better. One of the potential classes of hybrid materials to explore is metal matrix composites (MMCs). In particular, copper-tungsten (Cu-W) composites may be interesting to study further. This chapter reviews past work on metal matrix composites with some emphasis on Cu-W composites.

3.1 Introduction to Metal Matrix Composites

3.1.1 Particulate MMCs

Particulate MMCs have constituents with relatively low aspect ratios approximately equal to unity. The particulate is well suited for three dimensional loading due to relatively isotropic properties. Particulate diameters and volume fractions usually fall in the range of 1-100 μm and 5-30%. As compared with other MMCs, production costs are on average comparably lower since existing metal forming practices and equipment can be readily employed to produce this type of MMC components [25].

3.1.1.1 Powder Metallurgical Production

3.1.1.1.1 Solid State Production

Solid state production (SSP) is characterized by temperature levels that are not sufficient to cause melting of metal matrix. An inclusive range of MMCs has shown superior mechanical properties when fabricated using SSP as compared to those achieved through liquid state production due to limited segregation and embrittlement interfacial reactions during these generally deformation driven methods [26].

Powder metallurgy is an example of SSP that utilizes powder matrix material. The matrix and particulate materials are mixed then consolidated. This step is in turn followed by a secondary processing plan. A number of factors concerning the particulate are very critical for achieving the desired mechanical properties in the MMCs. Particle size imposes a very significant determination of the resulting mechanical properties. In some cases the reinforcement particle is more than six times smaller than the matrix average powder particle size. The large particle size difference results in the production of agglomerates. These particle clusters have deleterious effects on the mechanical properties [27]. In attempts to ensure the most homogenous mixture possible, the powder blend is mixed through several different methods. Vibratory mixture is the most common practice employed to mitigate particle clustering. Mechanical alloying is a means of increasing powder mixture uniform distribution. Cyclic application of an external load causes dispersion and embedment of ceramic particles into metal matrix. Special care must be taken to limit opportunity for contamination and atmospheric reactions. Successful production of mechanically alloyed MMCs has been demonstrated by Li et al. [28]. Uniform particle sizes approaching nanometer ranges reduce the temperature and pressing time required to produce increased densification during consolidation.

3.1.1.1.2 Hot Pressing

Once adequate matrix-reinforcement powder mixture is accomplished, consolidation is typically the next step in MMCs fabrication. Most consolidation techniques rely on hot pressing and/or hot isostatic pressing. Tailoring of this step is based upon the unique requirements of the matrix and constituents. Generally, pressure is applied at a maximum temperature that will not produce damage to reinforcement or

yield a liquid matrix phase transition. Elevated temperatures allow for increased

diffusion rates and more complete diffusion within particle spacing [29].

3.2 Material Processing Influences

Jankovic et al. [30] have evaluated the implications of processing variations on

physical and mechanical properties of functionally graded copper-tungsten composites.

Three tungsten self-formed packing structures are produced through variations in

vibratory compaction times, sintering hold times, and sintering temperatures. These

packing structures are subsequently infiltrated with molten copper during sintering. The

W concentration profile for sintering temperatures at 1723 K yield W vol. % ranging

from 100% to 70%; however, at 2073 K the concentration gradient is between 100% and

15%.

The dependence of electrical resistivity on vibration time and W contiguity is

shown in Figure 27. The data presents a monotonic trend between vibratory compaction

times, W contiguity, and consequently electrical resistivity.
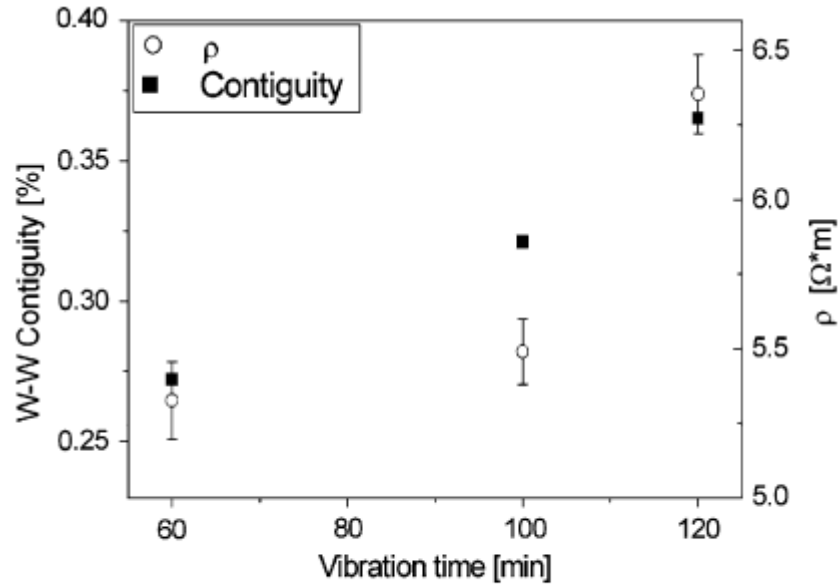
Figure 27: Electrical resistivity (ρ) and contiguity of W phase as function of vibration duration in the sample sintered at 1723 K for 3 hrs. [30]

The temperature dependent electrical conductivity of the W-Cu specimens produced in this study is presented in Figure 28. The slope for each material is nearly linear. A transition in resistance behavior occurs at 673 K. This transition is attributed to W connectivity and residual stresses.
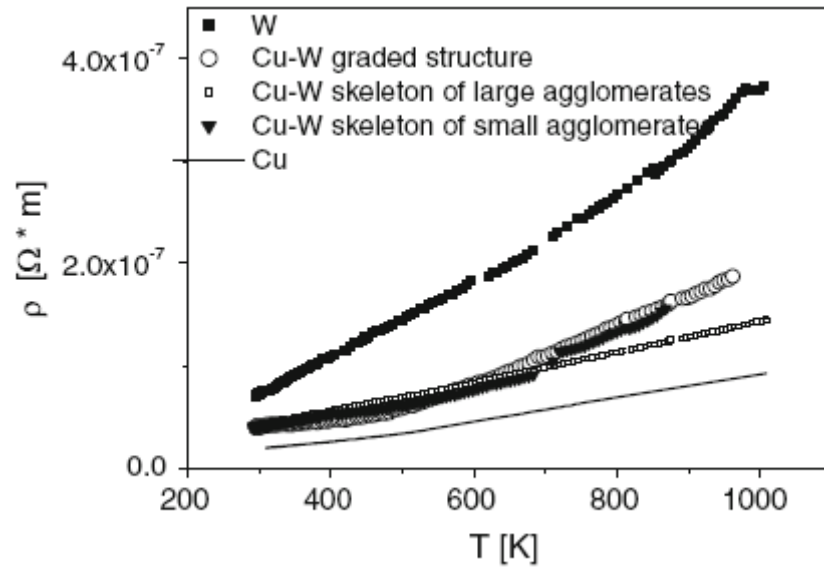
Figure 28: Electrical resistivity (ρ) as function of temperature for functionally graded Cu-W composites with 70-100 W vol.%, pure Cu, and W [30]

A set of optimal sintering parameter levels was determined in attempts to optimize hardness and density properties [31]. Manipulation and distribution of particle size are means by which the sintering process can be adjusted to yield enhanced densification and mechanical properties (e.g. hardness) as illustrated in Figure 29. By adding small (B) W particles (2.2-5.0μm) with larger particles (38.9-76.8μm), relative density can be increased [31]. The plot in Figure 30 shows that density increases with content of small W particles up to a concentration level of 20%, after which, relative density rapidly degrades. The small W particles, in conjunction with Cu, are able to fill in the pores produced adjacent to the large W particles.
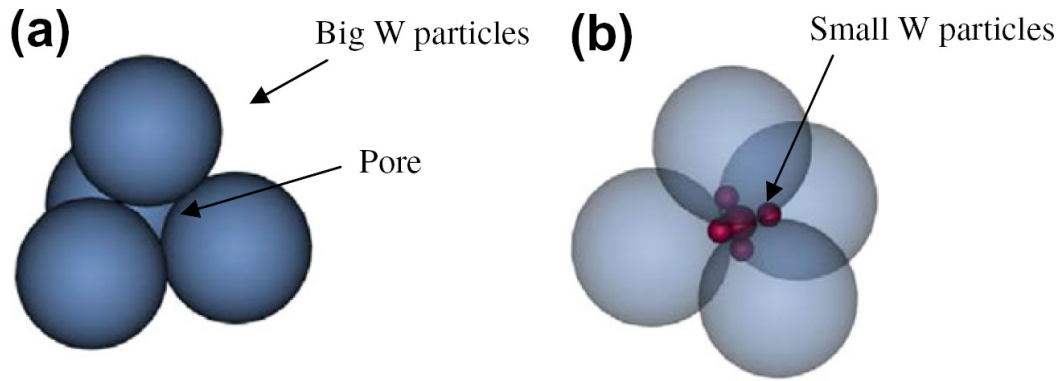
Figure 29: Distribution patterns of W powders and pores formed by W powders (a) distribution pattern of tetrahedron and (b) small W particles in the pore [31].
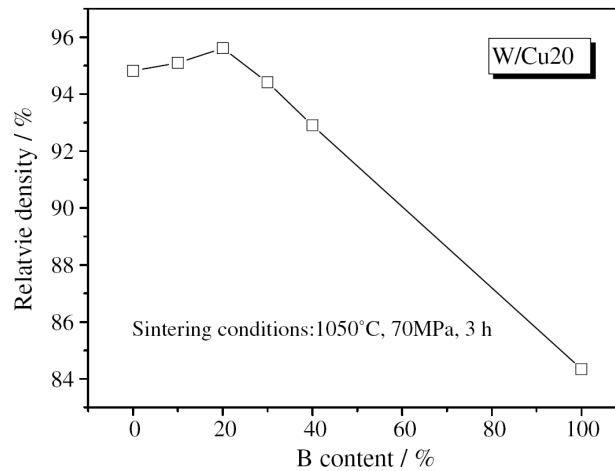
Figure 30: Variation of relative density for 80W-20Cu (mass %) or 65W-35Cu (vol.%) with % (2.2-5.0μm) content of particle size W [31]

The effects of sintering temperature on relative density and hardness are graphically represented in Figure 31 and Figure 32, respectively. At sintering temperatures 1050°C, 1060°C, and 1070°C, the increasing relative density correlates with increasing Cu content. The 48W-52Cu (vol.%) and 32W-Cu68 (vol.%) materials reach a maximum hardness value at 1060°C, beyond this point the hardness value decreases due to partial melting of the copper constituent. The hardness of the 65W-35Cu (vol.%) continues to increase at temperatures exceeding the melting temperature.

46
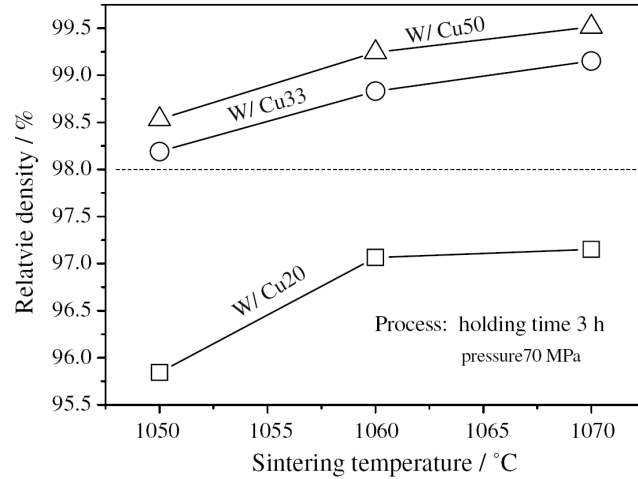
Figure 31: Effects of sintering temperature on relative density of different W-Cu layers [31]
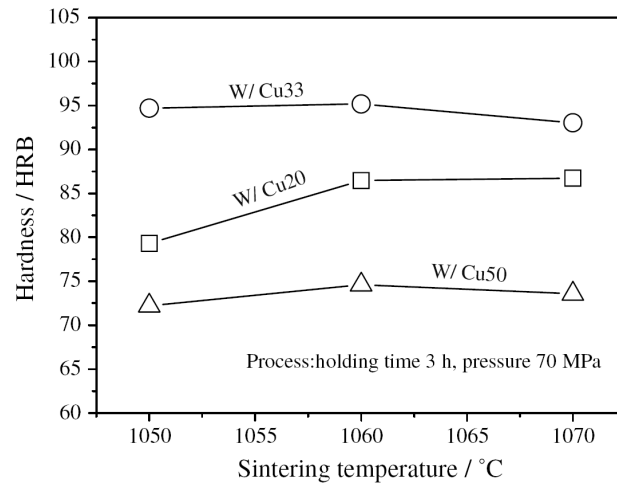
Figure 32: Effects of sintering temperature on hardness of different W-Cu layer [31]

Relative density increases with sintering pressure for all three W-Cu compositions as shown in Figure 33. A maximum relative density exceeding 99% is achieved for sintering pressures of 85 MPa.

47
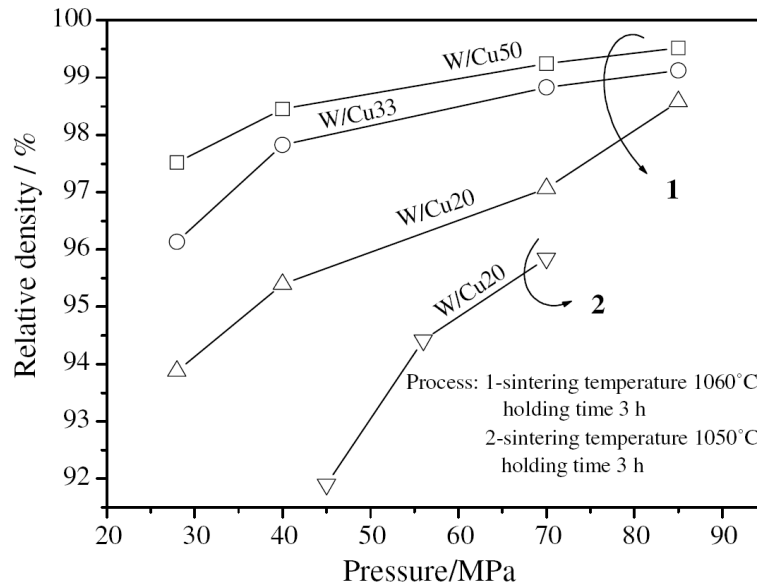
Figure 33: Effects of pressure on relative density of 65W-35Cu (vol.%), 48W-52Cu(vol.%), and 32W-68Cu (vol.%) [31]

The level of shrinkage during sintering caused by the combined effects of temperature, pressures, and hold time is shown in Figure 34. The processing parameter levels to obtain a fully dense composite are as follows: sintering temperature of 1060°C, pressure of 85 MPa, and hold time of 2-3 hours.
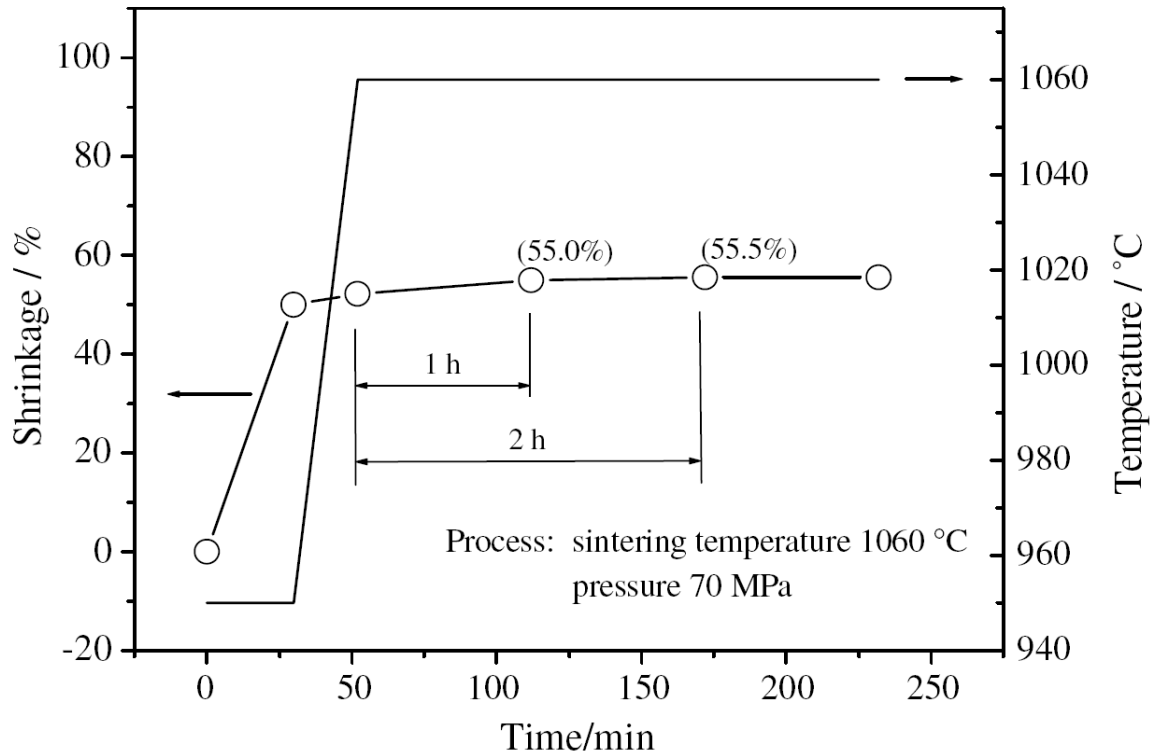
Figure 34: Effect of holding time on shrinkage under different sintering temperatures [31]

It is determined that composites produced by additional steps of re-pressing and re-sintering yield enhanced mechanical properties as compared with those manufactured through a single pressing and sintering stage [37]. Composite materials comprised of coated particles possessed density, hardness, and ultimate tensile strength properties that exceeded those obtained by uncoated particles. Each of these properties is also increased as the volume fraction is reduced.

The critical particle concentration is based primarily on matrix-particle powder size ratios [27]. Young's Modulus, yield strength, and ultimate yield strength properties decline once either critical size or concentration ratio is exceeded. Minimal dependence on matrix ductility is demonstrated [27].

3.3 Composite Constituent Investigation

Ultrasonic agitation during electroless plating of particles improved uniformity in particle distribution, hardness, ultimate tensile strength, yield strength, elongation, relative density, and electrical conductivity [33]. The improvement of mechanical and electrical properties by electroless plating is illustrated in Table 2. The 1μm particle yields superior mechanical properties as opposed to larger 20 μm particle at room temperatures. For both particle sizes, the coated materials have superior mechanical properties in each of the observed categories. Comparison of the 1 μm W at 3 vol.% composite and pure annealed Cu mechanical properties, as shown in Figure 35 and Figure 37, shows an approximate increase of 160%, 150%, 230%, and 160% in hardness, ultimate tensile strength, yield strength, and elongation, respectively.

Table 2: Properties of repressed/re-sintered W-Cu composite powders with 3 vol.% W addition under ambient conditions [33]

W particle	Condition	Relative density (%)	Electrical conductivity (%IACS)	Hardness (Hv)	Ultimate tensile strength (MPa)	Yielding strength (MPa)	Elongation (%)
1 μm	Condition 1	97.3	85.7	71	250	95	16
	Condition 2	98.5	94.6	79	295	135	46
20 μm	Condition 1	93.9	88.4	70	227	67	32
	Condition 2	96.8	93.9	74	289	120	46
Pure copper		–	96.5	50	201	58	28

Condition 1: without electroless Cu plating.
Condition 2: electroless Cu plating.

The mechanical and physical properties of pure Cu are shown to be substantially bolstered through the use of copper coated tungsten particles, even for elevated temperatures. The broad trend observed in each plot shows the inverse relationship between W particle size and mechanical properties. Elongation properties are nearly equal to room temperature properties for composites incorporating the 1 μm W particle. Figure 38 illustrates the marginal reduction in electrical conductivity over the

50

temperature range due to the implementation of the copper coated tungsten particles. The electrical conductivity of the pure copper is nearly equivalent to that of the 1 μm W particle composite. At 300°C, the 1 μm tungsten at 3 vol.% shows an improvement over pure copper by a factor of 9.2, 3.2, 24 for yield strength, ultimate tensile strength, and elongation, respectively.
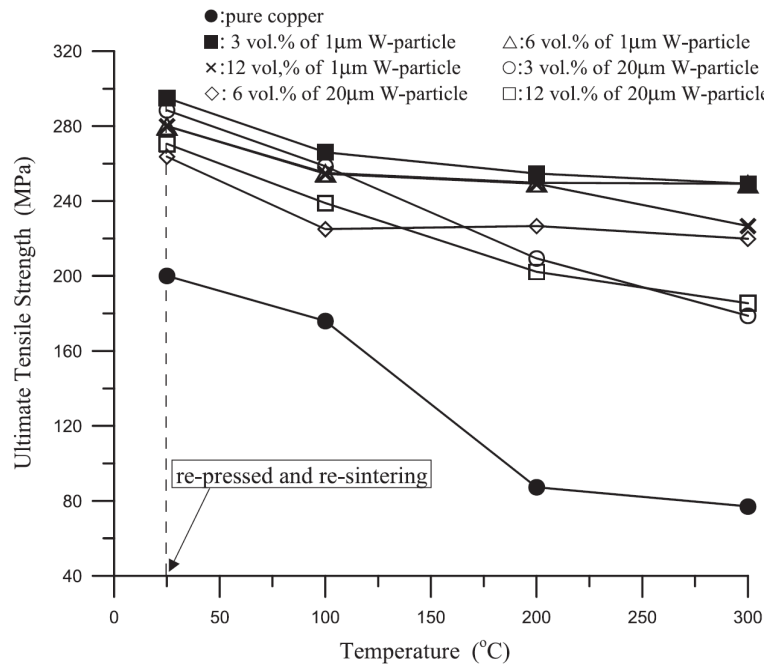
Figure 35: Temperature-dependent variation of UTS of pure Cu samples and W-Cu composite [33]
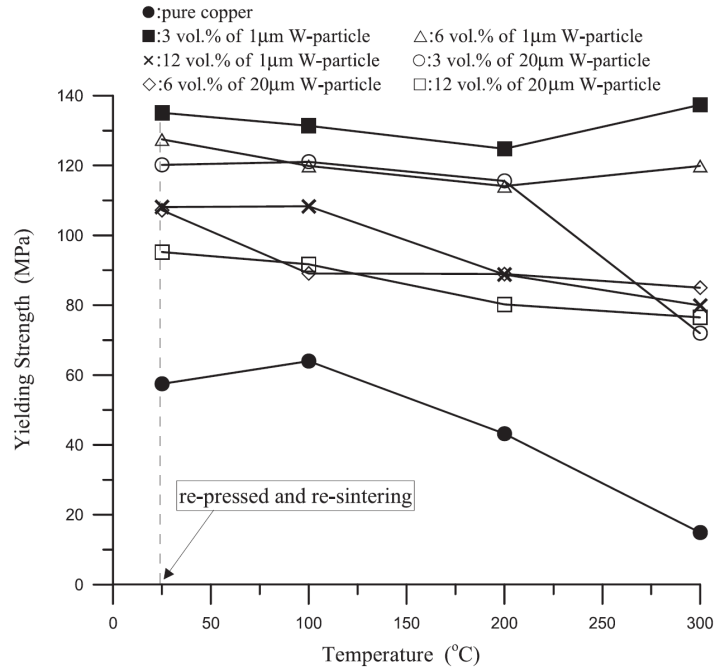
Figure 36: Temperature-dependent variation of yield strength of pure Cu samples and W-Cu composite [33]
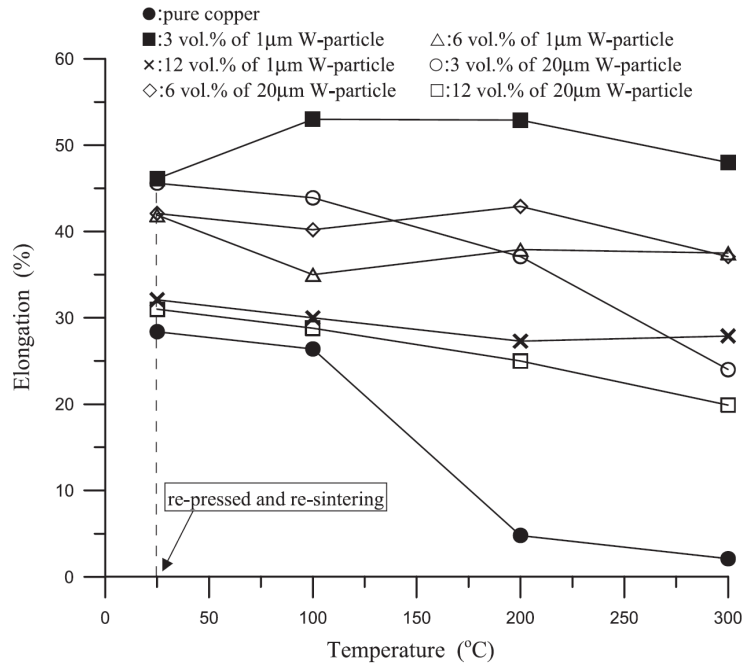
Figure 37: Temperature-dependent variation of elongation of pure Cu samples and W-Cu composite [33]
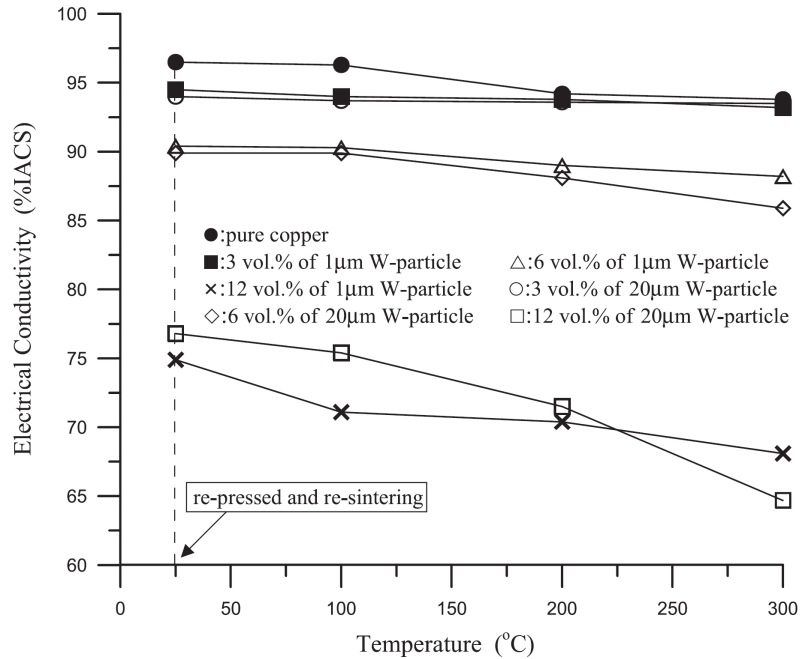
Figure 38: Temperature-dependent variation of electrical conductivity of pure Cu samples and W-Cu composite [33]

Zhang et al. [34] have utilized conductive ternary carbides to strengthen copper through powder metallurgy methods, resulting in composites with superior mechanical properties as compared to those of pure copper and graphite-copper composites. The electrical conductivity is reduced by less than 3% IACS for 5 vol.%.

Volume fractions of 15% or less permit near full theoretical density of 98% as shown in Figure 39. The 5 vol.% and 10 vol.% microstructures, presented in Figure 40 (a) & (b), show a uniform dense microstructure.
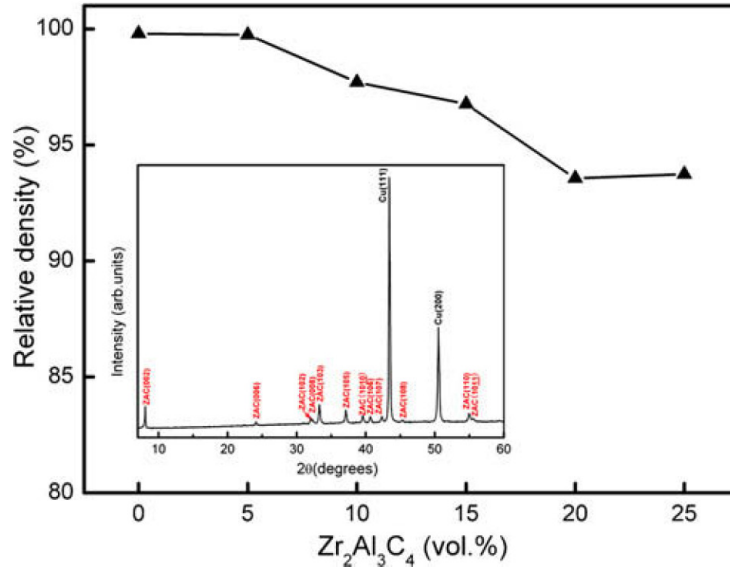
Figure 39: Relative density of Cu/ Zr$_2$Al$_3$C$_4$ composites plotted as a function of particle content. Inserted XRD pattern presents the phase composition of the Cu/25 vol.% Zr$_2$Al$_3$C$_4$ composite. [34]
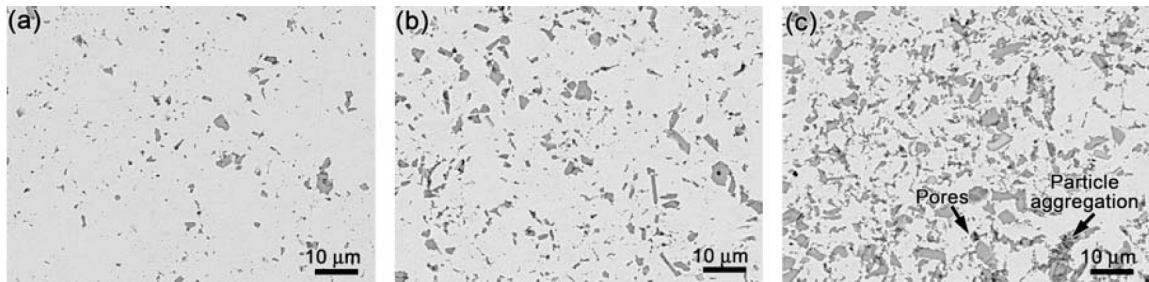
Figure 40: Distribution of Zr$_2$Al$_3$C$_4$ particles in (a) Cu/ 5 vol.% Zr$_2$Al$_3$C$_4$, (b) Cu/ 10 vol.% Zr$_2$Al$_3$C$_4$, (c) Cu/ 25 vol.%Zr$_2$Al$_3$C$_4$ [34]

The copper matrix develops a mechanical bond with the particle during cooling due to the difference in thermal expansion coefficients.

The addition of the Zr$_2$Al$_3$C$_4$ particle significantly improves the mechanical properties of the composite material as illustrated in Table 3. The fracture toughness and flexural strength are both optimized by 10 vol.% particle concentration or less. Hardness values increase with further additions of particle, but minimal gains are observed past 20 vol. %. The electrical properties at room temperature are reported in Table 3. The particle concentration and electrical conductivity are inversely related.

54

Table 3: Room temperature properties of pure annealed copper and Cu/ $Zr_2Al_3C_4$ composites [34]

	HRB	Flexural strength (MPa)	Fracture toughness (MPa$\cdot$m$^{1/2}$)	IACS (%)
Pure cooper	28.0 ± 0.35	181.5 ± 6.2	–	89.6
Cu/5 vol.% $Zr_2Al_3C_4$	40.5 ± 0.88	353.7 ± 5.6	10.40	86.9
Cu/10 vol.% $Zr_2Al_3C_4$	49.5 ± 0.46	333.7 ± 8.8	10.24	76.1
Cu/15 vol.% $Zr_2Al_3C_4$	55.5 ± 0.39	309.2 ± 7.6	9.19	63.5
Cu/20 vol.% $Zr_2Al_3C_4$	61.5 ± 0.45	291.5 ± 1.0	4.38	50.7
Cu/25 vol.% $Zr_2Al_3C_4$	65.3 ± 0.67	217.4 ± 9.0	2.32	42.1

Tungsten carbide and cobalt particulate are shown to increase the bulk hardness and wear properties of CuMC [45]. Three groups of composite materials are fabricated with particle wt.% ranging from 5-20% and size ranging from 1-9 μm. All of the materials produced reach densification levels of nearly 98%, except for the Co particulate composite. The bulk hardness of the CuMC is shown to increase with increasing particle concentration or decreasing particle size. A Hall-Petch type of strengthening mechanism is revealed.

The additions of the hard WC and Co particles yield wear resistances significantly higher than pure copper. The trend of wear resistance as a function of particle concentration and size closely follows the observations for hardness. Although the CuMC reinforced with WC and Co possesses lower hardness, the wear rate for this material is equal to, or in some instances, less than the harder WC reinforced copper matrix materials. SEM analysis of wear surfaces for Co particulate material did not show any surface cracking or pulled out particle. This result is in agreement with previous investigations of Co effects on metal matrix composites [46].

3.4 Strengthening Mechanisms

The tungsten particle size effect in CuMC is investigated for shear loading conditions [41]. 10μm and 30μm diameter W particle at 80, 70, 60 wt.% concentrations were evaluated to determine shear driven deformation. The smaller tungsten particle size

is shown to increase the shear stress levels at concentration levels, as highlighted in Figure 41. The increased shear stress levels are derived from the increased resistance to deformation in the composites. An increase in shear stress is also characterized by an increase in W concentration levels. The impact of concentration level is most pronounced at 80W-20Cu (mass %) or 65W-35Cu (vol.%).

Two different failure mechanisms are visualized in Figure 42. The reduced stresses associated with lower W concentration produce diffused deformation in which the vast majority of deformation proceeds with the pliable Cu matrix, Figure 42(b). However, for the smaller shear zone width, the stress level is sufficiently large to yield W particles and the deformation progresses through the copper and tungsten constituents, as in Figure 42 (a).
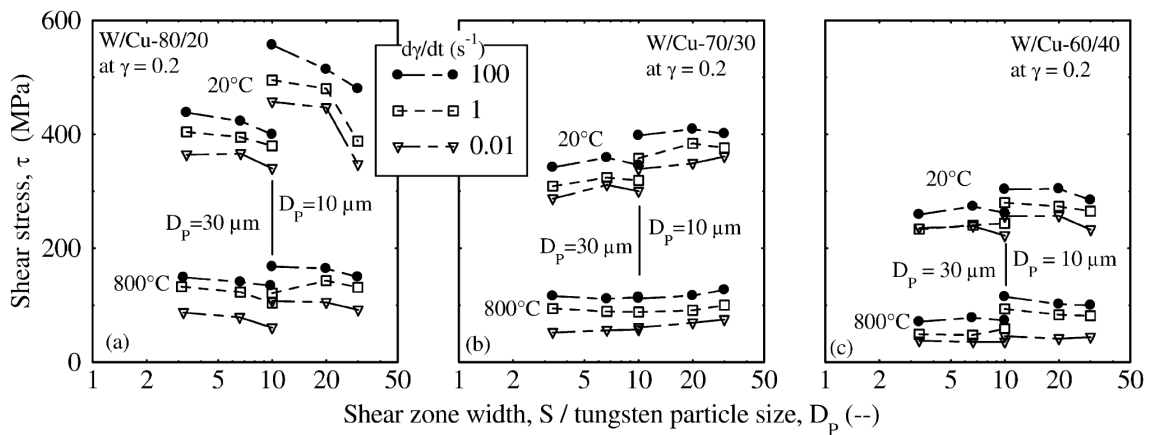
Figure 41: Size effects under shear deformation of W/Cu-80/20, W/Cu-70/30, and 60/40, with tungsten particle sizes (D_p) of 10 µm and 30 µm [41]
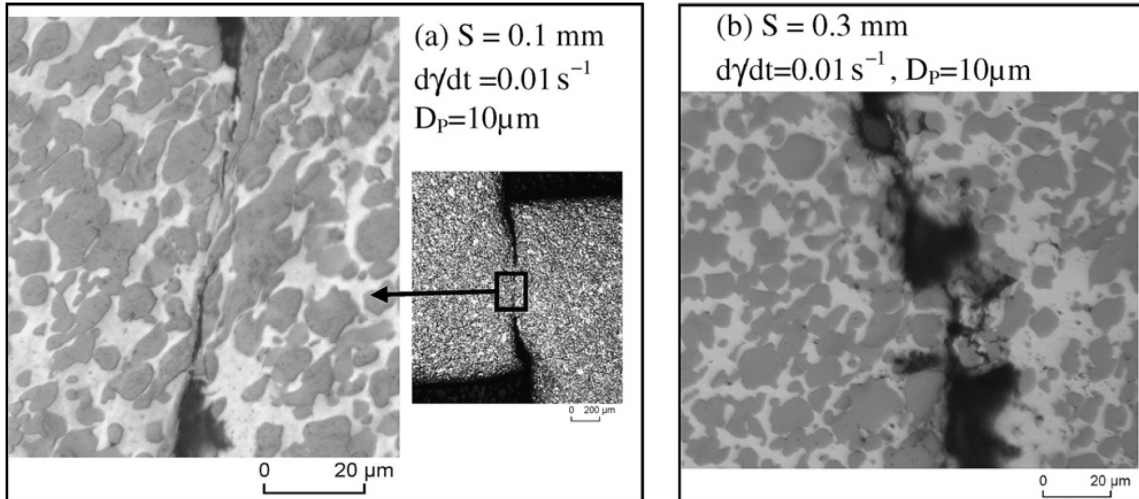
Figure 42: Effect of shear zone width (S) on the fracture mechanism of 10μm W/Cu-80/20 wt. % at 20°C [41]

CuMCs consisting of 0.5-1 vol. % ZrC and 0.5%-1 vol.% ZrB$_2$ exhibit tensile strengths more than three times that of wrought pure copper. Strengthening mechanisms are attributed to resistance to dislocation slip by particles inside grain interiors and along sub-grain boundaries [42]. Introduction of these particles also yields grain refinement, resulting in Hall-Petch strengthening.

3.5 Impact of Particle Coatings

Brinell hardness and bending strength properties of CuMC are higher for Cu coated SiC particles than uncoated SiC particles [35]. Porosity increases nearly linearly with additions of coated particulate. SEM microstructure analysis reveals limited porosity for the 30 vol.% SiC concentration. Clean well-bonded SiC-Cu matrix interfaces are attributed to the Cu coating.

Brinell hardness is observed to peak at 40 vol.% for both uncoated and coated particles. Higher bearing capacity is attributed to the good bonding at the interface

resulting from the electroless copper plating, and the lower porosity due to improved powder fluidity [35].

The bending strength decreases with increasing volume fraction for both uncoated and coated particles, due to the increase in porosity. The annealing is shown to reduce the strength properties as well.

CuMC with 20 vol.% uncoated and Ni coated SiC and Al_2O_3 particles were fabricated and characterized based on sintering response, microstructure, density, 0.2% proof stress, fracture stress, and elongation [36]. Nickel is selected as a coating material because it forms a solid solution with Cu.

Porosity increases with uncoated particles. Good interfacial adhesion is observed (i.e. nearly no visible porosity) between the Ni coated particles and Cu matrix. SEM images reveal closed and interconnected porosity in the vicinity of the uncoated particles [36].

The compression properties of each material are presented in Table 4. The yield and fracture strengths of the uncoated reinforced composites are approximately 21% and 40% of the coated reinforced composites, respectively. The superior mechanical properties for the coated particles are attributed to good adhesion at the matrix-particle interface.

Table 4: Compression properties of Cu-20 wt.% (un)coated SiC and Cu-20 wt.% (un)coated Al_2O_3 composites [36]

Materials composition	0.2% proof stress (MPa)	Fracture strength (MPa)	Elongation (%)
Cu−20% coated SiC	83	344	43.6
Cu−20% SiC	16	135	30.4
Cu−20% coated Al_2O_3	62	285	48.4
Cu−20% Al_2O_3	14.1	112	33.2

Coating of tungsten wires to improve interfacial shear resistance is achieved [38]. Tungsten whiskers were CVD coated with single annealed copper and annealed copper/tungsten multilayers. Single fiber specimens were subjected to fiber push-out test via macro-indentation experiments.

The single copper layer exhibited appreciable interfacial shear resistance. The area under the copper mono-layer curves shown in Figure 43 implies more energy absorption than the Cu/W multi-layer coating. The mono-layer absorbs nearly 50% more energy than multi-layer Cu/W coatings. The Cu/W multi-layer coating exhibited push-out behavior typically associated with brittle interfaces. There are no improvements with additional copper in multi-layer coatings.
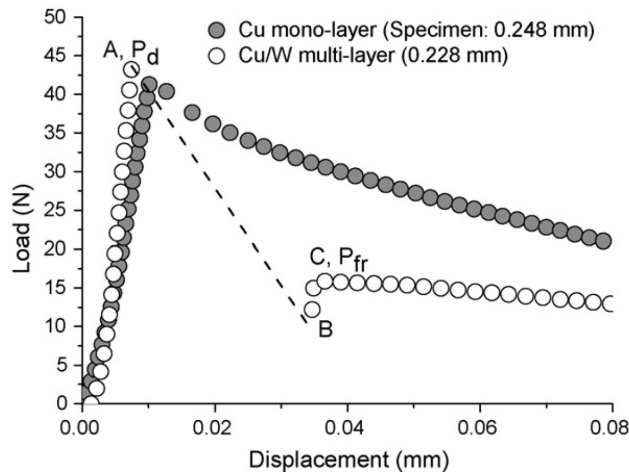
Figure 43: Measured push-out load vs. fiber-end displacement curves for the Cu single-layer and the Cu/W multi-layer coated interface. Specimen thickness was 0.248 and 0.228 mm, respectively [38].

Copper coating yielded stronger particle-matrix interfacial bonds and subsequent increases in load transfer, resulting in approximately three times the strain to failure of non-coated particle [39]. Debonding of uncoated constituents from the matrix is determined to be the cause of failure. Particle pullout (i.e. particle decohesion from

59

matrix) indicates weak matrix-particle bonding and minimal load transfer to particle, as observed for non-coated particles [39].

Relative density, bending strength, modulus, and ductility are shown to decrease with increasing volume fraction of copper coated SiC [40]. A maximum hardness value is optimized at 50 vol.% SiC and then reduces for additional SiC additions. The bending strength of the composite is optimized at 20 vol.% SiC. The increasing porosity reduces the strength values at higher particle concentration levels. Young's modulus is highest at 20% particle content. Large porosity associated with the higher concentration levels permits relatively unrestricted crack propagation through these microstructure imperfections.

Cr interlayers applied to the SiC fiber are shown to yield drastically improved adhesion properties [47]. The utilization of Cr interlayers yielded push-out loads in excess of three times that of uncoated SiC fibers, as presented Figure 44.
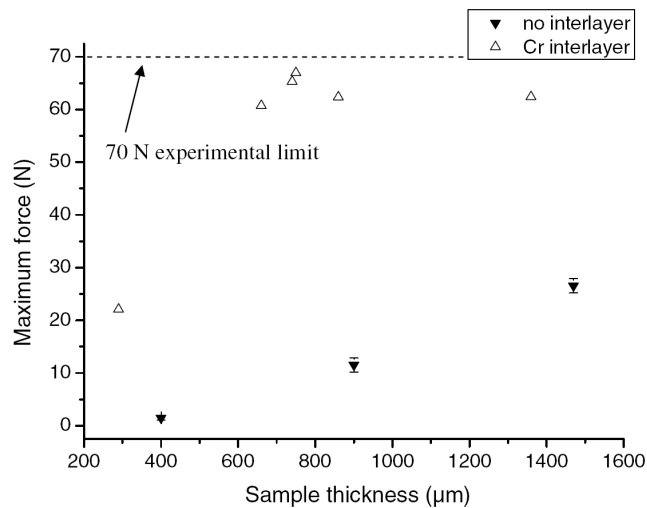
Figure 44: Comparison between push-out results of SiC-Cu composites with as-received and Cr coated fibers [47]

In CuMC, 30% increase in ultimate flexural strength is observed for Fe coated carbon fibers compared with non-coated fibers. The interface bonding transitions from a purely mechanical bond (uncoated carbon fiber) to a chemical bond (Fe coated carbon fiber), resulting in superior bond strength and particle structural integrity yielding increased performance [48].

Intermetallic layers of Mo on graphite have been shown to improve the wetting and adhesion of graphite particles in Cu matrix [43]. Improvements in mechanical properties are accredited to the resistance of void formation and delaminating of particle. Demonstration of advanced interfacial bonding performance achieved through Mo interlayer additions is displayed in Figure 45. Bonding improvements are indicated by increases in adhesion strength of copper coatings on Mo surfaces. The indication of minimal Mo interlayer delaminating is validated through sustained repeated stress levels during subsequent cycles in Figure 46 [43], [44].
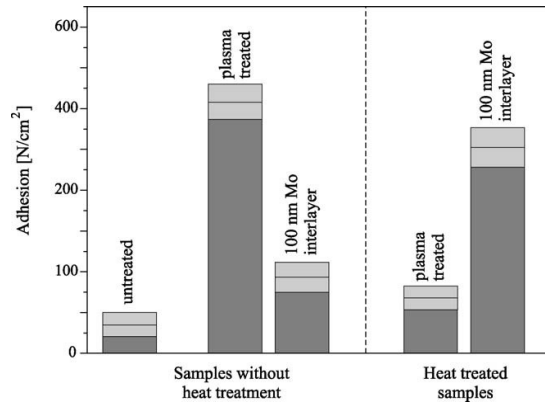
Figure 45: Adhesion Strengths for Coated Carbon Substrates [43]
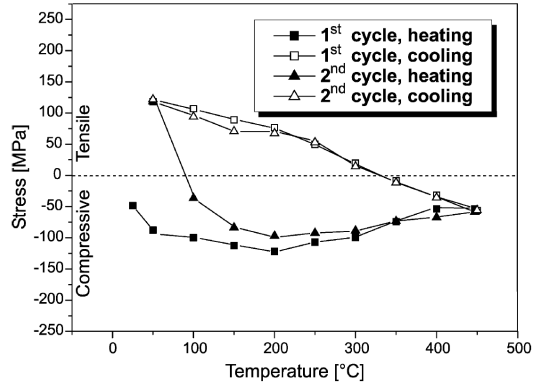
Figure 46: Thermally Induced Tensile/Compressive Stresses on C substrate [43]

Chapter 4: Effective Properties of Composites

The properties of hybrid materials depend on the volume fraction of the constituents and how they are configured in the structure. To explore candidate materials that fill white spaces, the hybrid properties need to be estimated. This chapter analyzes how the relevant properties can be estimated. Here, the focus is on particulate reinforced composites.

Simple models or functional forms have been developed that estimate mechanical and physical properties based on relevant microstructural parameters including volume fraction, morphology, and configuration of the constituents. Properties of particular interest include modulus of elasticity, strength, and electrical conductivity. Other properties that are often described are density, fracture toughness, and wear resistance. This review focuses primarily on models expressed as functional forms applicable to particulate reinforced metal matrix composites.

4.1 Density

4.1.1 Rule of Mixture

The density of the composite is readily determined by a simple rule of mixtures,

$$\rho_c = f_1\rho_1 + f_2\rho_2 \tag{1}$$

where ρ is density and subscripts 1, 2, and c refer to constituent 1, constituent 2, and composite, respectively. f is constituent concentrations by volume. This relationship is suitable regardless of constituent morphology. This rule of mixture is applicable for composites with limited or negligible porosity.

4.2 Elastic Modulus

4.2.1 Rule of Mixture

When uniform strain throughout the microstructure is assumed, the Voigt model effectively leads to a simple rule of mixture function form that provides an elastic modulus upper bound for particulates [49]. Using the isostrain condition and static equilibrium, the stress is the volume average of the local stresses, and as a result composite moduli is given by

$$M_c = f_1 M_1 + f_2 M_2 \qquad (2)$$

where M is Young's, shear, or bulk modulus. Elastic properties are typically matrix dominant properties [50]. Generally, this equation has limited accuracy for particulate composites with high particle volume fractions [49], [51]. This volume fraction threshold above which rule of mixture is not accurate varies according to microstructure factors (e.g. matrix-reinforcement material, processing parameters, interfacial bond strength, etc.). Using the isostress condition, a lower bound is given by

$$M_c = \frac{M_1 M_2}{f_1 M_2 + f_2 M_1} \qquad (3)$$

4.2.2 Strain and Stress Energy Derived Moduli Bounds

The following elastic modulus relationships are derived as a consequence of several simplifying assumptions. The reinforcement particles are taken to be appropriately dispersed such that the microstructure can be considered on average uniform. Consequently, the displacement and traction on the surface of a representative volume are macroscopically uniform. Both constituents are assumed isotropic and

elastically homogeneous; therefore, stress and strain energies are simplified for the isotropic homogenous case [52]. This simplification allows for the strain energy W^ε and stress energy W^σ to be succinctly expressed as follows:

$$W^\varepsilon = \frac{1}{2}\left(9K^*\bar{\varepsilon}^2 + 2G^*\bar{e}_{ij}\bar{e}_{ij}\right)$$

$$W^\sigma = \frac{1}{2}\left(\bar{\sigma}^2 / K^* + \bar{s}_{ij}\bar{s}_{ij} / 2G^*\right)$$

(4)

where $\bar{\varepsilon}$ and $\bar{\sigma}$ are the isotropic part of average strain and stress, respectively. $\bar{s}_{ij}$ and $\bar{e}_{ij}$ are the average stress and strain, respectively. K^* and G^* are effective bulk and shear moduli, respectively. Paul [52] utilizes principles of minimum potential and complementary energies in conjunction with linear displacement or constant stress to obtain primitive bounds,

$$K^*_{(-)} = [\sum v_n / K_n]^{-1} = \frac{\overline{1}}{K}$$

$$K^*_{(+)} = \sum K_n v_n = \overline{K}$$

(5)

$$G^*_{(-)} = [\sum v_n / G_n]^{-1} = \frac{\overline{1}}{G}$$

$$G^*_{(+)} = \sum G_n v_n = \overline{G}$$

(6)

v_n is the volume fraction of constituent n. It should be noted that these relationships provide the inputs for determining Young's modulus, as presented in the following analysis. For concept design of hybrid materials, these simple classical bounds are often sufficient. But they would not be sufficient for detailed design of hybrid materials [51]. In the next sections, improved bounds are provided.

4.2.3 H-S Elastic Modulus Bound

Refinements of these bounds were achieved by Hashin and Shtrikman [54] through variational principles in terms of the elastic polarization tensor [55]. The basis for this variational approach is founded on the deviation between the stress-strain relationship of an isotropic homogenous and an anisotropic heterogeneous material. For the isotropic material, the stress-strain relationship is accurately described by Hooke's law as:

$$\sigma^o{}_{ij} = C^o{}_{ijkl}\varepsilon^o{}_{kl} \tag{7}$$

A symmetric stress polarization tensor is defined to relate the constant elastic modulus of the isotropic material to those of anisotropic material. The volume integral is taken over the entire body to yield the strain energy [55]. Hashin and Shtrikman developed the following lower and upper extremum for moduli properties [54].

$$K^*_{(-)} = K_1 + \frac{v_2}{1/(K_2 - K_1) + 3v_1/(3K_1 + 4G_1)}$$
$$K^*_{(+)} = K_2 + \frac{v_1}{1/(K_1 - K_2) + 3v_2/(3K_{21} + 4G_{21})} \tag{8}$$

$$G^*_{(-)} = G_1 + \frac{v_2}{1/(G_2 - G_1) + 6v_1(K_1 + 2G_1)/5G_1(3K_1 + 4G_1)}$$
$$G^*_{(+)} = G_2 + \frac{v_1}{1/(G_1 - G_2) + 6v_2(K_2 + 2G_2)/5G_2(3K_2 + 4G_2)} \tag{9}$$

for $K_1 < K_2$ and $G_1 < G_2$. Applications of these bounds have been applied to numerous material properties [51], [54]. The conventional relationship remains applicable for Young's, bulk, and shear modulus described by

$$E_\pm = \frac{9K_\pm G_\pm}{3K_\pm + G_\pm} \tag{10}$$

4.2.4 Walpole Refinement

Walpole [53] formulated a refinement of the relationships developed by Hashin and Shtrikman [51]. In this work, Green's function is utilized toward deriving the bounds in conjunction with classical extremum principles yielding in

$$\frac{f_1}{1+(K_1-K_2)f_2/(K_2+K_l^*)} \le \frac{K_c-K_2}{K_1-K_2} \le \frac{f_1}{1+(K_1-K_2)f_2/(K_2+K_g^*)} \tag{11}$$

where K_l^*, K_g^*, G_l^*, and G_g^* are derived from the minimum and maximum values of the constituent materials as specified by

$$K_g^* = \frac{1}{3}G_g, K_l^* = \frac{1}{3}G_l$$

$$G_l^* = \frac{3}{2}\left(\frac{1}{G_l} + \frac{10}{9K_l+8G_l}\right)^{-1} \tag{12}$$

$$G_g^* = \frac{3}{2}\left(\frac{1}{G_g} + \frac{10}{9K_g+8G_g}\right)^{-1}$$

The shear modulus, G^*, is calculated by the same relationship presented above. K and G are the bulk and shear modulus of the constituents, respectively. Subscripts l and g refer to the lower and greater value specified by each constituent, respectively. Using the bounds for a WC-Co alloy, the Young's modulus is bounded quite well [54], as shown in Figure 47. The applicability of this model is limited to modulus ratios of approximately 10 [51].
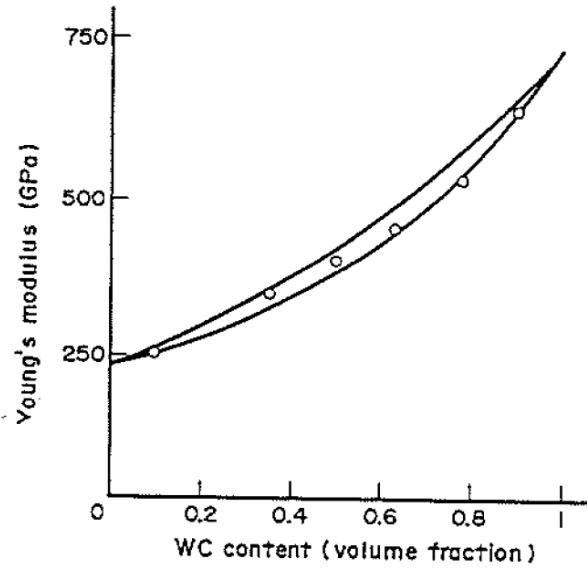
Figure 47: Hashin-Shtrikman bounds for Young's modulus of a WC-Co alloy [54]

4.3 Yield Strength

Deriving bounds for yield strength is considerably more challenging due to the distribution of stress in the heterogeneous microstructure. The impact of multiple strengthening mechanisms in each of the constituents as well as strengthening mechanisms related to the interactions of the constituents further complicate modeling efforts.

4.3.1 Lenel and Ansell Model

Lenel and Ansell [56] developed simple relationships on the basis of a dislocation pile-up strengthening mechanism in particulate reinforced MMC. Strengthening is assumed to occur due to dislocation pile-up in matrix near particle-matrix interfaces. The composite material is assumed to yield once the applied stress is sufficient to fracture the reinforcement particle. The particle is assumed to provide the source of dislocation

density. The primary resistance to dislocation movement is attributed to the particle induced dislocation densities. The fracture stress of the particle is taken to be directly proportional to the particle shear modulus, resulting in the relationship:

$$F = \mu^* / C \tag{13}$$

where F is the fracture stress of the reinforcement, μ^* is the shear modulus of the particle, and C is a proportionality constant which is on the order of 30. The yield strength of the composite σ_c follows.

$$\sigma_c = \sqrt{\frac{\mu b \mu^*}{2\lambda C}} \tag{14}$$

Alternatively, the composite yield stress can be expressed in terms of the reinforcement volume fraction. The mean interparticle spacing is related to the volume fraction and average particle radius through [57], [58]:

$$\lambda = \left(\frac{2\pi}{3f}\right) \bullet r \tag{15}$$

r and f are the average particle radius and reinforcement volume fraction, respectively. Substitution of this approximation into the preceding yield stress equation results in the equation:

$$\sigma_c = \left(\frac{\mu b \mu^* f^{0.5}}{2.89 r C}\right)^{0.5} \tag{16}$$

These yield strength relationships clearly demonstrate that a reduction in particle size and interparticle spacing result in increased composite yield strength. An increase in reinforcement volume fraction increases yield strength. These observations point to

increased dislocation density and grain size refinement as the primary strengthening

mechanisms. Microstructural influences imposed by residual thermal stresses associated

with differences in coefficients of thermal expansion are not captured by this model.

It is important to note that sufficiently small interparticle spacing could lead to

secondary strengthening through Orowan mechanisms, dislocation pinning by

reinforcement particles [59],[60]. The advantages of Orowan mechanisms have been

demonstrated by several MMCs that utilize nanoscale reinforcements in conjunction with

high volume fractions [61].

4.3.2 Matrix Flow Impedance

For microstructures characterized by well-bonded, non-deforming reinforcements

dispersed in a ductile matrix, reinforcement constrained matrix flow leads to the

development of tensile strength models that relate yield strength to volume fraction as

follows:

$$\sigma_c \approx \sigma_m \left(\frac{1}{1 - 1.73 \left(\frac{f}{\pi} \right)^{\frac{1}{2}}} \right) \tag{17}$$

where f is reinforcement volume. σ_c and σ_m are composite and matrix yield strength,

respectively. This relationship is considered an upper limit as it is based on the situation

in which both constituents yield simultaneously, as opposed to yielding of either

component individually [62].

4.3.3 Reinforcement Dislocation Pinning

This model derived by Zhao et al. [63] uses the idea of the Hall-Petch theory, such that the dominant strengthening mechanism attributed to resistance to dislocation movement due to dislocation pile-up or increased dislocation density near the matrix-particle interface, similar to Hall-Petch [63]. Experimental validation of inverse square root relationship provided in the following equation gives evidence of dislocation pile-up as the dominant strengthening [63]. This model is adopted for particulate matrix composites. The composite yield strength equation for dispersion reinforced composite is

$$\sigma_c = \sigma_m + \kappa \lambda^{-\frac{1}{2}} \tag{18}$$

where σ_c and σ_m are composite and matrix yield strength, respectively. *k* is the material constant. The interparticle spacing, λ, depends on volume fraction *f* and particle size d_p [64];

$$\lambda = \left[\left(\frac{\pi}{6f} \right)^{\frac{1}{2}} - \frac{2}{\pi} \right] d_P \tag{19}$$

The material constant, κ, is given by:

$$\kappa = \beta \mu \left(b \varepsilon \right)^{\frac{1}{2}} \tag{20}$$

where β, μ, *b*, and ε are a constant, shear modulus of matrix alloy, Burgers vector, and strain, respectively. The κ value is typically correlated to experimental results by volume fraction and particle sizes.
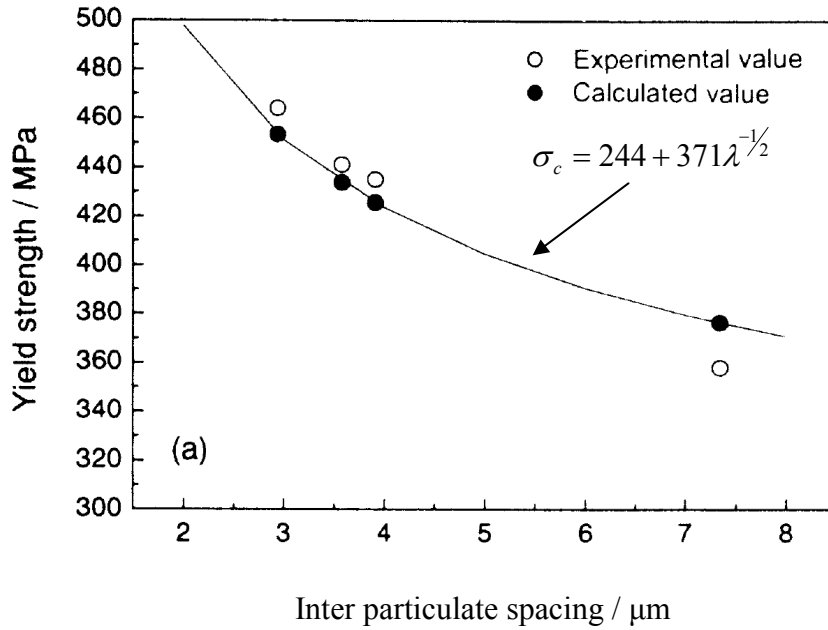
Figure 48: Composite yield strength as a function of inter particulate spacing, λ, varied by SiC volume fraction of 3.5 μm SiC particles [63]
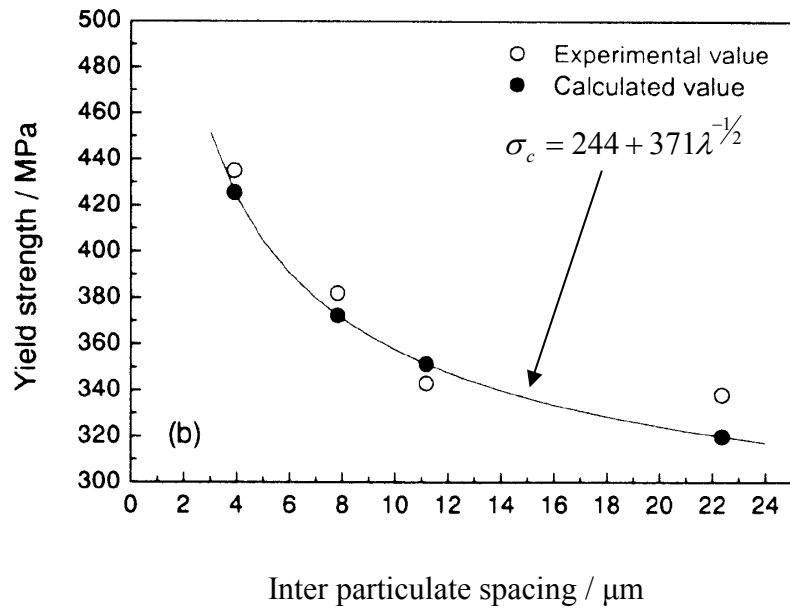
Figure 49 Composite yield strength as a function of inter particulate spacing varied by SiC particulate size at 0.17 volume fraction [63]

This model was fit to SiC/Al produced through conventional powder metallurgy procedures. Good agreement between calculated and experimentally obtained data is illustrated in Figure 48 and Figure 49 for both cases of varying of volume fraction and particle size.

4.3.4 Computational Approaches

4.3.4.1 Unit cell with rigid particles and perfectly plastic matrix

Since strengthening involves the interactions of stress and strain fields for particulates, often of different geometries, a more accurate approach involves computational analyses to determine the composite strength as a function of the particle and matrix attributes. Initial efforts by Bao et al. [65] represented uniformly distributed rigid reinforcement particles in a matrix through a unit cell approximation as seen in Figure 50. A particle is embedded in an axisymmetric cell to represent the composite microstructure. The matrix material is assumed to deform perfectly plastic; while, the perfectly rigid particles are treated as being perfectly bonded in the matrix. Finite element analysis is used to solve the boundary value problems for this axisymmetric cell analysis. The limit on volume fraction is 2/3 for spherical particles since theoretically they will start touching. Calculated values for β as a function of volume fraction and additional computational results are shown in Figure 52. Within the dilute limit, volume fraction less than 0.2, strength increases linearly with volume fraction and β is taken to be 0.375. This parameter is a means by which to relate the composite yield strength to a simple function:

$$\sigma_c = \sigma_m (1 + \beta f) \tag{21}$$

where f and β are volume fraction and reinforcement factor, respectively.
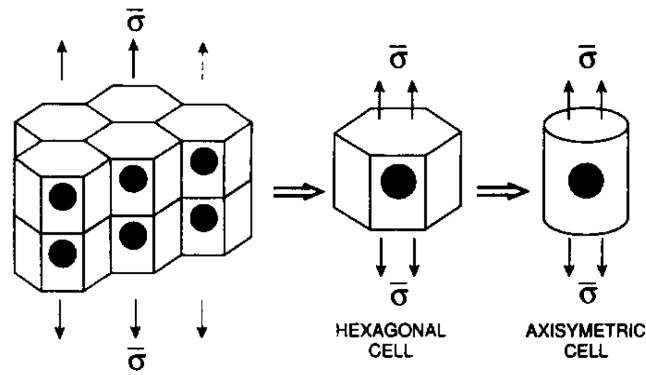
Figure 50: Unit Cell Approximation [65]
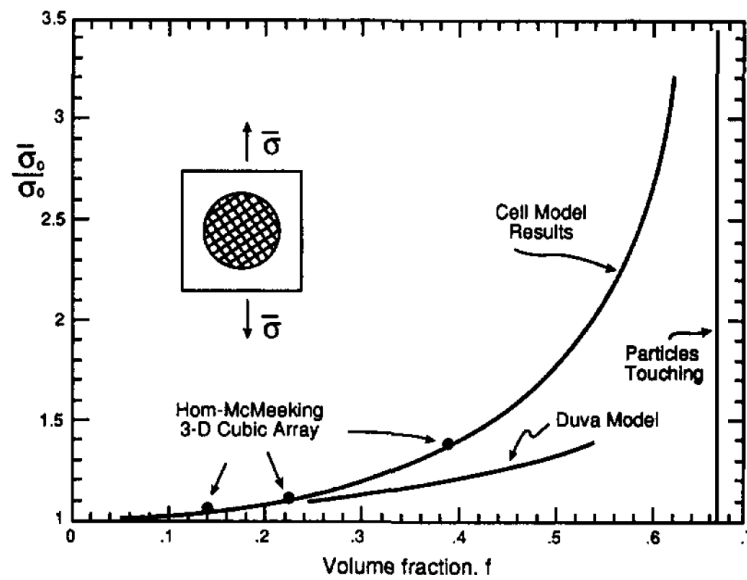
Figure 51: Limit flow stress as a function of volume fraction for an elastic-perfectly plastic matrix containing rigid spherical particles [65]
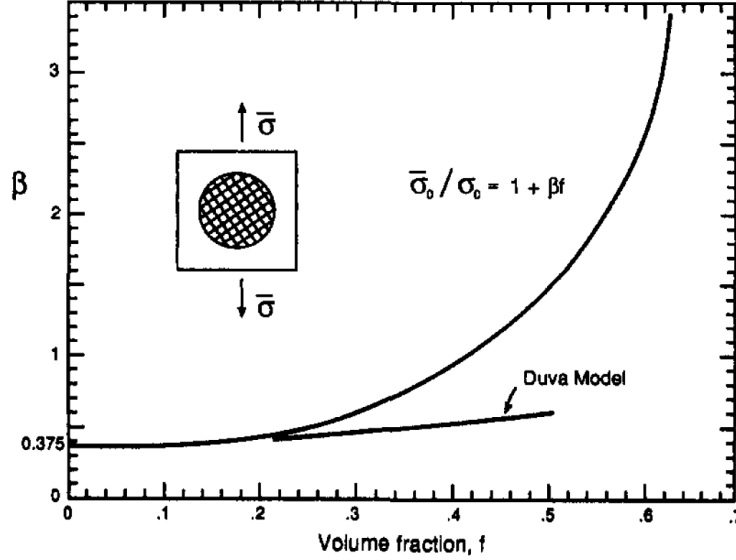
Figure 52: Reinforcement factor β as a function of volume fraction for an elastic-perfectly plastic matrix containing rigid spherical particles [65]

4.3.4.2 Unit cell with rigid particles and work hardening matrix

Building from the FE derived unit cell formulations presented by Bao et al.[65], the yield strength for composite materials with rigid particles is extended to capture matrix work hardening [66]. The material investigated by Majumdar and Pandey [66] was a SiC particulate reinforced 7071 aluminum matrix. The composite strengthening was correlated to the composite attributes, particle volume fraction *f* and work hardening exponent of the matrix, *n*.

$$\sigma_c = \sigma_m \xi \left((1+3.5n)(1+\beta * f) - 3.5n \right) \tag{22}$$

where σ_m is the yield strength of the matrix. β and ξ are correlation parameters. When plastic flow is severely constrained (e.g. needle and disc shaped reinforcements at high volume fractions *f*>.6), the value of *n* often needs to be increased to account for constraint effects. Typically, composites reinforced with moderate reinforcement concentrations of

75

spherical particles are adequately modeled by equating n for matrix material with that of the composite. The reinforcement factor, β, includes the reinforcement shape and volume fraction contributions to composite strengthening. The factor of 3.5 preceding the work hardening exponent varies according to particle morphology. This factor is typically bounded within the range of 2.5-3.5. These bounds are determined by power law strain analysis of work hardening behavior. Similar to β, this factor is obtained utilizing data presented in the work by Bao et al. [65] for various reinforcement shapes and configurations. σ_m is the approximate 0.2% offset yield strength of the matrix. The value of ξ is related to the level of plastic strain,

$$\xi = 1 - 0.07 \exp(-\varepsilon_P / \varepsilon_O) \tag{23}$$

where ε_P and ε_O are the plastic strain in the composite and yield strain of the matrix, respectively. For simplicity, the parameter ξ can be assumed to be unity for sufficiently large strains ($\varepsilon > 3\varepsilon_o$), at strains comparable to the yield strain, $\xi = 0.94$. For the purpose of strength estimations, 0.94 is typically appropriate.

4.4 Fracture Toughness

4.4.1 Empirical Correlation

Predictive models for fracture toughness are derived on fracture mechanisms and details of the microstructure (e.g. interparticle spacing, porosity, interfacial bonding strength, etc.). If the microstructure contains microcrack features and matrix is brittle, linear elasticity theory can be utilized as an estimate to determine fracture toughness. The crack field must be larger than the characteristic microstructure length to treat body

as homogenous. Young's modulus and fracture energy are related to fracture toughness by:

$$K_{IC} = \left(E G_c \right)^{1/2}$$ (24)

where E and G_c are Young's modulus and critical fracture energy release rate, respectively. Both K_{IC} and G_C have been shown experimentally to increase nearly linearly with reinforcement volume fraction in particulate reinforced composites [67]. The fracture toughness behavior of particulate reinforced composites has been observed to vary nearly linearly with reinforcement concentration [68], [69]

4.4.2 Path Dependent

Crack path dependent models have been derived, which attempt to capture the microstructure characteristics in the vicinity of the crack tip. Rice and Johnson [70] attempted to characterize fracture toughness based on the strain ahead of the crack tip. Based on their model, fracture occurs when the applied stress is sufficient to produce a high strain region ahead of the crack tip large enough to encompass the nearest reinforcement particle. This condition for failure is based on the assumption that microcracks are associated with every particle due to debonding at the matrix-reinforcement interface.

The failure mechanism presented by Rice and Johnson [70] was related to composite properties and microstructure parameters by Hahn and Rosenfield [71]. A relationship between critical crack opening, δ, and reinforcement spacing, λ_v (i.e. microcrack spacing) of $\delta = 0.5\lambda_v$ is assumed. Through the relation of critical crack opening and critical crack energy, fracture toughness can be expressed in terms of

reinforcement volume fraction. The resulting fracture toughness of the composite, K_c, is given by

$$K_c = \left[2\sigma_Y E \left(\frac{\pi}{6} \right)^{1/3} d \right]^{1/2} f^{-1/6}$$

(25)

where σ_Y, E, d, f are matrix yield strength, matrix Young's modulus, spherical particle diameter, and volume fraction, respectively [71].

Significant limitations are encountered in this approach due to the assumptions of particle concentration in crack tip vicinity. If microcracks are not present at each particle; specifically, the particles are well bonded to the matrix, then the K_c predicted by this model is a lower bound. The relevance of this model diminishes as volume fractions are reduced. The monotonically increasing relationship between yield strength and fracture toughness exhibited by this model is inconsistent with experimental observations which often reveal an inverse trend. Fracture toughness values predicted by this model are typically of the correct order of magnitude, but usually over estimated [71].

4.5 Wear Behavior

Despite vast experimental wear studies, accurate and widely applicable predictive tribological models for particulate reinforced composites are scarce due to the complexity of the wear mechanisms [72]. Most wear models for composite materials are not explicitly dependent on the critical microstructure features. An inverse rule of mixtures (IROM) is derived if both constituents of the composite wear at the same rate [73],

$$\frac{1}{W_c} = \frac{f_1}{W_1} + \frac{f_2}{W_2}$$

(26)

where W is the wear rate.

A linear rule of mixtures (ROM) of wear rates has been proposed [74]. The predicted wear behavior of the composite is derived from proportional wear rate contributions of each constituent,

$$W_C = f_1 W_1 + f_2 W_2 \qquad (27)$$

The IROM and ROM have been generally accepted as lower and upper bounds, respectively, for wear rate predictions when the interfacial bond between the constituents is strong. However, however the wear rate will exceed the upper boundary specified by the linear ROM, as shown in Figure 53, when the interfacial strength between the constituents is not strong or there are auxiliary wear interactions between the constituents.
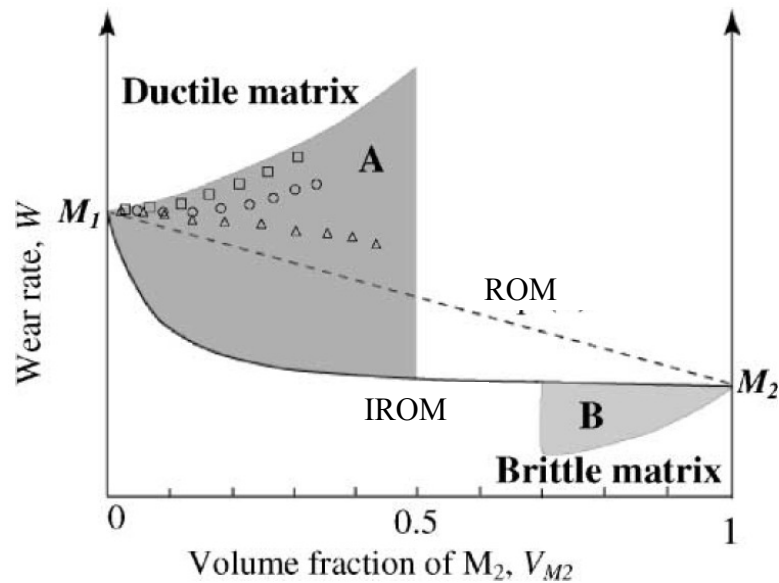
Figure 53: Experimental wear rate data points compared with upper (linear ROM) & lower (inverse ROM) [76]

A modification to the inverse ROM wear equation was introduced by Lee et al. [75] to more accurately capture the various contributions to wear in composite materials:

79

$$\frac{1}{W_C} = \frac{f_1}{W_1} + C\frac{f_2}{W_2}$$

(28)

where C is the contribution coefficient which depends on the interfacial strength and reinforcement particle size. For weak interfacial strengths, C tends to zero. The different wear rate projections for strong and weak interfacial bonds are illustrated in Figure 54.
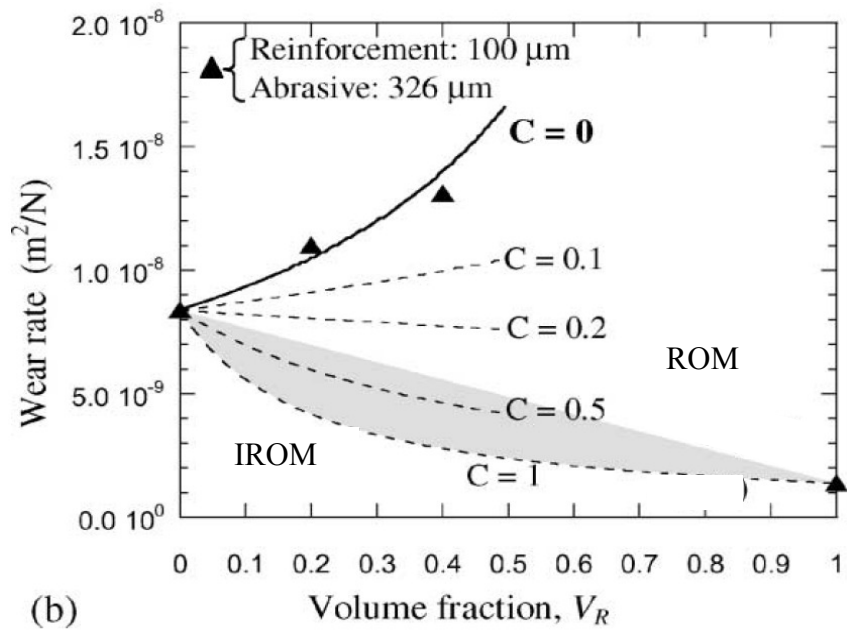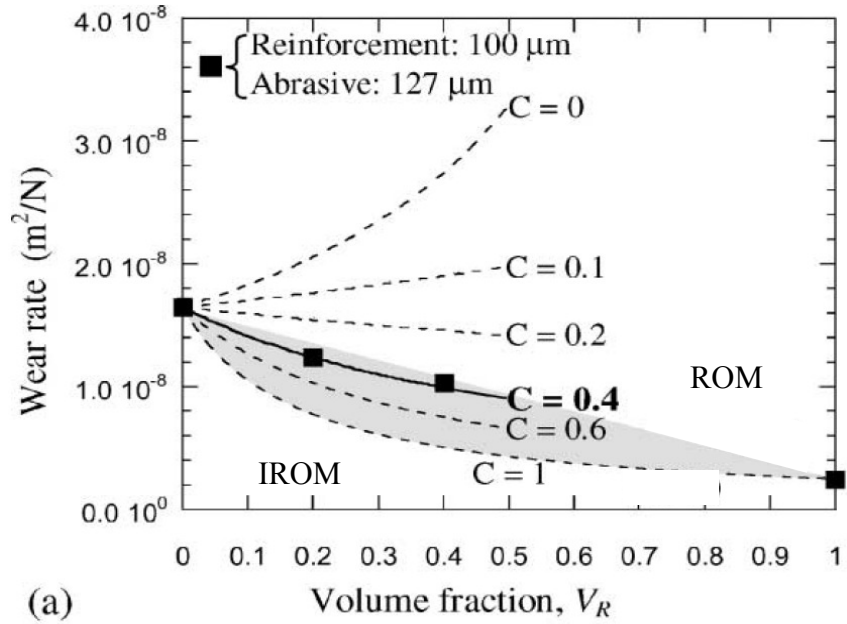
Figure 54: Comparison of predicated and experimentally obtained wear rates for strong (a) and weak (b) reinforcement/matrix bonding interfaces for reinforcement volume fractions from 0 to 1[75]

4.6 Electrical Resistivity

The transport and diffusion properties (e.g. electrical resistivity) are predominantly governed by the establishment of "connectivity paths." These paths are created as the conductive particles form a connective path throughout the material from one surface to another. These conductive paths provide a conduit for free electron migration. Any resistive microstructure component (e.g. porosity, secondary phase constituents, interface degradations, etc.) included in or inhibiting these "connective paths" must be accounted for to accurately determine electrical resistivity. The formation of this connective path is influenced by microstructure parameters such as constituent volume fraction, size, shape, processing parameters, solute atoms in matrix, and dislocation density [77]. Electrical conductivity is the reciprocal of electrical resistivity. This relationship is defined by

$$\rho = \frac{1}{S} \tag{29}$$

where ρ and S are electrical resistivity and electrical conductivity, respectively.

4.6.1 Percolation Theory

Volume fraction of conducting composite constituents is a critical determinant of conductivity properties in composite materials, particularly in conductive-insulator microstructures containing a mixture of conductive and insulator constituents. Percolation thresholds, minimum volume fraction of conductive constituent to ensure one fully connected path, have been estimated for various conductive component arrangements. Typically, random distributions yield percolation thresholds in the range of 0.19 to 0.22 for spherical particle geometries. Smaller conductive spherical particles

require higher volume fractions to yield the same composite conductivity produced by larger diameter spherical particles. Volume fractions exceeding the percolation threshold result in the formation of additional conductive paths. Above the percolation threshold, composite conductivity can be described by the rule of mixtures, assuming uniform microstructures with preferred reinforcement orientations [77]. The conductivity for composite materials is given by,

$$S_c = S_1 f_1 + S_2 f_2 \tag{30}$$

.

The conductive constituent morphology, for example, characterized by the aspect ratio, affects the percolation threshold. Conductive morphologies that yield increased opportunity for conductor-conductor contact reduce the minimum volume fraction required. This behavior is described by:

$$P_{AR} = \frac{P_C}{\beta^{1/2}} \tag{31}$$

where P_{AR} is the percolation threshold as a function of particle aspect ratio, β. P_C is the percolation threshold, based on spherical particles

$$\beta = L/d \tag{32}$$

where L and d are the reinforcement length and diameter, respectively.

The following are necessary microstructure attributes for determination of electrical conductivity properties: (i) electrical conductivities of each constituent, (ii) volume fractions and distributions of constituents, (iii) size, shape, orientation and

spacing of the constituents, (iv) interaction between constituents, (v) preparation method [83].

4.6.2 General Effective Medium

This approximation models 3D composite microstructures by representing a particle as a sphere embedded in a surrounding medium, which represents the matrix constituent [78]. A uniform microstructure is assumed; therefore, the spherical particle in the surrounding medium "effectively" represents the entire microstructure. Limitations in this model are introduced by the inability of this model to capture the changes in the effective medium. One critical example of this is observed as the volume fraction reaches concentration levels that cause variations between effective mediums. The spherical reinforcement is assumed to be perfectly bonded to surrounding effective medium. There are no allocations for resistive microstructure attributes.

The general effective medium (GEM) equation is based on mean-field theory, percolation theory, and network formation [78]. In this model, it is assumed that the entire microstructure is modeled by the representative volume, effective medium. This model has been shown to accurately model the conductivity of composite materials over a wide volume fraction range [79]. Initial development of the general effective medium model is founded on the work by Landauer [80] and Bruggeman [81]. Analysis of the non-linear dependence of the composite conductivity on the conductive volume fraction was pioneered through the effective medium theory. This relationship is described by:

$$f_1 \frac{S_1 - S_c}{S_1 + 2 \cdot S_c} + f_2 \frac{S_2 - S_c}{S_2 + 2 \cdot S_c} = 0 \qquad (33)$$

Directly relevant to the presented discussion concerning percolation threshold is the non-linear transition from the conductivity level of one constituent to the other as the volume fraction approaches this critical concentration. Composite conductivity, as specified by percolation theory, is related to the conductive constituent volume fraction and conductivity by:

$$S_c = 0 \text{ for } f_2 < f_{pt} \tag{34}$$

$$S_c = S_2 \cdot \left(\frac{f_2 - f_c}{1 - f_c} \right)^t \text{ for } f_2 \geq f_{pt} \tag{35}$$

where f_{pt} is the percolation threshold and t is the critical exponent for the composite. The critical exponent is predicted to have a value ranging from 1.4 to 2.46 [82]. The utility of this percolation based model is limited to composite systems in which the conductivity of one constituent approaches zero. The contribution of the percolation theory into GEM development permits for the incorporation of microstructure transitions due to conductive reinforcement levels.

Conductivity as a function of volume fraction and conductivity of each constituent material is described by the GEM equation,

$$f_1 \cdot \frac{S_1^{1/t} - S_c^{1/t}}{S_1^{1/t} + f_c/(1 - f_c) \cdot S_c^{1/t}} + (1 - f_1) \cdot \frac{S_2^{1/t} - S_c^{1/t}}{S_2^{1/t} + f_c/(1 - f_c) \cdot S_c^{1/t}} = 0 \tag{36}$$

where f_1 is the volume fraction of the lower-conductivity constituent. f_c and t are the critical volume fraction of conducting constituent and the critical exponent of conductivity, respectively. S_1 and S_2 represent conductivities of the lower and higher conductive constituents, respectively. S_c is the effective conductivity for the composite.
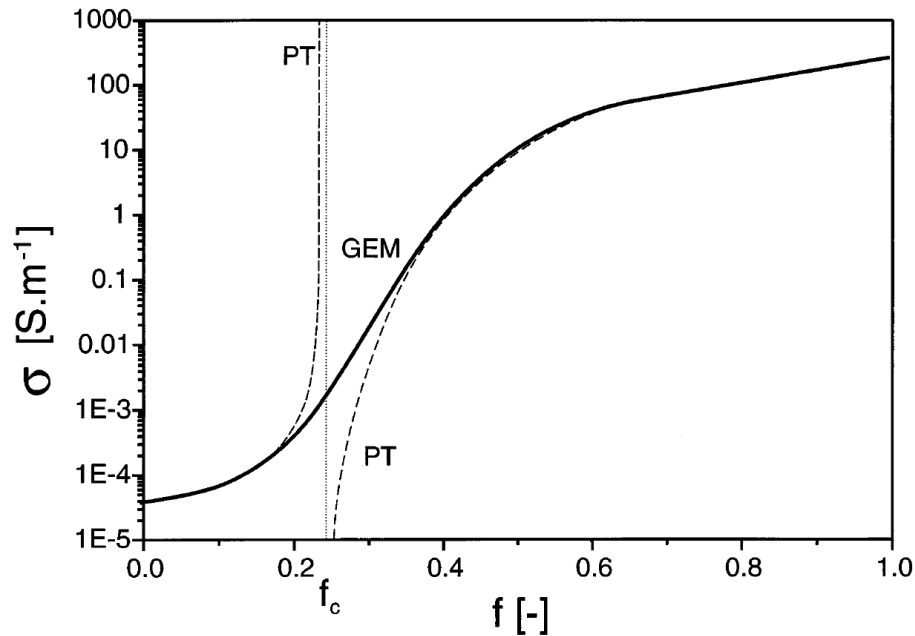
Figure 55: Example of S-shaped curve for the effective conductivity dependence on the volume fraction of conducting constituent [79]

The utility of this model over a large reinforcement range is demonstrated in Figure 55. Graphical validation of the conductive path being created at the critical volume fraction is confirmed by the non-linear increase in composite effective conductivity with increasing volume fraction of the conductive constituent above the percolation threshold. The dashed lines are produced using the percolation model. The coincidence of the GEM plot with those of the percolation model confirm that the critical exponent and percolation threshold parameters in the percolation models are indeed equivalent to the fitting parameters f_c and t in the GEM equation.

Percolation threshold values have been observed to range from less than 1% to 60%. Furthermore, there is not a generally accepted theory to predict this value based solely on microstructure observations for complex distributions (i.e. microstructures not simplified for theoretical modeling purposes. The percolation threshold, f_{pt}, and critical

component, t, are microstructure parameters that usually need to be experimentally determined.

4.6.3 Equivalent Circuit Decomposition

Through equivalent microstructure transformation, Fan et al. [84] showed complex multi-constituent composites can be evaluated using simple equivalent electrical circuit techniques of decomposed microstructures, as seen in Figure 56. The effective conductivity of the composite material can be determined by summing the individual resistances for elements I, II, and III as resistors in parallel shown in Figure 57.
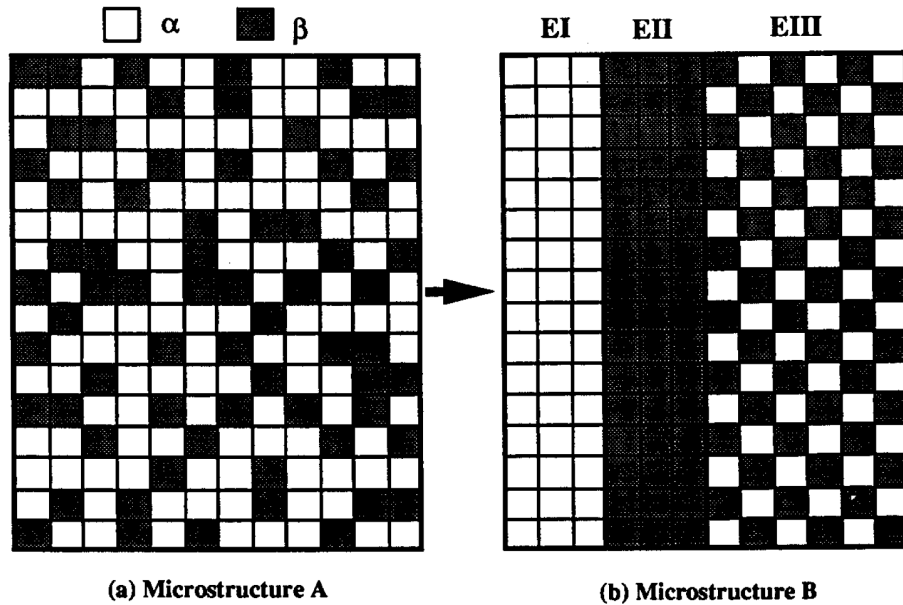
Figure 56: Schematic illustration of the topological transformation from microstructure A to microstructure B [84]
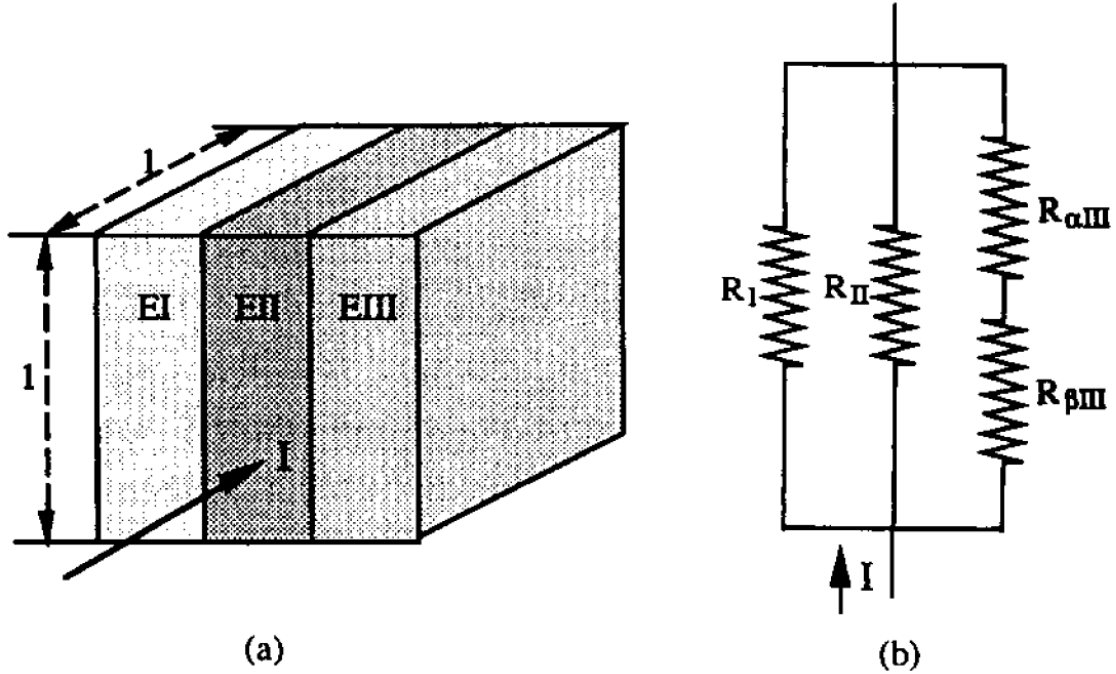
Figure 57: Schematic illustration a) the unit cubic three element body which is subject to an electrical current, b) equivalent electrical circuit of a) [84]

The composite conductivity is controlled by the inverse of the parallel resistance additions,

$$S_c = S_1 f_{1con} + S_2 f_{2con} + \frac{F_S}{\dfrac{f_{1III}}{S_1} + \dfrac{f_{2\beta III}}{S_2}} \qquad (37)$$

where S_c, S_1, and S_2 are the composite, component 1, component 2 conductivities, respectively. f_{1con} and f_{2con} are the contiguous volume fractions for each component in element I and II, respectively. F_s is the volume fraction of separation or the volume of element III. Physically, this microstructural parameter is the volume of the microstructure that is characterized by mixture of the 1 and 2 constituents. f_{1III} and f_{2III} are the volume fraction of component 1 and 2 in the discontinuous element III resulting from the equivalent circuit decomposition. For precise determination of electrical

88

conductivity properties, the microstructure parameters would need to be experimentally

obtained. Good agreement is achieved through the use of approximations. A power law

relationship is utilized to relate the contiguous volume fraction to the total volume

fraction of each constituent. The exponent values m and n range between 2 and 4. These

values are correlated by experimental observations [85].

$$f_{1con} = f_1^m \tag{38}$$

$$f_{2con} = f_2^n \tag{39}$$

$$F_s = 1 - f_{1con} - f_{2con} = 1 - f_1^m - f_2^n \tag{40}$$

The conductivity property estimation model presented by equation 37 [84] shows

good agreement with experimentally obtained electrical resistivity values for Cu based

materials as shown in Figure 58. Appreciable correlation is attained for the entire range

of volume fractions as well as constituent resistivity ratios of particle to matrix 2, 3, and

9. Increasing contiguity in the more conductive constituent is more efficient for

increased conductivity as compared to increasing separation of the more resistive

constituents. This separation of the more resistive particles permits the flow of the

electrical current while the discontinuous particles act as isolated resistive clusters in the

conductive matrix [84].
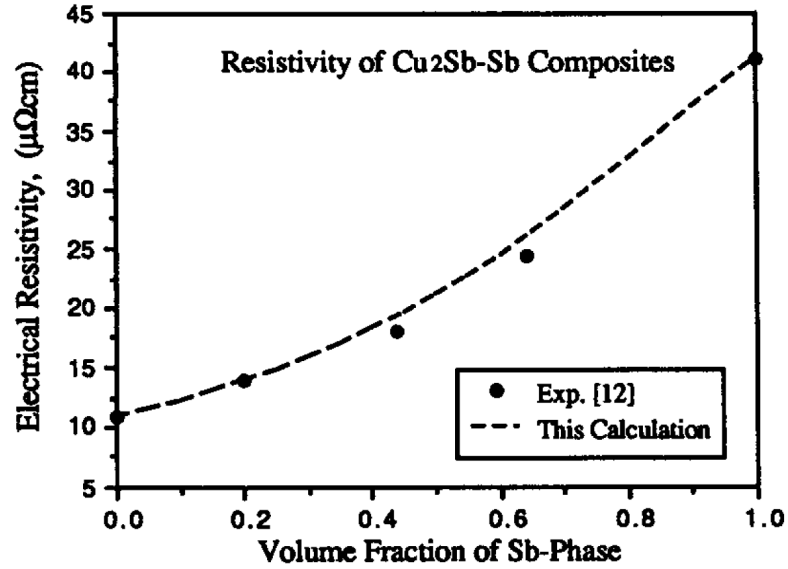
Figure 58: Calculated electrical resistivity of Cu$_2$Sb-Sb composites compared with experimental data [84]

4.6.4 Unit Cell Approximation

Chang et al. [86] investigated the influence of constituent coefficient of thermal expansion, particle size, volume fraction, and shape on MMC electrical conductivity of discrete reinforced MMC. Comparisons of experimental and theoretical composite resistivity values validate the influence of these microstructural parameters. The manifestation of residual stresses and dislocation concentrations is shown to be a crucial consideration in an effort to accurately predict the effective composite electrical conductivity.

A theoretical resistivity is derived based on the assumption that a unit cell, shown in Figure 59, represents the entire microstructure of the composite (i.e. the reinforcement is uniformly distributed throughout the microstructure). The spherical particulate is encapsulated in the matrix material in the RVE.

90
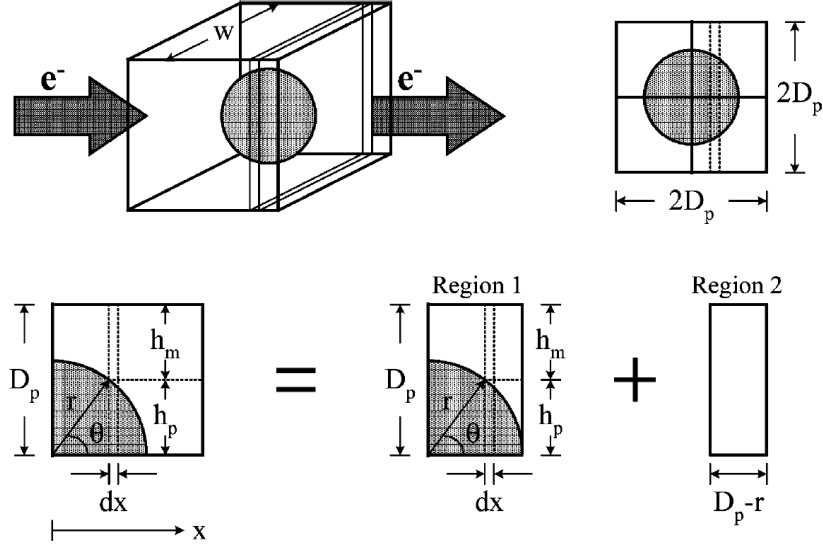
Figure 59: Unit cell containing spherical particle [86]

Further simplification is achieved by neglecting any interfacial material. Theoretical electrical resistivities are modeled with free electron migration as the only means of current flow. The RVE is separated in two regions as shown in Figure 59. The resistance in region 1 is calculated by adding the reinforcement and matrix resistance contributions. Region 2 is only comprised of the matrix material. The total resistance of the unit cell is modeled as the sum of region 1 and 2 resistances.

Integration of resistivity contributions of infinitesimally thin slices result in the theoretical resistivity of particulate reinforced composites as follows [86],

$$\rho_c(p) = \rho_m \left\{ 1 - \eta + \frac{4\rho_p}{\sqrt{\left[4\rho_p - (\rho_p - \rho_m)\pi\eta^2\right]\left[(\rho_p - \rho_m)\pi\right]}} \tan^{-1}\left[\sqrt{\frac{(\rho_p - \rho_m)\pi\eta^2}{4\rho_p - (\rho_p - \rho_m)\pi\eta^2}}\right] \right\} \quad (41)$$

where ρ_m, ρ_p, and $\rho_c(p)$ are the matrix, particulate, and composite resistivity, respectively. η depends on reinforcement volume fraction, f;

$$\eta = \sqrt[3]{\frac{6f}{\pi}} \qquad\qquad (42)$$

This electrical resistivity equation yields composite resistivity values that agree with the trend of experimentally obtained values; however, there is an appreciable deviation from measured resistivity properties. Relationships derived by Arsenault and Shi [87], [88] relate dislocation density to particle volume fraction, size, and difference in coefficient of thermal expansion. High concentrations of residual stresses and dislocations act as barriers to current flow. This phenomenon is captured by the inclusion of the bracketed term in:

$$\tilde{\tilde{\rho}}_c(p) = \rho_c(p)\left[1 + \left(\frac{\alpha^3 - 1}{\alpha^2}\right)f\right] \qquad\qquad (43)$$

where α is a constant that is a function dislocation density, type of matrix, type, size, and shape of the reinforcement, usually determined experimentally. This expression accounts for the region around the reinforcement particle where increased dislocation density and residual stresses are present; both of which are barriers to electron flow. Trends of increasing electrical resistivity with increasing particle volume fraction are shown in Figure 60. Influences due to variations in particle morphology are illustrated as well. Good correlation is shown between the experimentally obtained values and theoretically generated curves by utilizing the appropriate α value [86]. Demonstrations of accurate calculation of composite resistivity properties are limited to a volume fraction 0.4 in this work. Limitations encumbered due to the unit cell approximations prohibit accurate predications of volume fractions higher than where the assumption of uniform distribution (e.g. reinforcement-reinforcement contact) is no longer valid.

92
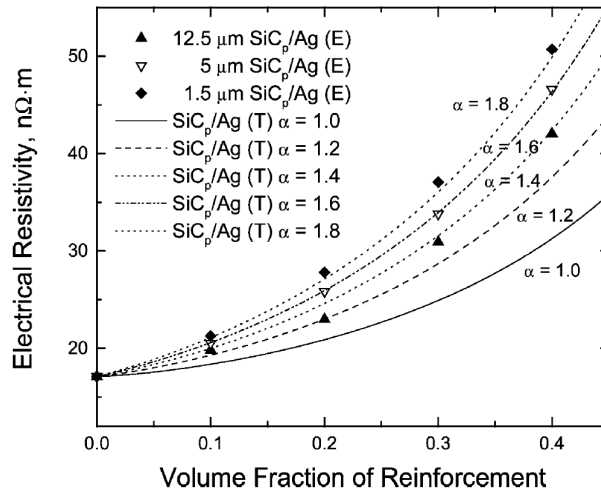
Figure 60: **Electrical resistivity of SiC particulate reinforced Ag composite as a function of volume fraction [86]**

Chapter 5: Experimental Procedures

A couple of these potential candidate materials were obtained and evaluated. These included copper-tungsten W-Cu, "self-lubricating" graphite-impregnated Cu, and Gr-W-Cu composites with different volume fractions of the constituents. The structure-property relations were determined through mechanical and electrical resistivity testing. This chapter describes the experimental procedures used to determine these properties. A unique test protocol for exposing mechanical test specimens to extreme current densities up to 1.2 GA/m^2 was developed.

5.1 Materials

The materials investigated are shown in Table 5. The Gr-Cu materials were developed by NSWCCD based on the premise of developing a "self-lubricating: material. The W-Cu materials are motivated by the material selection component of this study.

Table 5: Material designation and corresponding volume and weight % compositions

Designation	Composition vol.%	Composition wt.%	Source
C10100	99.99Cu	99.99Cu	McMaster Carr
C11000 H4	C11000 H04 99.9Cu-0.04O-0.005Pb		McMaster Carr
Annealed W	99.9W	99.9W	REMBAR
10W-90Cu	10.4W-89.6Cu	20W-80Cu	NAECO
32W-68Cu	31.7W-68.3Cu	50W-50Cu	NAECO
65W-35Cu	64.9W-35.1Cu	80W-20Cu	NAECO
15Gr-85Cu	15Gr-85Cu	4.3Gr-95.7Cu	NSWCCD
15Gr-20W-65Cu	15Gr-20W-65Cu	3.3Gr-38.6W-58.1Cu	NSWCCD

The W-Cu materials were produced by powder metallurgy methods. The W and Cu particle sizes are nominally 6 and 20 μm, respectively. The cylindrical billets had an average diameter and length of 15.9 mm and 50.8 mm, respectively. Thirty billets of each material composition were requested. NAECO was able to only yield twenty-three of the 10W-90Cu, the others were successfully manufactured. Specifics concerning the powder metallurgy processing parameters utilized by NAECO in the production are limited for proprietary reasons.

The materials from the Naval Surface Warfare Center Carderock Division (NSWCCD) were produced by vacuum hot press by Mr. D. Divecha. Cylindrical billets received nominally had a 34 mm diameter and are 57 mm long. Ten billets of each material manufactured received. The billet processing parameters are presented in Table 6.

The graphite morphology in the billets from NSWCCD is Mo coated flakes with in-plane dimensions of 200-400 μm and 5-50 μm thick. The W and Cu powders were blended by ball milling. They were consolidated through vacuum hot pressing in the axial direction. Approximately 90% of the Cu powder size is -325 mesh with balance -140 mesh. The copper powder is 99% pure with an apparent density of 2.39 g/cc.

Table 6: Billet Processing Parameters

Vacuum Hot Pressing Parameters	
Pressure	2000 psi
Hold Temperature	608 °C
Vacuum	2×10^{-4} - 5×10^{-5} torr
Hold Time	6 hrs.

The C101, C110 H4 (fully hardened), and pure annealed tungsten were received in a rod with a 15.9mm diameter and 0.6m length.

5.2 Microhardness Testing

The Vickers hardness was determined through the use of a Buehler 1600-6125 hardness tester located in Dr. Singh's laboratory in the School of Material Science and Engineering at the Georgia Institute of Technology. A 300 gram load was applied. Dimensional measurements of each rectangular shaped indentation were completed using a microscope function on the same apparatus. At least six indentations were taken approximately 2 mm apart. Care was taken to avoid indentation sites that were agglomerations of either constituent. The microhardness property for each material was determined by averaging the microhardness value determined by each indentation. This value correlates to Vickers hardness for the given load which was recorded for each material.

5.3 Tensile Testing

The mechanical properties of Young's modulus, yield strength, and ultimate yield strength were obtained through room temperature tensile tests. Stroke-controlled tests were used for the NAECO materials, while strain-controlled tests were utilized for the NSWCCD materials. These different testing procedures were required due to specimen size limitations arising from NAECO production procedures. All tensile specimens were machined in the mechanical engineering undergraduate machine shop at the Georgia Institute of Technology.

An image of the W-Cu specimens is shown in Figure 61. These specimens were fabricated according to ASTM E8 specifications. The dimensions of the specimens are as follows: overall length 54.1mm, gage length 13mm, and gage diameter 7.6mm. The annealed W and C110 H4 specimens were machined according to the same dimensions. Dimensions of the Gr-Cu and Gr-W-Cu tensile specimens are shown in Figure 62. The C101 specimens were machined according to the same dimensions. For the Gr-Cu and Gr-W-Cu specimens, strain was measured using a 0.5" gage length MTS 632 13B-20 clip on extensometer displayed in Figure 63.

For the W-Cu specimens, strain was measured using strain gages. Vishay Micro-Measurements SR-4 C2A-06-125LW-350 strain gages were utilized to accommodate for the reduced gage section length of the Cu-W specimens. The gages were attached to the tensile specimens according to the procedures specified by Vishay for copper based specimens. An illustration and dimensions of the strain gages are provided in Figure 64. A MicroMeasurements 2310A signal conditioner amplifier was used to obtain strain signal and input into the TestStar IIs control and data acquisition system.

A 20 kip Satec Uniframe uniaxial servohydraulic mechanical test system was used to execute the tensile tests. Tensile specimens were gripped within MTS 647 hydraulic wedge grips with MTS 647.10 wedge set assembly inserts. MTS TestStar IIs software was used for testing controls and data acquisition. The strain rate for the test was 10^{-4} strain per second. For the W-Cu specimens, stroke-controlled tests were conducted at a sufficiently low stroke rate to ensure strain rates of 10^{-4} strain per second. Axial force, crosshead displacement, strain, and time outputs were recorded for each test at a sampling rate of 0.1 seconds. For the Gr-Cu specimens, axial force, crosshead

displacement, strain, and time outputs were recorded at every change in strain value greater than or equal to 0.0005.

Specimens were first inserted into the grips with the load frame in load control. To avoid any unintentional loading, the load control was set to maintain zero axial force during specimen insertion. The clip strain gage was then attached in the gage section of the specimen. The strain value was inspected to ensure that zero strain was the equilibrium strain prior to any load being applied. Following insertion of the W-Cu specimens, the strain gage output was then balanced and calibrated to zero. The specimen was then inserted into the top grip. Strain gage output was then inspected again to ensure stable values. Crosshead displacement values were used to calculate strain greater than the 50,000 microstrain limit of the strain gage. Increasing displacement was applied until the specimen fractured (i.e. applied load returned to zero). Each piece of the specimen was carefully removed and stored for subsequent examinations.
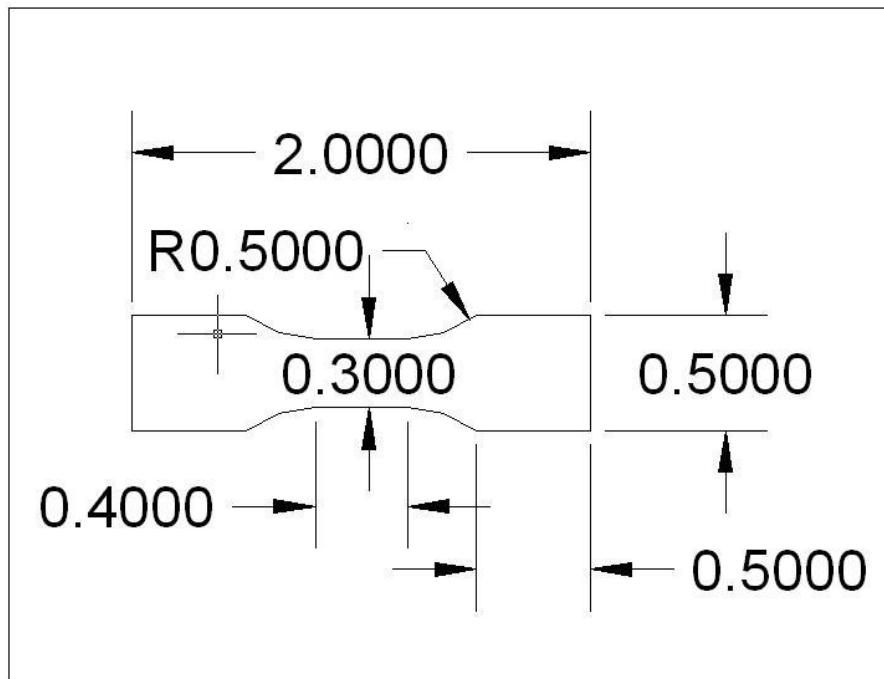
Figure 61: Tensile specimen used for materials obtained from NAECO
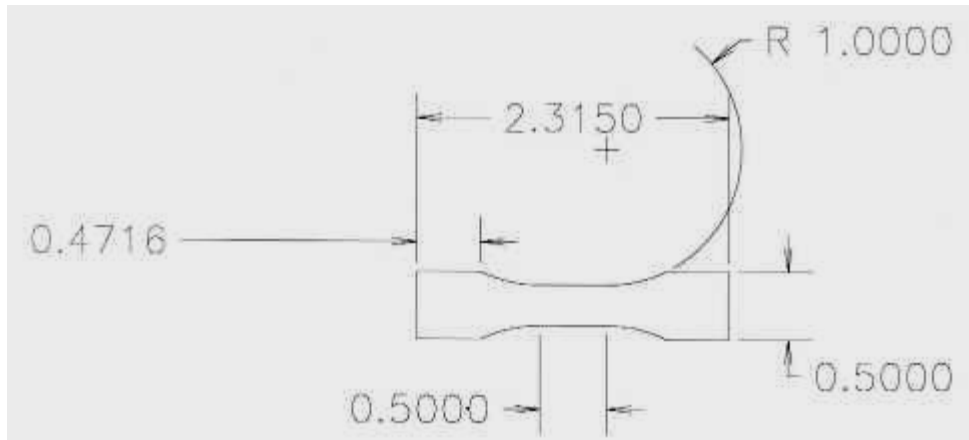
Figure 62: Tensile specimen used for materials obtained from NSWCCD, REMBAR, McMaster-Carr
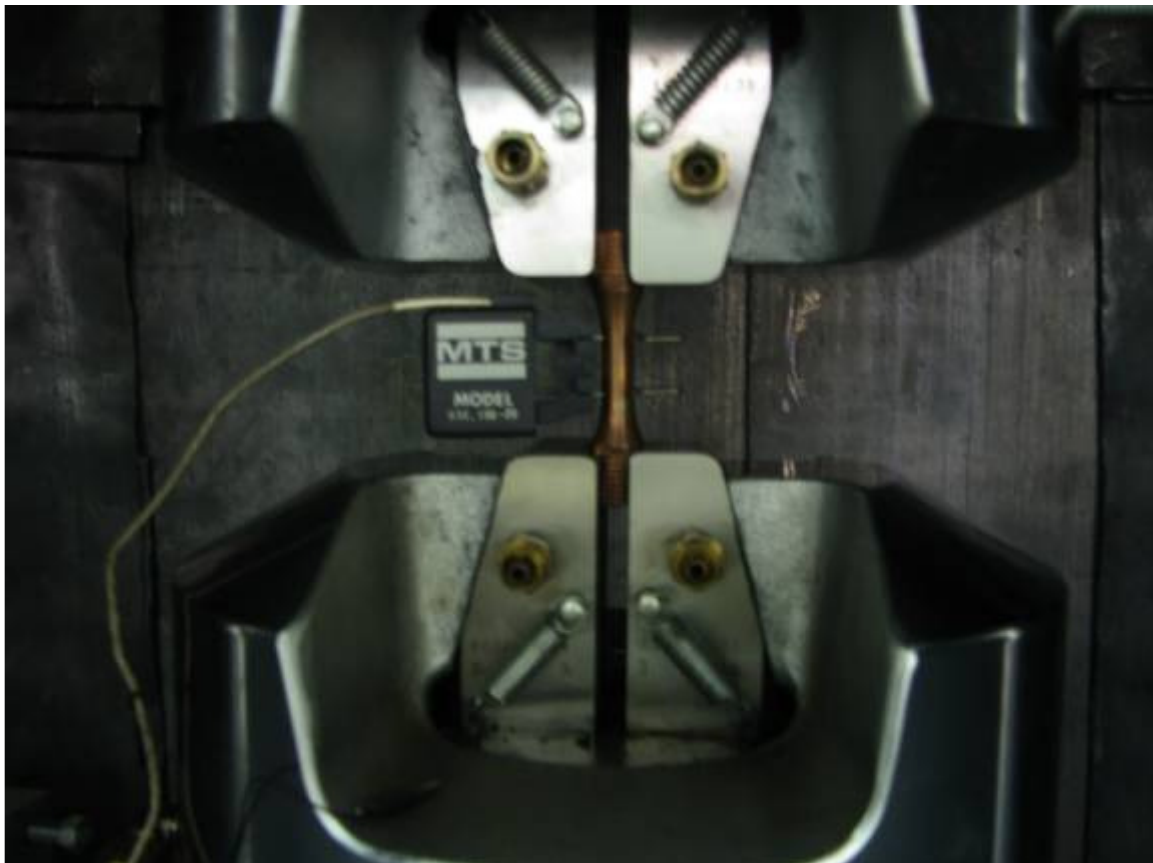
Figure 63: Hydraulic Grip and Extensometer Configuration
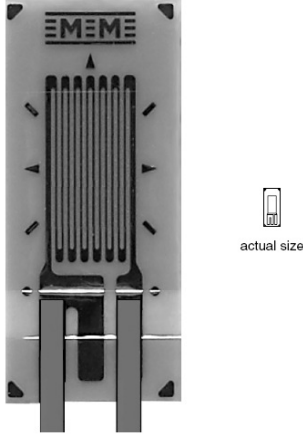
GAGE PATTERN DATA

	GAGE DESIGNATION See Note 1	RESISTANCE (OHMS)	OPTIONS AVAILABLE
	L2A-XX-125LW-120	120 ± 0.6%	
	L2A-XX-125LW-350	350 ± 0.6%	
	C2A-XX-125LW-120	120 ± 0.6%	
	C2A-XX-125LW-350	350 ± 0.6%	

DESCRIPTION

Widely used general-purpose gage.

RoHS COMPLIANT

GAGE DIMENSIONS		Legend:	ES = Each Section S = Section (S1 = Sec 1)		CP = Complete Pattern M = Matrix	inch millimeter

Gage Length	Overall Length	Grid Width	Overall Width	Matrix Length	Matrix Width
0.125	0.238	0.070	0.080	0.315	0.170
3.18	6.05	1.78	2.03	8.00	4.32

Figure 64: Vishay strain gage dimensions

5.4 Pulsed High Density Electrical Current Test

The high density electrical exposure tests were conducted on the IAP Research lab-scale EML system located in the Extreme Tribology Laboratory at the Georgia Institute of Technology. It was utilized to expose specimens to pulsed current densities on the order of 1.2 Ga/m^2 corresponding to approximately 55,000 amps, based on a gage diameter of 7.6mm. Three pulsed power supply modules were charged to 1KV and dumped simultaneously in order to generate the desired current level of 55,000 amps. A fixture was designed to be inserted in the breech end of the railgun in place of the rails, as shown in Figure 65. The tensile specimens are bolted into the railgun breech block as a means of producing a short circuit as shown in Figure 65. In this method, all of the current released from the capacitor bank flows through the specimen. A schematic of this modification is illustrated in Figure 66. The rail insert machining detail dimensions are shown in Figure 67.

The voltage measurement across the specimen was collected by attaching cable leads to either end of the specimen gage section (i.e., 0.4in apart). The cables were attached by wrapping wire leads around the specimen at both ends of the gage section. These were then fixed in place with electrical adhesive insulation. Current and voltage plots were retrieved through the CAMZ data acquisition system configured by IAP Research, Inc. The data acquisition card was a National Instrument's PCI-6133 with a sampling rate of 3 million samples per second for each channel. Each specimen was subjected to three cyclic exposures. Approximately, two to three minutes elapsed between exposures for equipment, safety, and specimen inspections. Visual and optical microscopy inspection of each specimen was completed at the end of each test to determine any apparent effects of the electrical current exposure. A summary of the specimens exposed to the high density electrical current is shown in Table 7.

Table 7: Pulsed High Density Electrical Current Test Plan

Material	Number of Cyclic Exposures
10W-90Cu	3
32W-68Cu	3
65W-35Cu	3
C110 H4	3
Annealed W	3
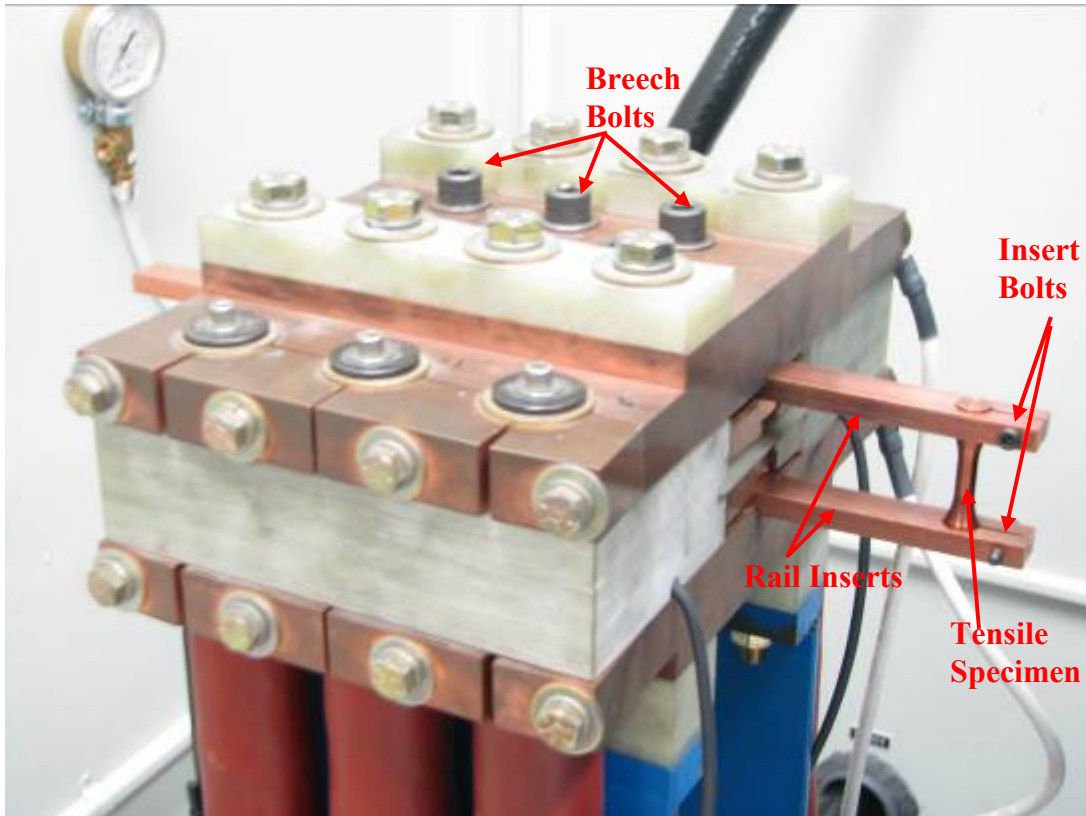
Figure 65: Railgun Breech fixture
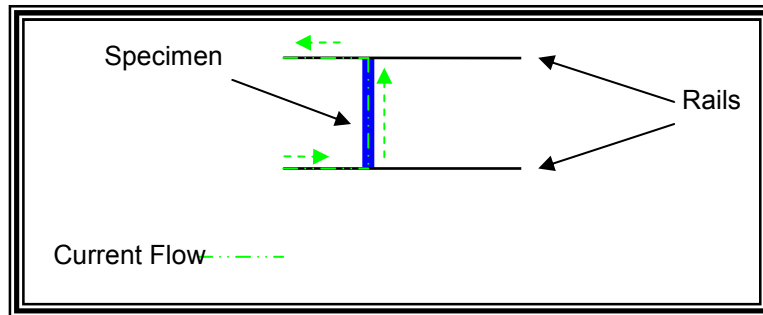
Figure 66: Schematic of Short Circuit Modification for High Current Density Exposure
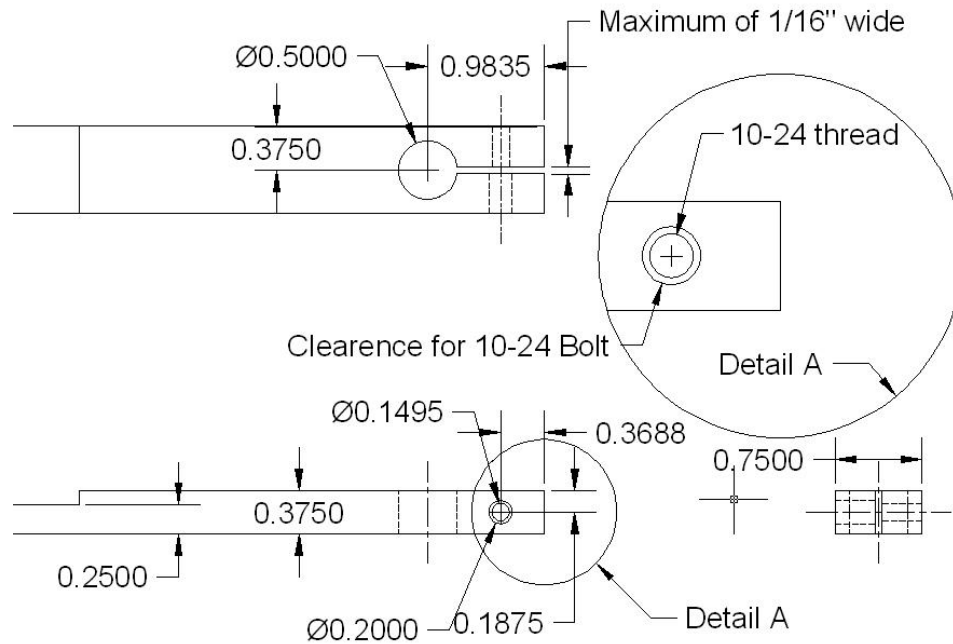
Figure 67: Dimensional Drawing of breech rail component

5.5 Microscopic Characterization

Optical and scanning electron microscopy methods were used to characterize microstructures of the as-received specimens and fracture surfaces. Surfaces were prepared for optical examination through the following procedure. A Buehler Isomet low speed diamond saw was used to section samples from the as-received specimens. These samples were initially cleaned by spraying them first with acetone, then ethanol, and finally rinsing them with distilled water. Specimens were then deposited into a beaker filled with a soap solution. This beaker was then inserted into an ultrasonic agitator for approximately 10 minutes. The acetone, ethanol, and distilled water rinse cleaning was then repeated. Struers EPOAR epoxy-hardener and EPOES resin were used to cold mount specimens for polishing. The mount was allowed to cure for at least 24 hours.

The polishing procedure for CuMC as specified by Struers on their website was used with slight modification. The steps are given in Table 8. A Struers RotoPol-15 automatic polisher with a RotoForce-1 was used.

Table 8: Specimen preparation for microscopic characterization

Description	Abrasive Substrate	Load (N)	Duration (min)	Rotation Speed (rpm)
Initial grinding	400 grit	15	3	200
Sec. grinding	800 grit	5	3	200
Polishing	1000-4000 grit	5	3	150
Polishing	3 μm diamond suspension	5	3	150

Images of the microstructures were taken by an Olympus BX40 optical microscope. Images were produced and edited by PictureFrame imaging software. An ISI Dual Stage 130 SEM was used to examine polished as-received surfaces as well as fracture surfaces. Back-scatter capabilities were provided by an ETP SEMRA Robinson detector. The back-scatter images more clearly differentiate the constituent materials.

Chapter 6: Results and Discussion

6.1 Microstructure

The as-received microstructures of the 10W-90Cu composites are shown in Figure 68 and Figure 69. In these images W is grey in optical images and is the lighter material in the SEM images. Porosity is observed in the 10W-90Cu specimens as the dark circular regions. A zoomed image reveals the nature of porosity concentrations in close proximity to the W. Porosity is also observed in the Cu matrix, suggesting that the particles did not consolidate during processing of the 10W-90Cu.

100 μm

50 μm
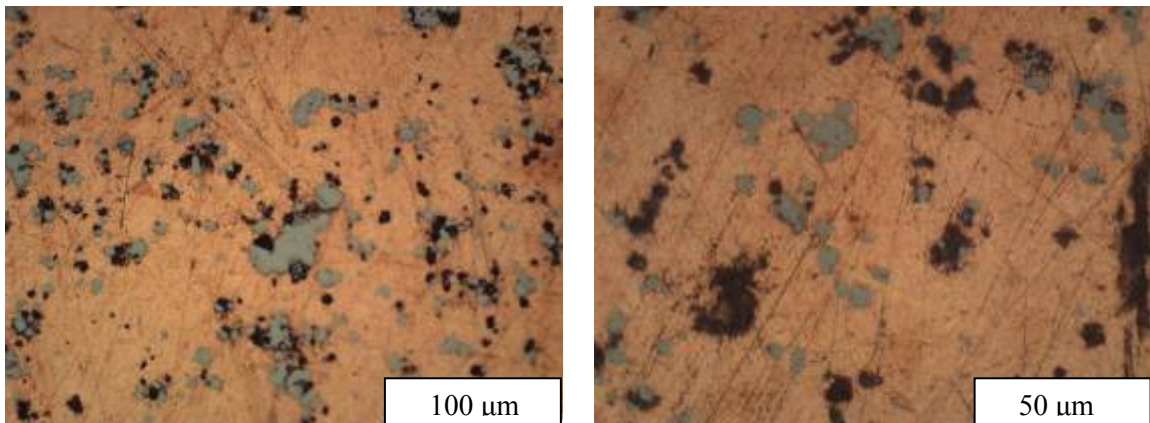
Figure 68: Optical microscopy image of as-received 10W-90Cu
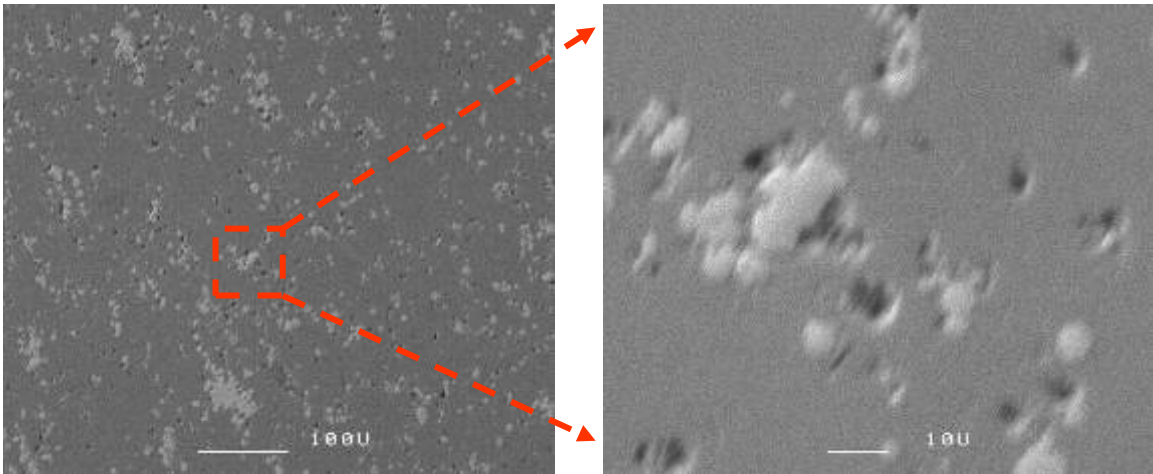
Figure 69: SEM image of as-received 10W-90Cu

The 32W-68Cu microstructure is shown in Figure 70 and Figure 71. The copper matrix is fully consolidated with negligible porosity. These images suggest appropriate processing parameters to achieve good mechanical properties. The microstructure images indicate desirable W-Cu interfacial regions, which appear to be well-bonded. The volume fraction of W appears to be in excess of 32%. This is attributed to the smearing away of the much softer Cu constituent [89].
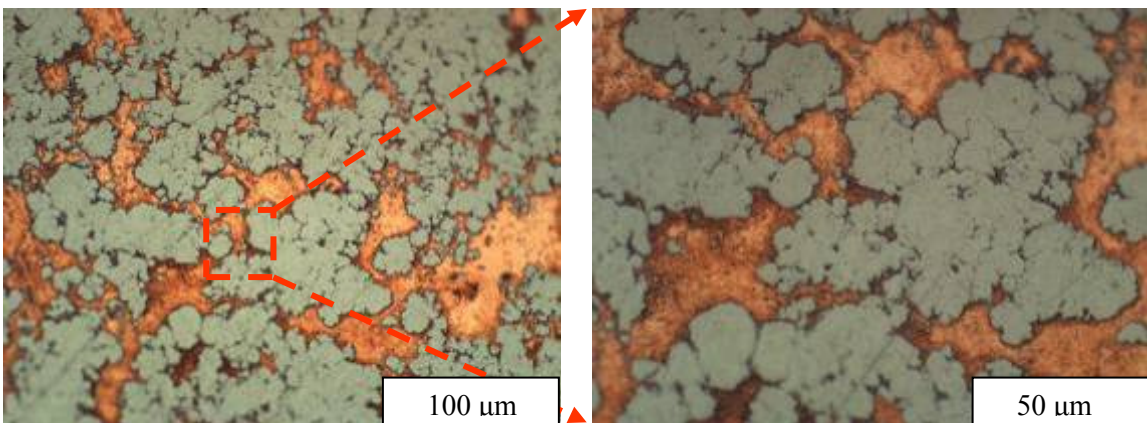
Figure 70: Optical microscopy image of as-received 32W-68Cu
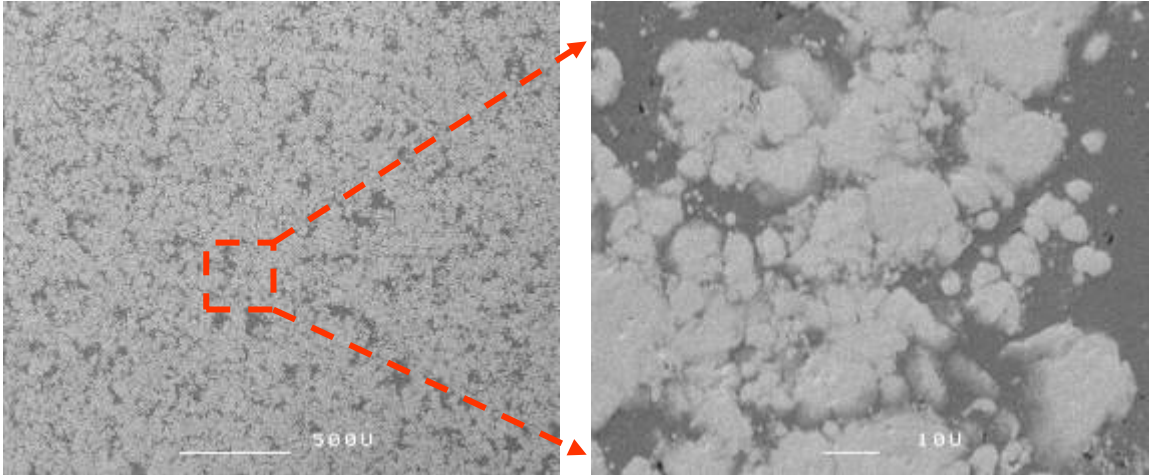
Figure 71: SEM image of as-received 32W-68Cu

The microstructure of the 65W-35Cu is shown in Figure 72 and Figure 73. The presence of limited Cu connectivity is presented in these figures. The connectivity of tungsten is complete. Similar to the 32W-68Cu, a significant amount of the Cu material is removed during polishing. For all of the preceding W-Cu composites, post-processing chemical analysis was conducted to ensure volume concentrations specifications were accurate [89].
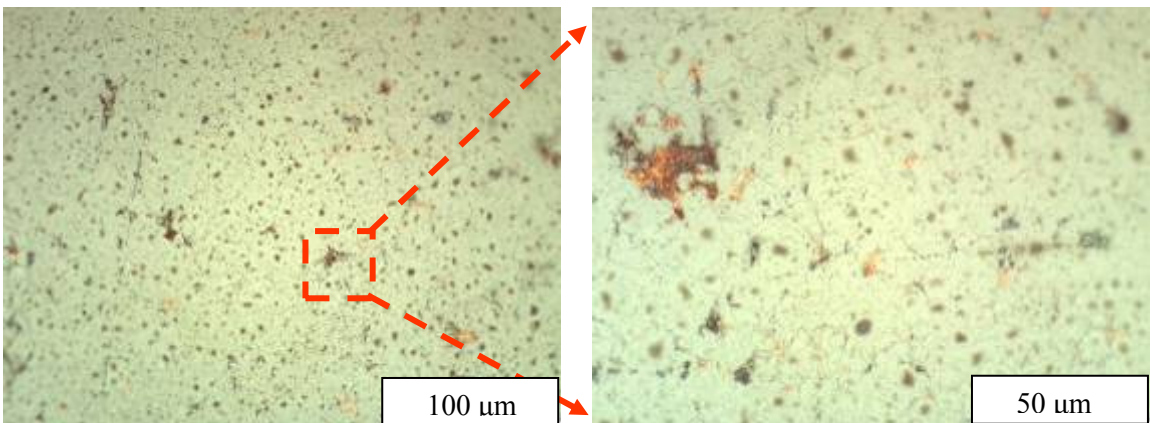
Figure 72: Optical microscopy image of as-received 65W-35Cu
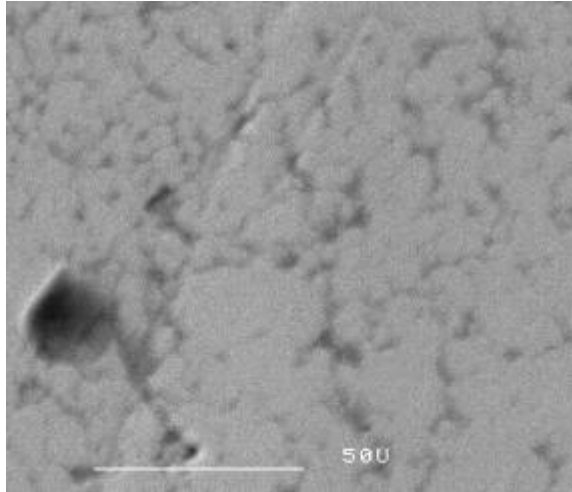
Figure 73: SEM image of as-received 65W-35Cu

The microstructure of the graphite containing composite is shown in Figure 74. Visualization of the graphite flake morphology illustrates how the graphite flakes are essentially cracks in the microstructure. In this figure, the consolidation pressure is applied in the horizontal direction, thus yielding the vertical flake orientation in the microstructure.
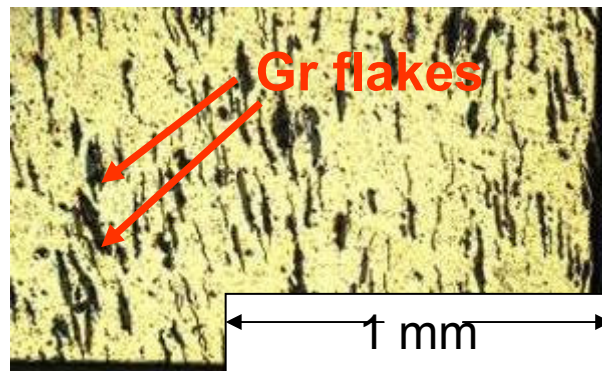
Figure 74: Optical microstructure image of 15Gr-85Cu

6.2 Microhardness Testing

The microhardness values are shown in Table 9 and Figure 75. The annealed

tungsten properties are obtained from CES EduPack level 3 database.

Table 9: Vickers hardness values

Material System Designation (volume %)	Microhardness (Vickers)
Annealed Cu	53
10W-90Cu	123
32W-68Cu	205
65W-35Cu	336
Annealed W	530*
C110 H04	143
15Gr-85Cu	114

*from CES EduPack 2010 [20]
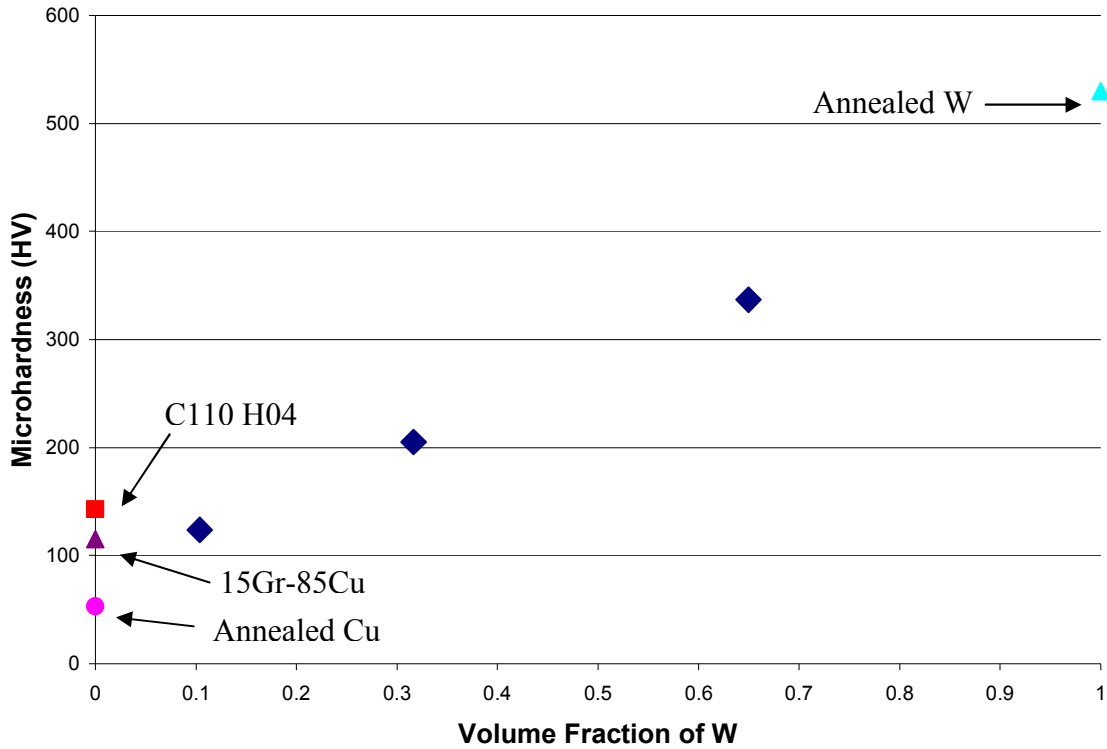
Figure 75: Dependence of Microhardness for on volume fraction of W.

The microhardness of 15Gr-85Cu and 10W-90Cu are below that of hardened copper. The 15Gr-85Cu hardness is nearly equivalent to the 10W-90Cu. This suggests that the increases in mechanical properties anticipated through the inclusion of W are negated by the substantial porosity, poor bonding, and inhomogeneity in the microstructure. The graphite flakes incorporated into the 15Gr-85Cu microstructure offer negligible structural performance toward the resistance of plastic deformation. The graphite actually compromises the hardness properties as illustrated by the reduction in hardness in Figure 75.

With progressive increases in W reinforcement, hardness values increase significantly. This behavior is attributed to the increased presence of W connectivity, as the hardness values begin to approach those of annealed tungsten. Evidence of this W

connectivity is presented in Figure 72 and Figure 73. The deformation resistance is dominated by the tungsten constituent; minimal W-Cu shared loading.

6.3 Tensile Response

The tensile responses of the W-Cu and C110 H4 materials are shown Figure 76. The tensile properties are summarized in Table 10. The influence of volume fraction of W on Young's modulus is shown in Figure 77.
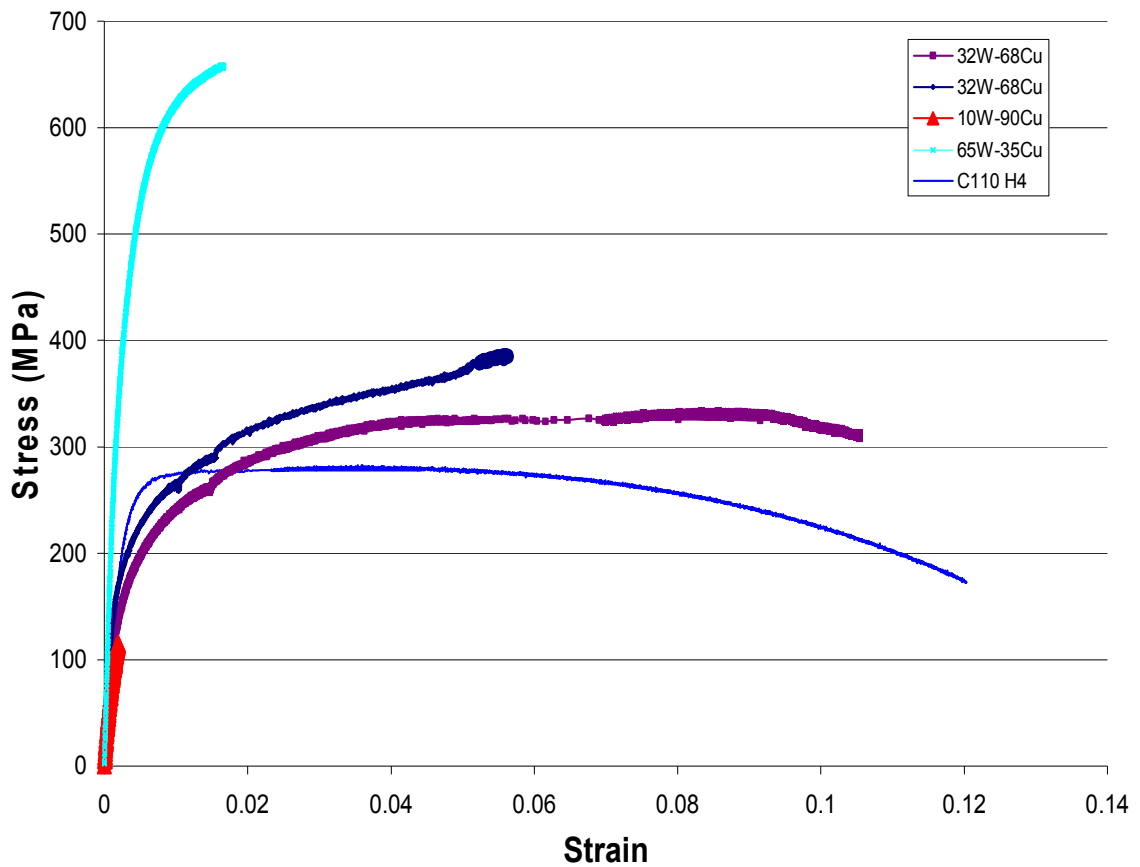
Figure 76: Stress-Strain plots for W-Cu and C110 H4

Table 10: Tensile Properties measured for each material

Material	Modulus (GPa)	Tensile Strength (MPa)	0.2% Offset Yield Strength (MPa)
Annealed Cu	120	210	45
10W-90Cu	87	115	115
32W-68Cu	173	360	200
65W-35Cu	226	660	500
Annealed W	340	1670	1350
C110 H4	128	280	255
15Gr-85Cu	N/A	28	N/A
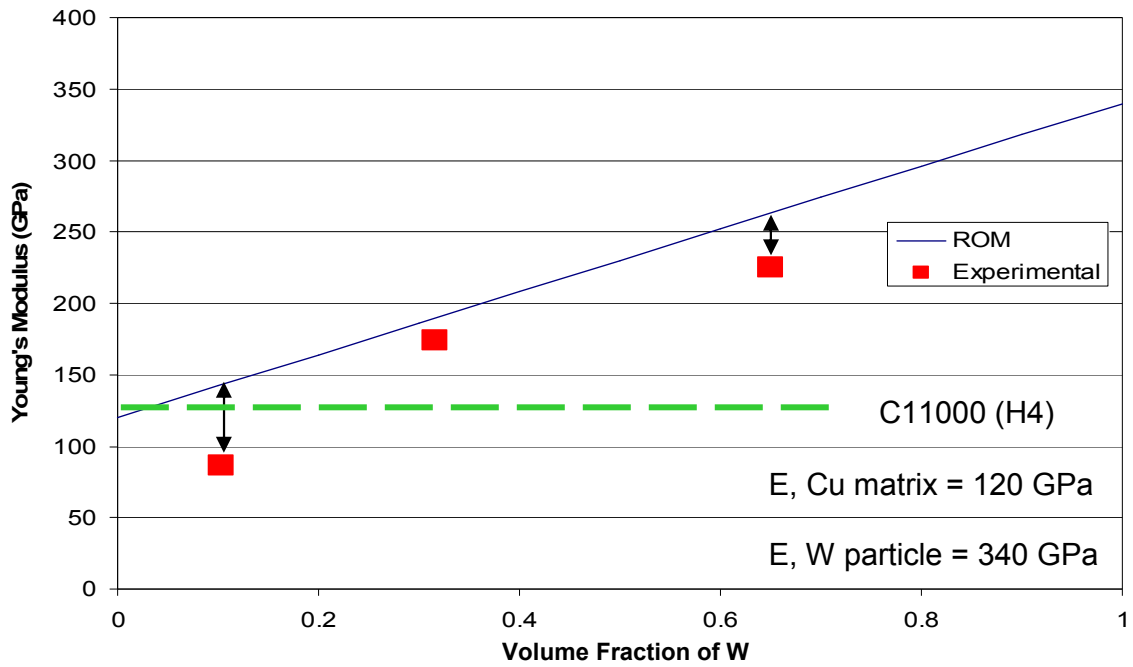
Figure 77: Influence of volume fraction of W on elastic modulus

6.3.1 10W-90Cu

The 10W-90Cu exhibited brittle behavior with a strength more than 50% lower than C110 H4. This behavior is attributed to several factors. Porosity is extensive throughout the material. Reduction from the ROM approximation of Young's modulus is consistent with the observations of poorly consolidated microstructure as shown in Figure 68 and Figure 69.

This is likely attributed to poor particulate and powder bonding between the W and Cu powders as well as Cu powders. A fully consolidated composite would be expected to achieve high ductility. Clearly the processing parameters for the 10W-90Cu are not optimized.

6.3.2 32W-68Cu

Analysis of the Young's modulus properties for the 32W-68Cu shows significantly better properties as compared with the 10W-90Cu. There is good agreement with the ROM. This observation indicates thorough consolidation within the matrix.

The yield strength of this material is nearly three times that of annealed copper. This indicates that there is strengthening due to the W constituent. Good bonding results in increased load transfer from the ductile copper matrix to the hard W reinforcement.

The observation of strain to failures on the scale of C110 H4 further suggests consolidation is good. The 32W-68Cu stress-strain curve exhibits strain hardening. The tensile strength is approximately 70% greater than its yield strength.

The 32W-68Cu is observed to fail in a ductile manner as shown in Figure 78. This type of fracture surface is indicative of a ductile matrix, such as copper, with good

consolidation. The dimples indicate ductile deformation within the Cu matrix as the material is strained to failure [91].
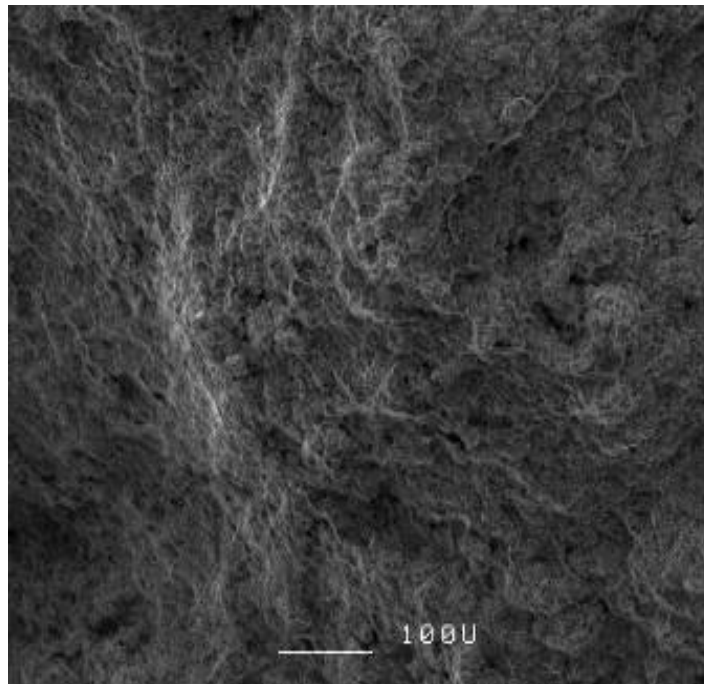
Figure 78: SEM image of 32W-68Cu fracture surface

6.3.3 65W-35Cu

The Young's modulus of the 65W-35Cu material is slightly lower than the values estimated by the ROM. The yield strength of this material is nearly twice the strength of the 32W-68Cu material. The interconnectivity of the W is the main contributor to the strength of this material.

The strain to failure of this composite is less than 2%. This value represents less than 20% of pure tungsten. The poor interfacial properties between W-Cu also prohibit the extended strain to failures expected with the inclusion of ductile copper [39]. Strain hardening is observed in this material as well.

114

The 65W-35Cu fracture surface is shown in Figure 79. A coarse fracture surface is presented. This SEM image shows the irregularity of the fracture surface, due to limited plastic deformation prior to fracture [91]. This corresponds to the prevailing interconnectivity of the W that is shown in Figure 72 [89].
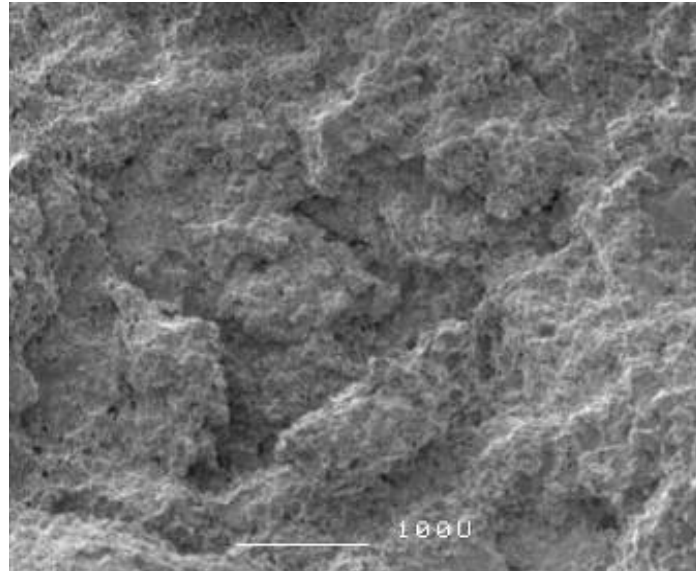
Figure 79: SEM image of 65W-35Cu fracture surface

6.3.4 15Gr-85Cu

The strength of this composite is extremely low as shown in Table 10. The mechanical properties of the flakes are such that they offer no mechanical contributions to the material system. The flakes provide a preferential path of crack propagation without an appreciable resistance to crack growth or fracture toughness.

6.4 Young's Modulus

The experimentally measured modulus values are compared to several modulus estimation models, ROM, Paul [52], and Warpole [53], in Figure 80.   The ROM plot is generated using copper and tungsten Young's modulus values of 120 and 340 GPa, respectively. The curves representing the Warpole [53] model reflect inputs of copper bulk and shear modulus values of 130 and 44 GPa, respectively, and the tungsten bulk and shear modulus of 246 and 130 GPa, respectively. The two Warpole curves represent a bounded value for the anticipated Young's modulus values based upon the aforementioned material inputs. The small deviation of the Warpole model observed at the extremities of pure Cu and pure tungsten is explained by the utilization of the bulk and shear moduli in the Warpole estimation, where as, the Young's modulus of the respective constituent is directly utilized in the ROM and Paul [52] models. The Paul model is also generally representative of the experimental response, closely following the upper bound of the Warpole model, suggesting that the assumptions of isotropic constituent particles and constant stress are appropriate. Good agreement is observed, particularly with the upper bound curve.

Large deviation of 10W-90Cu Young's modulus value suggests significant porosity and poor bonding. Due to the relatively low reinforcement concentration, the Young's modulus is concluded to be deleteriously affected by the lack of thorough consolidation and structural integrity in the copper matrix. The prevailing porosity precludes the measured value from being within the Warpole lower bound. This fact brings forth the anisotropic nonhomogenous traits of the microstructure.

116

The relatively good agreement between the 32W-68Cu measured value and the ROM suggests substantially less porosity and increased matrix-particle bond strengths as indicated by the assumptions in the ROM formulation. This premise is further supported by the good ductility exhibited in tensile testing and the observation of a ductile fracture. The Warpole upper curve slightly underestimates the Young's modulus value. At this reinforcement concentration, approximately 32% of the microstructure is W particles with significant interconnectivity. Consequently, the Warpole upper bound approximation does not capture the contributions of the high stiffness W connectivity within the microstructure.

The deviation from ROM increases for the 65W-35Cu indicates an increased porosity as the tungsten concentration is increased from 32 vol.%. This reduction is likely attributable to the fact that the tungsten concentration is more than twice that of the copper concentration in the 32W-68Cu. Despite this increase in tungsten, the particle sizes and sintering parameters are not adjusted to ensure full consolidation and good mechanical bonding for the given size and volume fraction ratios [27], [89]. The Young's modulus is accurately captured within the Warpole approximation bounds. This highlights the ability of the Warpole model is estimate the Young's modulus for high particle concentrations, provided the microstructure is relatively uniform and well consolidated.
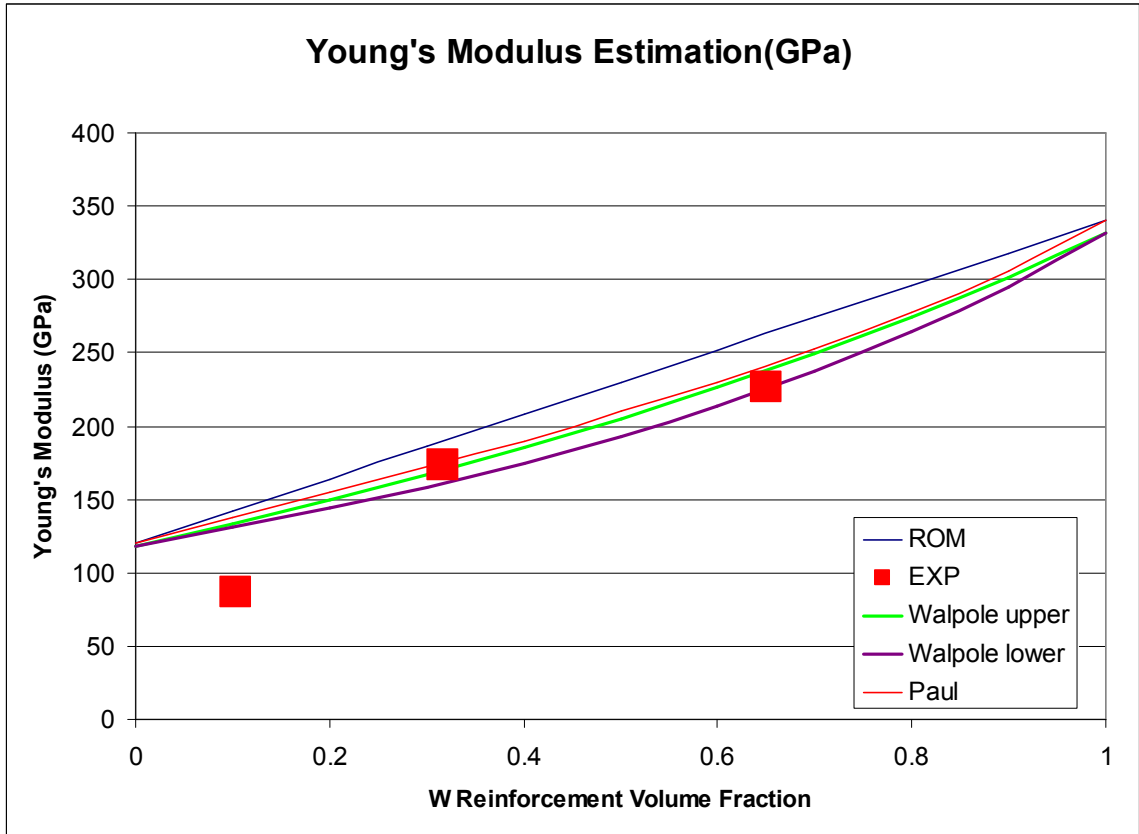
Figure 80: Comparison of experimental and model estimation values of Young's modulus

6.5 Yield Strength

For comparison purposes, yield strength as a function of W volume fraction plots are generated for each model in Figure 81. The experimental yield strength values are superimposed in this graph. The annealed copper and annealed tungsten yield strength inputs of 58 and 1350 MPa, respectively, were utilized for each model. These values were obtained from CES EduPack [20].
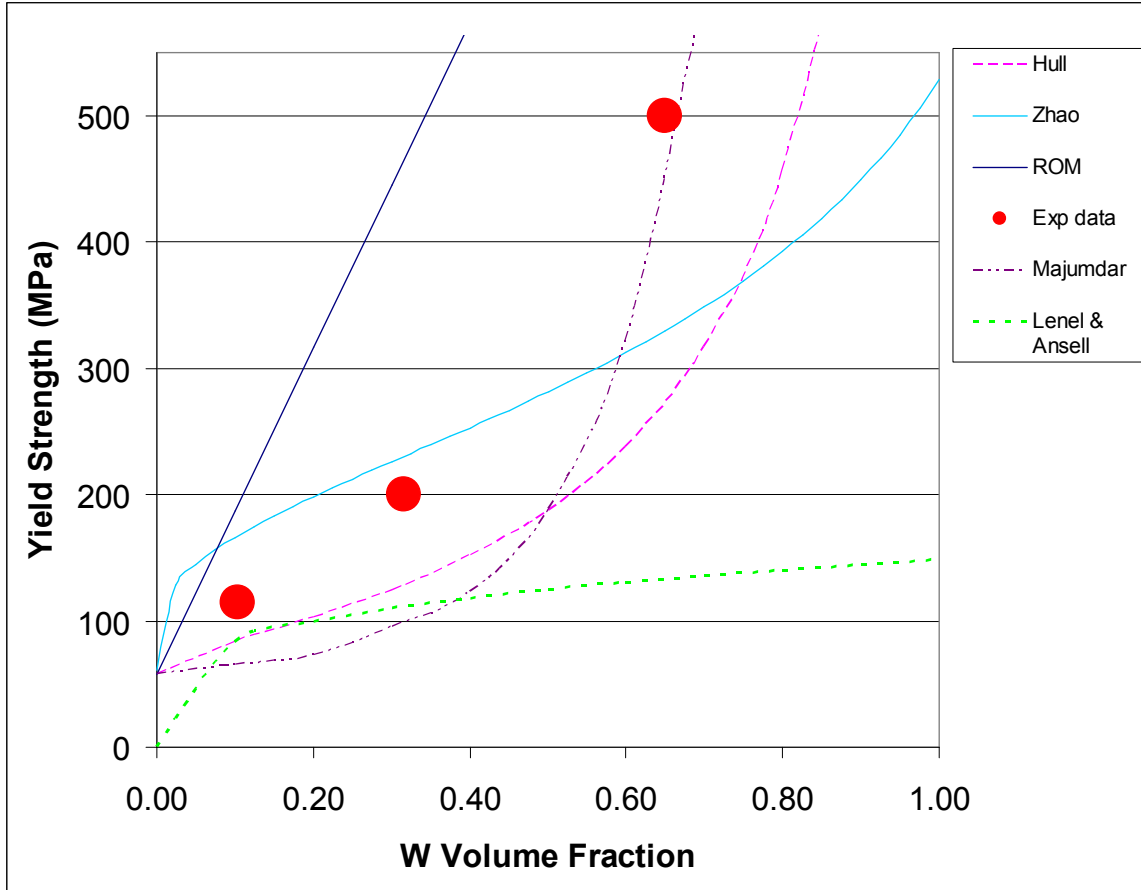
Figure 81: Comparison of experimental and model estimation values of yield strength

The Zhao et al. [63] model shows relatively good agreement at the lower volume concentrations of tungsten. This suggests that the primary strengthening mechanism is resistance to dislocation motion due to increased dislocation density near matrix-particle interfaces.

The increase in the experimentally obtained 65W-35Cu yield strength data suggests the presence of additional strengthening mechanisms at volume fractions exceeding approximately 40%. The additional strengthening due to the W connectivity interactions must be captured for accurate modeling. The model presented by Majumdar and Pandey [66] provides a means of capturing this effect. The work hardening exponent of the composite is generally assumed to be accurately approximated by the matrix work

hardening exponent [66]. This assumption is invalid for situations of significant plastic flow constraint (e.g., disc or needle shaped reinforcement, concentrations exceeding 60%). This phenomenon has been extensively investigated by Cleveringa et al. [92]. Microscopy characterizations reveal localizations of W concentrations that well exceed 60%. Based on these pillars of justification, the curve representing a work hardening exponent of 0.6 is presented in Figure 81. Relatively good agreement is obtained for the 65% reinforcement concentration. The basis of the Majumdar and Pandey [66] model is centered on the unit cell approximation [65] containing single particulate as shown in Figure 50; therefore, some inaccuracy could be introduced at volume fractions approaching and/or exceeding 66%. At these reinforcement concentration levels, the assumption of a single particle per unit cell is no longer applicable and the model accuracy is compromised.

At lower volume fractions, the strength behavior is described by the Zhao et al. [63] Hall-Petch inspired model. The higher reinforcement levels require additional strengthening mechanisms to be accounted. for as demonstrated by the Majumdar and Pandey [66] model with proper adjustment of the work hardening exponent to reflect the high concentration levels of the hard high modulus W reinforcement. The transition point between the dominant strengthening mechanisms is approximated at 57% W volume fraction.

6.6 Electrical Resistivity

NAECO provided resistivity values for each of the W-Cu composites is shown in Table 11. These values were obtained through the use of the four point probe method.

Table 11: W-Cu composite conventional electrical resistivity

Material System	Electrical resistivity (μΩ-cm)
10W-90Cu	2.4
32W-68Cu	3.8
65W-35Cu	5.8

Measured resistivity values are larger than those predicted by the ROM. This indicates resistive contributions within the microstructures. The Cu-W phase diagrams illustrate that no intermetallics are formed between W and Cu. The previous mechanical response observations clearly demonstrate prevalent porosity in the 10W-90Cu and 65W-35Cu microstructures. It is understood that porosity is also responsible for reduced electrical conductivity properties [77], [84], [86].

The 32W-68Cu is less than 35% more conductive than the 65W-35Cu despite having twice as much copper included in the microstructure. The measured resistivity for the 65W-35Cu slightly exceeds the resistance of pure W. The 65W-35Cu resistivity is attributed to lack of Cu connectivity throughout the microstructure. According to percolation theory and other models that were previously presented in Chapter 3, 35 vol.% Cu is an adequate Cu inclusion to ensure Cu connectivity in the microstructure [77],[78],[79]. This observation suggests insufficient processing parameters to yield homogenous distribution of the Cu throughout the microstructure. The preceding discussion of tensile properties dominated by W connectivity further corroborates the perspective of minimal Cu connectivity. Microscopic images shown in Figure 72 and Figure 73 support these findings.

The measured conductivities of the W-Cu materials are shown in Figure 82. The pure copper and pure tungsten electrical conductivities implemented in the models are 58.8 and 16.7 m/μohm, respectively. These values were obtained from the CES EduPack [20].
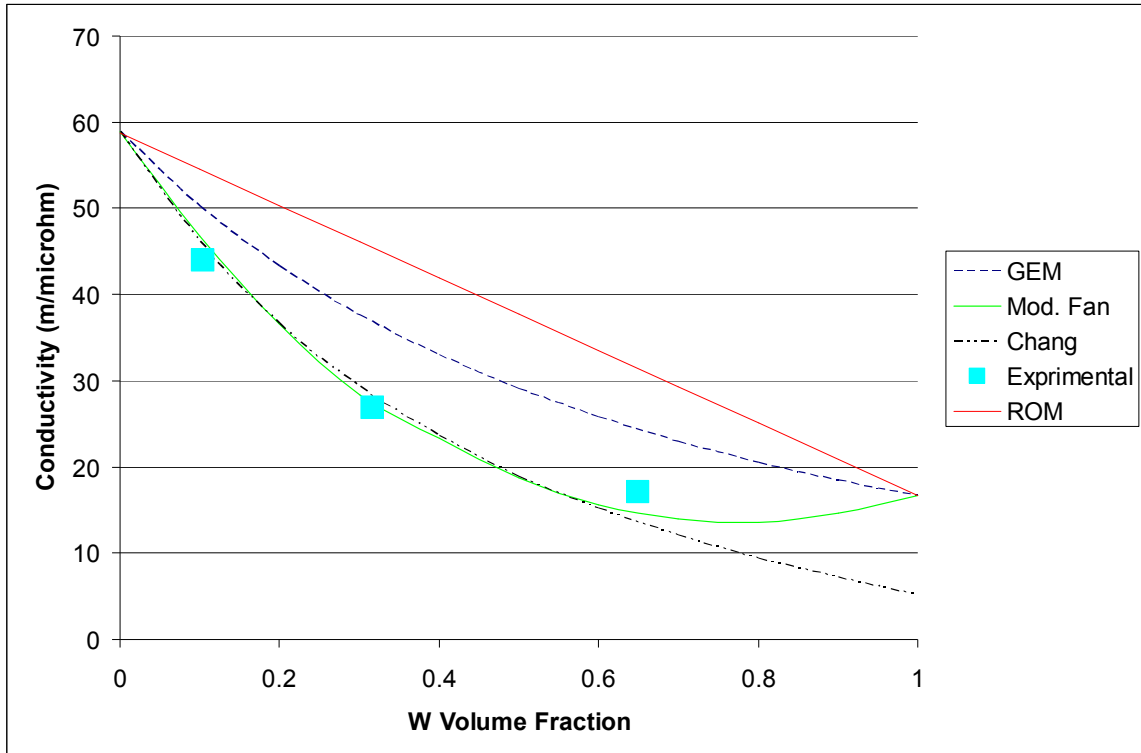
Figure 82: Comparison of experimental and model estimation values of electrical conductivity

The ROM and GEM models overestimate the electrical conductivities. These models fail to capture any resistive elements within the composite microstructure (e.g. porosity, dislocation densities).

The model by Chang et al. [86] addresses the influences of increased dislocation density due to particle-matrix interactions. This model is derived based on a unit cell approximation as shown in Figure 59; hence the accuracy of this model is compromised at concentration levels that yield appreciable W connectivity (i.e., as in the 65W-35Cu).

This model displays good agreement with experimental data at concentration levels below 50% W volume concentration. Conductivity predictions for this model decrease beyond W levels, because the reduction in conductivity becomes unbounded at approximately 66% volume concentration due to unit cell approximation and dislocation density assumptions.

A new model is introduced that is based on the approach by Fan [84]. This model utilizes equivalent circuit decomposition to approximate complex heterogeneous microstructures by three simple resistor circuits in parallel as shown in Figure 56 and Figure 57. One of the three resistors is comprised of the matrix-particle resistivity, while the other two circuits are defined by the resistivity of the two constituent materials. The modified Fan model utilizes a power law approximation to estimate the contiguous Cu and W volume fraction contributions to electrical conductivity. The power law approximation is utilized to relate the contiguous and total volume fraction of each constituent. This approximation is presented in

$$f_{\alpha c} = f_\alpha^m$$
$$f_{\beta c} = f_\beta^n$$

(44)

where $f_{\alpha c}$, $f_{\beta c}$, are contiguous volume fraction of constituent α and β, respectively. m and n typically range between 2 and 4. Here we used $m = 1.5$ and $n = 2.2$ based on the work by Werner and Stuwe [85].

It is presumed that the contribution to the electrical conductivity from W-Cu path of current flow in terms of volume fraction is negligible. The high levels of concentrated porosity at the W-Cu interfaces within the 10W-90Cu shown in the microstructure images, Figure 68 and Figure 69, support this perspective.

The 32W-68Cu microstructure is shown, Figure 70 and Figure 71, to be comprised of significant Cu connectivity and W connectivity. The conductivity of this material is therefore accurately modeled by considering the conductivity component based upon the W-Cu interaction as negligible when compared on a volume percent basis to contiguous W and contiguous Cu conductivity circuit contributions.

The 65W-35Cu conductivity is underestimated by the Modified Fan model. The lack of ductility in this material supports the thought of limited W-Cu bonding. This deviation is explained by the overwhelming tungsten connectivity. The as-received viewgraphs and mechanical properties clearly demonstrate W connectivity. The degree of contribution stemming from the W connectivity can be more appropriately modeled by increasing the estimated amount of contiguous W volume fraction. When the entire 65% volume fraction of tungsten is approximated as contiguous, the Modified Fan predicts the 65W-35Cu nearly exact.

6.7 Pulsed High Current Density Tests

The current versus time plot is displayed in Figure 83. The current is shown to be 55,000 amps which for the specimen geometry equates to a 1.2 Ga/m^2 current density. These current plots were the same for each exposure conducted. Voltage plots for the first exposures of each material are shown in Figure 84 through Figure 87. Voltage plots for each material generated during the last of three repeated exposures are shown in Figure 88 through Figure 91. The measured peak voltage for each exposure is given in Table 12

Table 12: First, second, and third voltage measurements for each material

Material System	First Exposure Voltage (Volts)	First Exposure Resistivity ($\mu\Omega$-m)	Second Exposure Voltage (Volts)	Second Exposure Resistivity ($\mu\Omega$-m)	Third Exposure Voltage (Volts)	Third Exposure Resistivity ($\mu\Omega$-m)
C110 H4	5.8	0.38	5.6	0.37	5.2	0.34
10W-90Cu	7.7	0.50	7.2	0.47	7.5	0.49
32W-68Cu	8.9	0.58	9.1	0.59	9.2	0.60
65W-35Cu	10.2	0.67	10.3	0.67	10.1	0.66
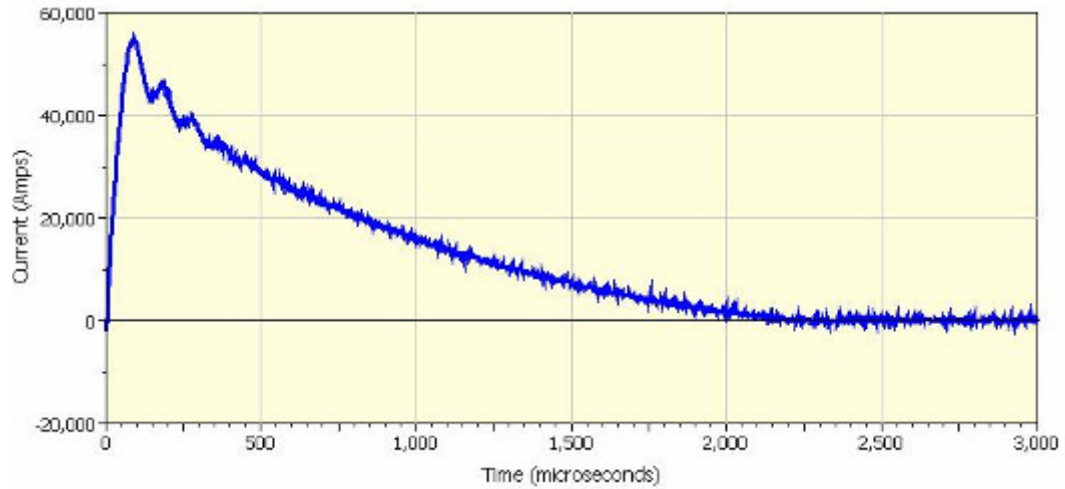
Figure 83: Representative current plot for 1.2 Ga/m^2 current density.
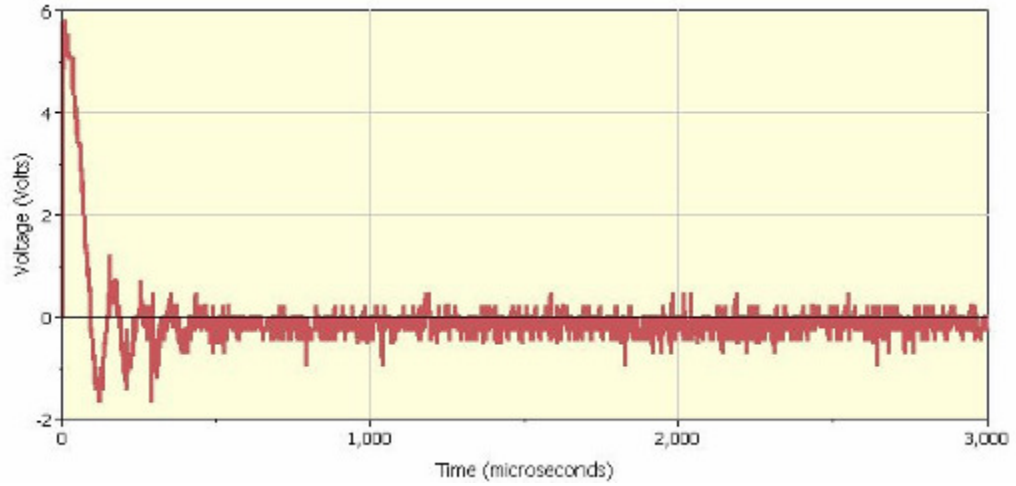
Figure 84: Voltage plot for Cu110 H4 after one exposure of pulsed high current density.
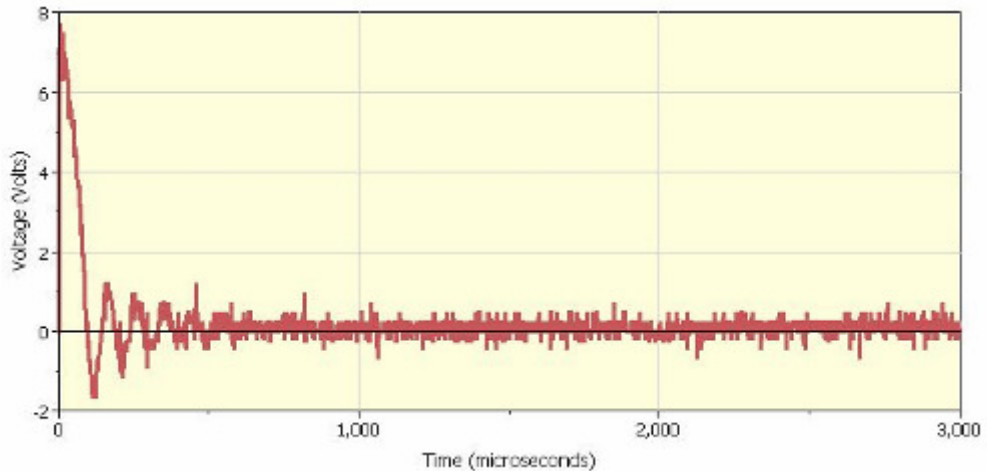
Figure 85: Voltage plot for 10W-90Cu after one exposure of pulsed high current density.
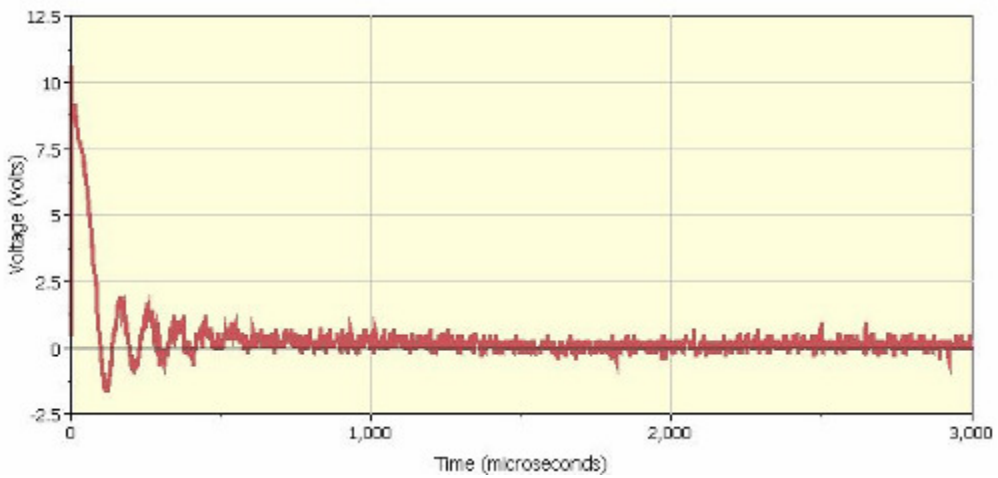
Figure 86: Voltage plot for 32W-68 Cu after one exposure of pulsed high current density.

126
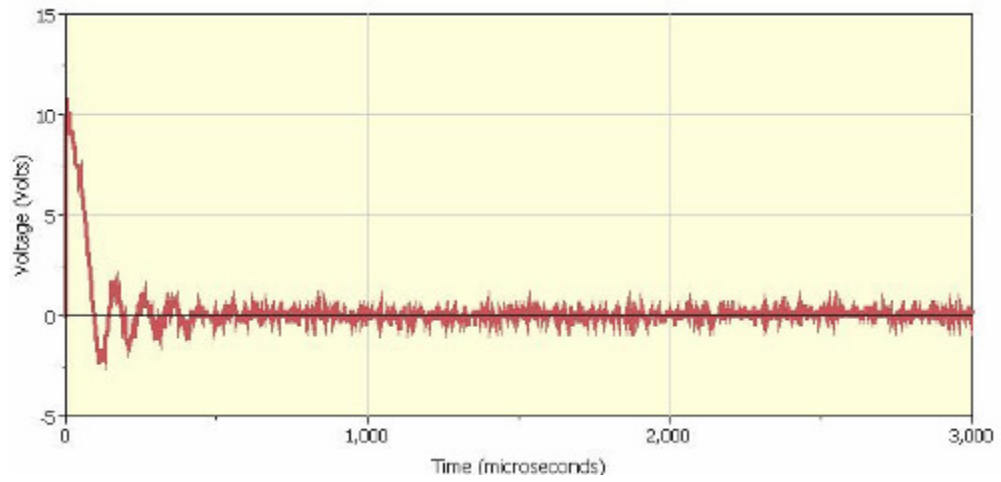
Figure 87: Voltage plot for 65W-35Cu after one exposure of pulsed high current density.
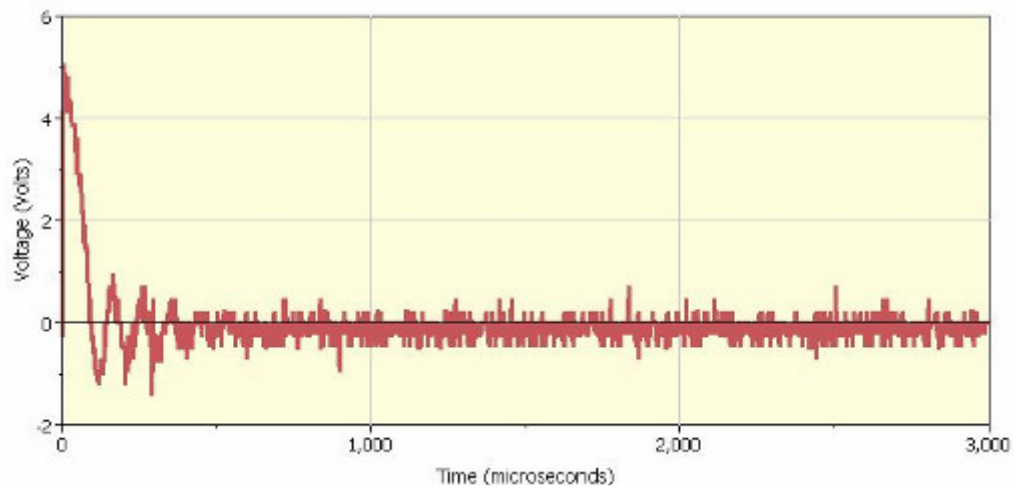
Figure 88: Voltage plot for Cu110 H4 after third cyclic exposure of pulsed high current density.
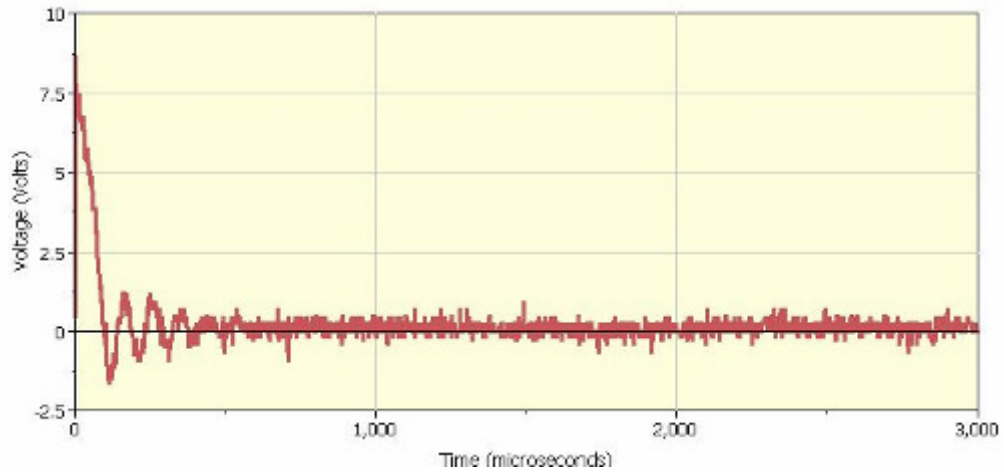
Figure 89: Voltage plot for 10W-90Cu after third cyclic exposure of pulsed high current density.
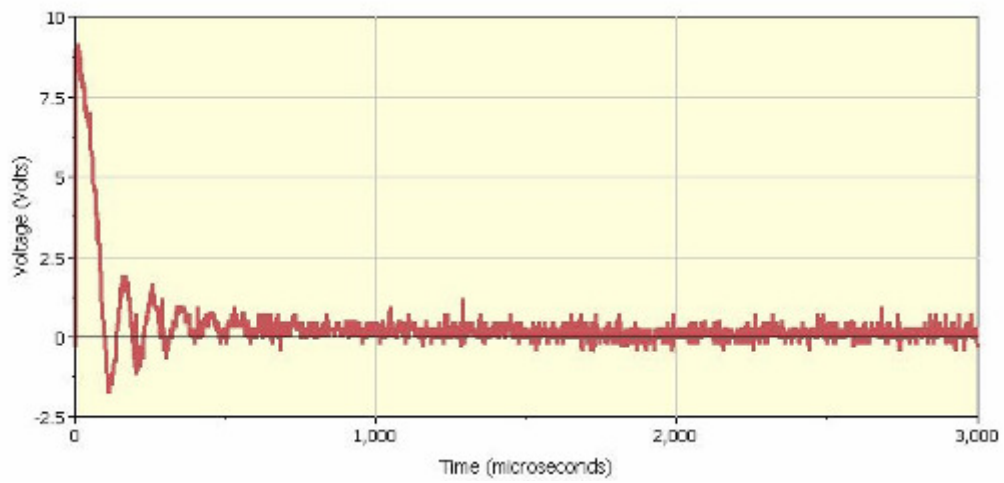
Figure 90: Voltage plot for 32W-68Cu after third cyclic exposure of pulsed high current density.
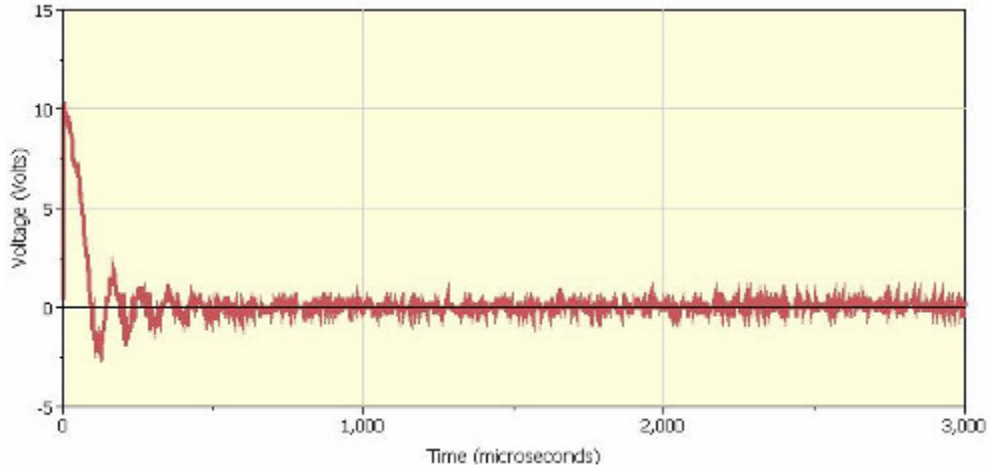
Figure 91: Voltage plot for 65W-35Cu after third cyclic exposure of pulsed high current density.

The peak voltages recorded during the pulsed high current density exposures were then utilized to calculate peak resistivity values for each material through the following approach. Ohms law is used to obtain the pulse resistance, R_p, for each exposure as described by

$$R_p = \frac{V_{pk}}{I_{pk}} \tag{45}$$

using peak values for both voltage and current, V_{pk} and I_{pk}, respectively. The resistance is then related to the specimen cross-sectional area and length to determine the corresponding peak electrical resistivity values as

$$\rho_{pk} = \frac{R_p \cdot A}{L} \tag{46}$$

where ρ_{pk}, A, and L are peak electrical resistivity, gage cross-sectional area, and gage length (i.e. distance between wire lead attachments), respectively. The values obtained are summarized in Table 12. These values are plotted against the conventional resistivity measurements obtained using the four point probe measured values in Figure 92. The

129

C110 H04 electrical resistivity is taken from published specifications in the CES

EduPack [20].
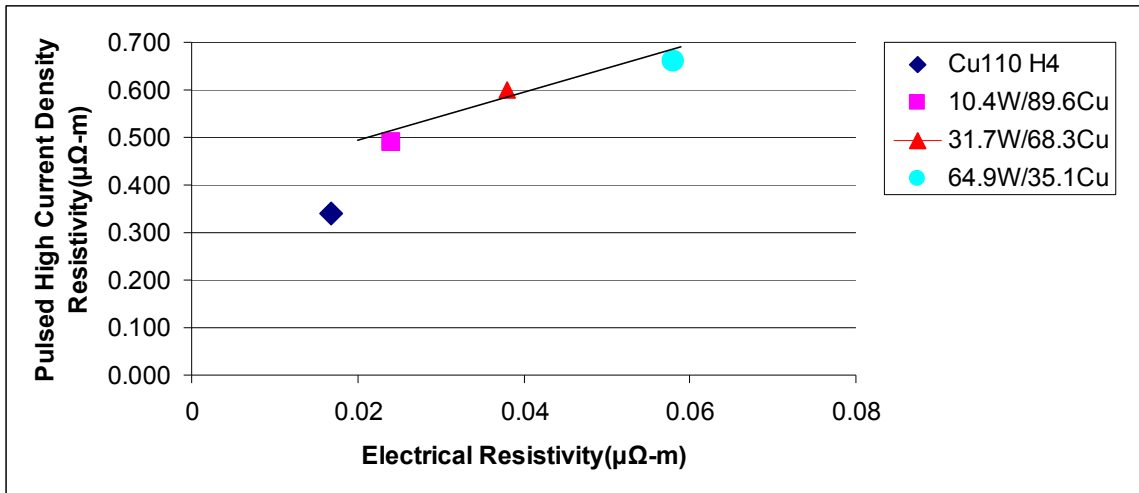
Figure 92: Comparison of pulsed high current density and standard electrical resistivity

The resistivities measured in the pulsed high current density experiments are

significantly larger by more than an order of magnitude than those measured by the

conventional four point probe using low current. The pulsed current is certainly not

uniform across the entire cross-section. The increased resistivity is attributed to two

factors: system configuration and electrical current skin effect. The current flows into the

specimen along the circumference of the gripped section. The current also exits the

specimen in the same manner from the opposite gripped section. As a result, flow of the

charged particles is potentially concentrated near the surface of the specimen.

Due to the pulse release of the current from the capacitor bank, a transient

response similar to those obtained in alternating current systems is generated. Magnetic

field variations within the conductor are produced during the brief pulse of extreme high

current. The skin effect phenomenon describes the concentration of electrical current

along the surface of the material; consequently, there is a significant reduction in the

130

cross-sectional area that carries the current flow. This occurrence is due to variation of the magnetic fields and associated eddy currents that effectively prohibit current flow through the core of a cylindrical conductor. The electrical resistance is effectively increased. The interruption to uniform current flow across the entire cross-sectional area is significantly increased with the variation of the applied current. The effective skin depth (i.e., distance from the conductor surface through which current flows) can reduce several orders of magnitude as a function of the transience in the current waveform [93].

The voltage values are consistent from the first through the third exposures. The voltage data is analyzed to characterize the level of confidence in the outputted peak values. Based on the sampling rate, a minimum of 150 data samples are collected within the timeframe the maximum voltage occurs. Approximately fifteen pulsed high current density tests were conducted during the course of this research. The maximum voltage data for each material system was consistent for each material system throughout repeated exposures, monolithic as well composite microstructures. The more resistive material systems yielded higher peak voltages as expected in each test. The voltages recorded during the pulsed high current density exposures for each material were correlated to the four point probe resistivity values for each material. There is a linear correlation between the resistivity measured by pulsed high current density and the resistivity measured by the four point probe method, shown in Figure 92.

Since the current release is pulsed, the peak current is only experienced by the specimen for approximately 20 µs. At 500 µs into the pulsed exposure, the current level is nearly half of the maximum value as shown in Figure 83. The estimated temperature rise for this energy input is well below the levels necessary to produce appreciable

microstructure changes. Quantitative approximation of the Joule heating is achieved through the use of Joule's first law

$$Q = I^2 \cdot R \cdot t \qquad (47)$$

where I, R, t, and Q are current, resistance, time, and heat energy, respectively. This resistive heat input is related to the change in temperature by

$$Q = m \cdot C_p \cdot \Delta T \qquad (48)$$

where m, C_p, and ΔT are mass, specific heat capacity, and temperature change, respectively. Even for the most resistive composite, 65W-35Cu, a temperature rise of less than 10°C is achieved. Physical properties (e.g., electrical resistivity) are therefore not significantly affected; consequently, the peak voltage for a given a material is not expected to change for subsequent exposures. No observable microstructural effects were found during visual and optical microscopy observations.

6.8 Comparison of properties on Ashby charts

The properties measured are plotted on the Ashby material maps presented in Chapter 2. The hardness and tensile strengths versus electrical resistivity are shown in Figure 93 and Figure 94, respectively.
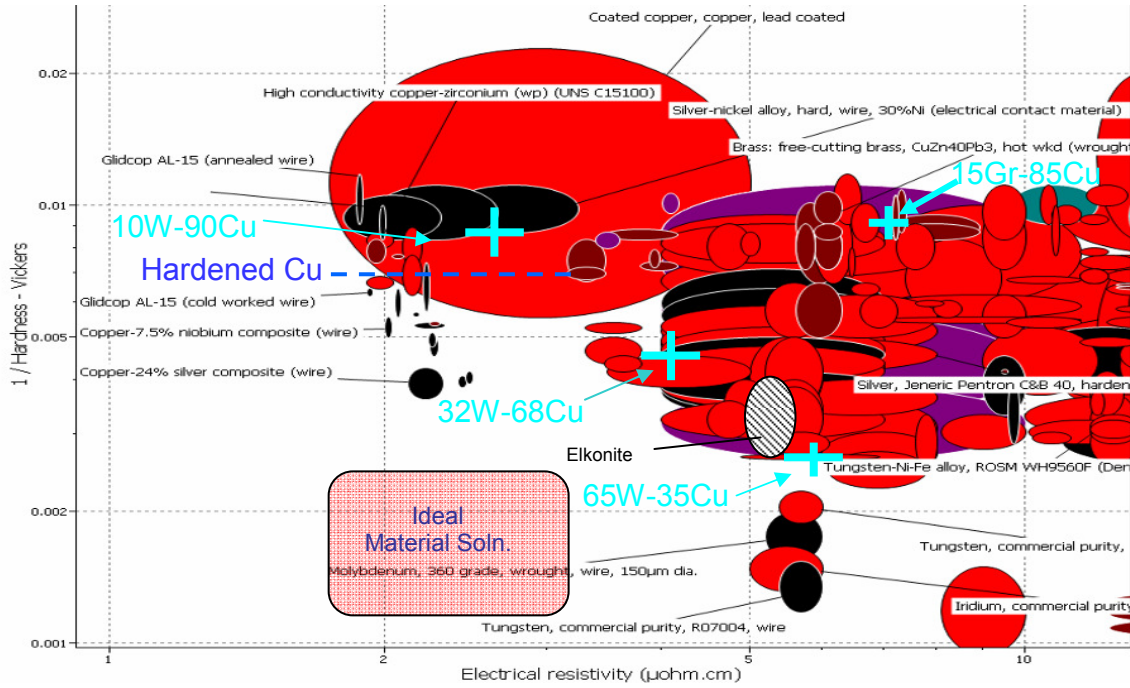
Figure 93: Ashby plot of hardness and electrical resistivity potential showing locations of W-Cu, Gr-Cu, and C110 H4
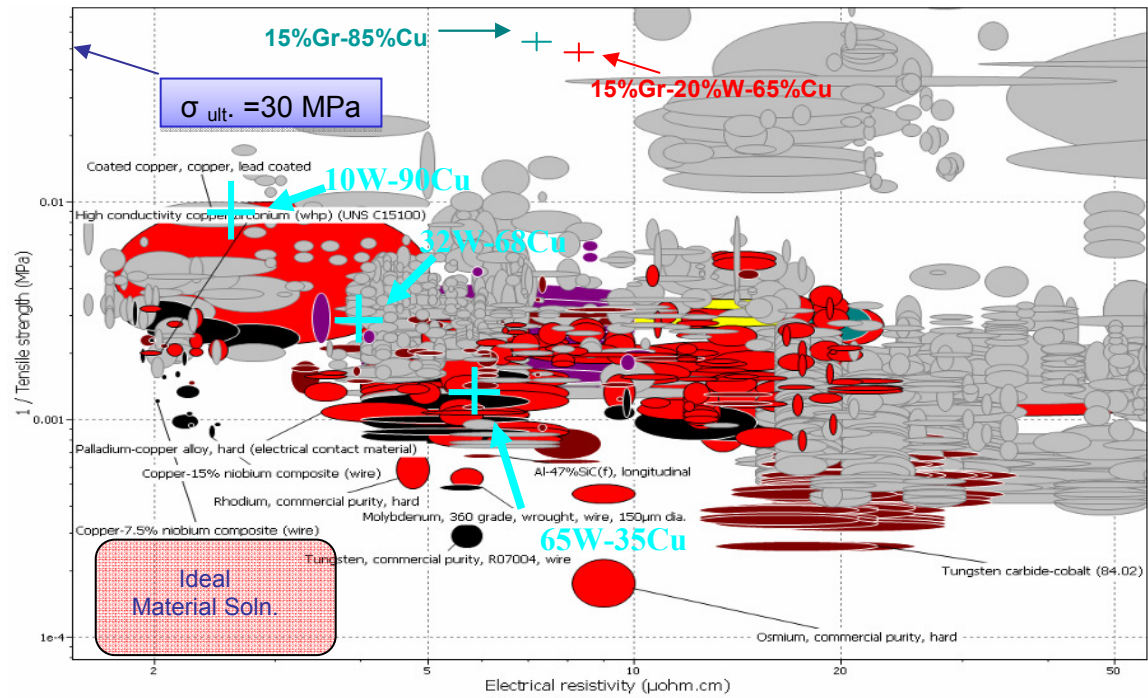
Figure 94: Ashby plot of tensile strength and electrical resistivity potential showing locations of W-Cu, Gr-Cu, and C110 H4

133

All of the W-Cu particulate systems are dominated solutions, meaning there are conventional materials closer to the Pareto frontier. The Pareto frontier represents the subset of conventional materials that provide the best trade-off between good tensile strength and minimal electrical resistivity. For the composites characterized in this study, the marginal increase in strength is accompanied by an undesirable electrical resistivity increase of nearly 300%. This suggests that alternative hybrid configurations, such as open-faced sandwich as discussed in Chapter 2, are likely a better means of obtaining a material that fills the desired white space on the Ashby chart.

Chapter 7: Conclusions and Recommendations

Extreme electrical contacts require multifunctional materials that combine good conductivity with good wear resistance. A methodology for selecting and designing suitable materials was laid out and exercised in this study. Specification of the screening constraints and objectives lead to the derivation of material indexes for materials selection. The conflicting objectives identified for extreme electrical contacts were to minimize electrical resistivity and maximize wear resistance. Two possible models for maximizing wear resistance were investigated.

Both tungsten alloys and W-Cu composites were shown to be candidate materials. Several particulate W-Cu composites with different volume fractions of W were obtained and characterized. Materials design relationships for electrical conductivity and yield strength of W-Cu particulate composites were identified and verified. In addition, other hybrid configurations such as coating or cladding of a substrate were also identified as potential materials solutions.

The following sections present conclusions and recommendations that are derived from the materials selection and material characterizations. These conclusions and recommendations are separated into principal and secondary findings.

7.1 Conclusions

7.1.1 Materials Selection

Currently, material solution exploration for extreme electrical contacts is an expensive, time consuming, empirical trial and error approach. A systematic material

selection study using the Ashby method has been conducted to quantitatively identify, compare, and rank the materials in the Pareto set defined by the conflicting objectives. Hybrid materials and alternative configurations are identified that enhance both conductivity and wear resistance.

7.1.1.1 Principal

- The primary conflicting objectives for extreme electrical contacts are maximizing wear resistance and minimizing Joule heating, which leads to minimizing electrical resistivity. Two possible models for maximizing wear resistance were identified and used to derive material indexes: (i) Archard's wear and (ii) thermally assisted melt erosion. Tungsten alloys are non-dominated solutions for both wear mechanisms; consequently, these alloys are particularly promising for extreme electrical contact applications.

- To fill the "white spaces" of the Ashby material charts, opportunities of designing a hybrid material may offer significant improvement. Potential configurations include particulate composites, "open-faced" sandwich (coating, cladding), or layered structures. Property curves for hybrid material solutions plotted on Ashby plots suggest that potential performance increases of nearly an order of magnitude are possible based upon the projected wear properties of these composites compared to those of hardened copper.

7.1.1.2 Secondary

- Plots of material metrics representing these conflicting objectives suggest that hardened copper and tungsten alloys are in the Pareto set (i.e., each is a non-

dominated solution) for both wear mechanisms. The hardened copper values minimize electrical resistivity well, while tungsten alloys may be a better compromise between increased wear resistance while maintaining minimal electrical resistivity. Tungsten alloys are approximately four times more resistive than hardened copper, but they possess hardness and maximum service temperature increases by factors of three and seven, respectively. Tungsten carbide is 15 times harder than copper, while increasing resistivity by a factor of six. This suggests that one may be able to use tungsten alloys or even tungsten carbide to obtain greater durability if an increase in electrical resistivity is permissible.

- Analysis utilizing the EduPack Level 3 database provides a Pareto set of candidates that potentially provide a reasonable trade-off of minimal electrical resistivity and good wear resistance. If wear is controlled by hardness then, tungsten, molybdenum, copper-silver composites, copper alloys, and titanium diboride lie along the Pareto frontier, the materials with the best trade-off of properties for these two conflicting objectives. If wear is controlled by thermally-assisted melt erosion, then tungsten, molybdenum alloys, tantalum, tungsten alloys, tantalum alloys, copper alloys, copper-based composites, and molybdenum disilicide are potential candidates for mitigating the thermally-induced surface degradation.

- Several alternative configurations combining copper with another material were considered for extreme electrical contacts. Alternative configurations of coatings and particulate composites are suggested. Tungsten, cobalt, hafnium, tantalum,

and molybdenum are particularly promising coatings/claddings due to their refractory and hardness properties. Several relatively conductive carbide reinforcements are identified as potential particulate constituents. Tantalum, tungsten, and tungsten-cobalt carbides are highlighted for their combination of hardness and conductivity properties. Tantalum, tantalum-tungsten, molybdenum alloys are non-dominated solutions for maximum service temperature. Molybdenum disilicide and titanium diboride are nearly non-dominated for both wear considerations.

- Comparison of widely utilized refractory materials (i.e., molybdenum, tantalum, iridium, and niobium) for hardness and maximum service temperature shows that tungsten is nearly a non-dominated solution for both. It is slightly dominated by iridium for hardness, but it only costs a fraction of iridium. So, tungsten is the most viable choice as a refractory constituent in a hybrid material, with molybdenum secondary.

7.1.2 Candidate Material Characterization

As a result of the material selection exercise, several candidate particulate composite materials were obtained and evaluated. These included copper-tungsten W-Cu, "self-lubricating" graphite-impregnated Cu, and Gr-W-Cu composites with different volume fractions of the constituents. The structure-property relations were determined through mechanical and electrical resistivity testing. In this study, physics- and micromechanics-based models were used to estimate yield strength and electrical conductivity values as a function of constituent volume fractions. These relationships are

useful in plotting the hybrid property relationships as a function of microstructure attributes on Ashby material charts, which has utility in accelerating the design of these classes of materials.

7.1.2.1 Principal

- A novel test method was established and validated for exposing candidate materials to single and cyclic pulsed high current densities (1.2 GA/m^2) that are equivalent to those in extreme electrical contacts. A unique aspect of this test method is the ability to perform subsequent mechanical characterizations following the high current exposures.

- Models to estimate the yield strength and electrical resistivity of the composite materials over the entire range of W volume fraction were identified and captured the experimental response. The estimated yield strength and electrical resistivity properties for each volume fraction had a maximum percentage error of approximately 18 and 7%, respectively. For the 32 and 65% W volume fraction, there is less than 10% deviation from the experimentally obtained data.

7.1.2.2 Secondary

- Microscopic characterizations of the 32W-68Cu and 65W-35Cu reveal nearly full consolidation. The yield strength of the 65W-35Cu is nearly twice that of the 32W-68Cu, while only achieving a small fraction of its ductility. These tensile responses are attributed to the significant W connectivity.

- Microscopic observations of the 10W-90Cu showed concentrated porosity in the vicinity of the W particles as well as within the Cu matrix. Consequently, electrical conductivity is reduced and the mechanical properties are characterized by brittle behavior. Microscopy and property characterizations suggest processing parameters were not optimized to yield a representative 10W-90Cu composite.

- The electrical resistivity values obtained for 1.2 GA/m^2 loads were empirically correlated to conventionally measured resistivity values of the materials. The relationship between the two resistivities is approximately linear, though the values obtained under the high current density were more than an order of magnitude larger. No observable microstructural changes occurred.

- The yield strength values for W-Cu composites ranging in W volume concentration from 10 to 65% are accurately modeled. The yield strength of W-Cu with W volume fractions of 10, 32, 65% were 115, 200, and 500 MPa, respectively. The yield strength at lower volume fractions is accurately modeled with a Hall-Petch inspired model. The 65W-35Cu yield strength is controlled by work hardening of the matrix due to severe plastic flow constraint from the high concentration of W particles.

- Rule of mixture (ROM) approximations do not accurately model the conductivity of these materials. Electrical conductivity decreases more rapidly with increasing W concentration than predicted by ROM. A modification of the equivalent resistance decomposition model accurately models the electrical conductivity

140

properties of the W-Cu materials at each of the W volume concentrations to within 7% error.

- The graphite additions to Cu and W-Cu for "self-lubricating" yields extremely low structural properties coupled with elevated resistivity. Therefore, adding graphite for self-lubrication is not a viable solution.

7.2 Recommendations

Based upon the contributions and conclusions presented in this study, there are several areas of continued investment that will lead to better material solutions for extreme electrical contacts.

7.2.1 Materials Selection and Design

7.2.1.1 Principal

- A likely more viable hybrid material is an "open-faced" sandwich configuration; that is, substrates that are coated or cladded. To support this endeavor, material property estimation models need to be identified, and perhaps derived, for the structural and electrical properties of relevance so that one can estimate the properties of these potential hybrid materials.

- A materials design methodology for these coated or cladded hybrid materials needs to be developed with an eye toward these extreme electrical contact applications.

7.2.1.2 Secondary

- Two potential constituents for particulate composites to explore are molybdenum disilicide and titanium diboride. Both have higher hardness and maximum service temperature capability than W, while retaining relatively good electrical conductivity.

- The sensitivity of secondary properties that are important to materials in extreme electrical contacts needs to be evaluated. These properties include thermal diffusivity, specific heat, and modulus of elasticity.

- Determine maximum allowable resistivity for these extreme electrical contact applications. It is likely dependent on the power source limitations, performance requirements, etc. This quantitative specification will facilitate prioritization, possibly through defining an exchange constant that can be used to evaluate trade-offs in properties.

7.2.2 Candidate Material Characterization

7.2.2.1 Principal

- Coatings and claddings, or similarly graded surfaces, on a substrate look to be a promising hybrid configuration solution. Several other issues become important that need to be addressed. These include the adhesion strength of the coating on the substrate, the coating-substrate interfacial resistivity, the effective compliance, the residual stresses that develop, and the tribological properties which will depend on coating thickness and properties (modulus of elasticity, hardness, etc.).

A systematic mechanical and electrical property characterization, relevant to extreme electrical contacts, of potential coating-substrate material systems needs to be developed that takes into consideration the thickness of the coating/cladding, its adhesion strength, the residual stresses from processing and service, etc. in order to optimize the architecture and processing design of these new hybrid materials.

- Physics- and micromechanics-based models are needed to predict the effective properties of these hybrid materials so they can be plotted on Ashby charts. These relationships will aid in the selection and design of coating/cladding solutions.

7.2.2.2 Secondary

- In an effort to address the thermal contributions to the service environment of extreme electrical contacts, it would be useful to utilize an impulse heat source to induce a localized instantaneous temperature rise. This test would facilitate a fundamental understanding of the material response to the extreme thermal conditions generated by the large, localized Joule and Coulomb heating effects. This approach will permit the simulation of rapid temperature rise and return to ambient conditions, while isolating the material response to impulse thermal inputs.

- Many of the maximum service temperature values presented in the CES EduPack database are estimated ranges with variations of 15% to 35%. It may be better to use the melting temperature of the material, which is a directly measurable value.

However, one needs to be careful since there are other reasons, such as stability of the material in a particular environment that may limit the service temperature.

- An experimental procedure is needed to evaluate the wear under these extreme tribological and electrical contacts. Friction and wear are contact phenomena that are highly dependent on interfacial and environmental parameters.

- A high voltage arcing environment is responsible for much of the surface degradation present in extreme electrical contacts. A testing methodology to induce controlled arcing on the surface of a candidate material will reveal the materials resistance to this environment as well as provide a means of fundamentally characterizing this type of degradation.

References

[1] Fair, H., "Electric Launch Science and Technology in the United States," *IEEE Transactions on Magnetics,* VOL. 39, No. 1, 2003.

[2] Price, J.H, W. G. C. Fulcher, M.w. Ingram, D. E. Perkins, D. R. Peterson, R.C. Zowarka, and J.A. Pappas, "Design and Testing of Solid Armatures for Large-Bore Railguns," *Proceedings of the 4th Symposium on Electromagnetic Launch Technology,* No. Pr-66

[3] Bauer, D. and John Juston, "Rapid Testing for Multishot Railgun Bore Life," *IEEE Transactions on Magnetics,* VOL. 33, No. 1, 1997.

[4] Wang, L., "Modeling of the Armature-Rail Interface in an Electromagnetic Launcher with Lubricant Injection, Ph.D Dissertation, 2008.

[5] Challita A, B. Chelluri, D. Bauer, "Minimizing Non-Arcing Contact Material Deposition on Rails," *IEEE Transactions on Magnetics,* VOL. 31, No. 1, 1995.

[6] Llewellyn-Jones, F., "The physics of electrical contacts," *Clarendon Press,* 1957.

[7] Holm, R., "Electrical contacts: Theory and Application," *Springer*, 1967.

[8] Germer, L.H., "Physical processes in contact erosion," *J. Appl. Phys.,* VOL. 29, pp. 1067-1082, 1958.

[9] Argibay, N., J.A. Bares, W.G. Sawyer, "Asymmetric wear behavior of self-mated copper fiber brush and slip-ring sliding in a humid carbon dioxide environment," *Wear,* VOL. 268, pp. 455-463, 2010.

[10] Goodman, S., and Page, T., "The contact resistance and wear behaviour of separable electrical contact materials," *Wear,* VOL. 131, pp. 171-191, 1989.

[11] Reichner, P., "Metallic brushes for extreme current applications," *IEEE Trans.,* CHMT-3, pp. 21-25, 1980.

[12] Ashby, M.F., *Materials Selection in Mechanical Design*, 3rd Ed., Elsevier, 2005.

[13] Young, F. and W. Hughes, "Rail and armature current distributions in electromagnetic launcher," *IEEE Trans. Magn.,* VOL. 18, pp. 33-41, 1982.

[14] Parks, P., "Current melt-wave model for transitioning solid armature," *J. Appl. Phys.,* VOL. 67, pp. 3511-3516, 1990.

[15] Barber, J., and Dreizin, Y., "Model of contact transitioning with "realistic" armature-rail interfaces," *IEEE Trans. Magn.,* VOL. 31, pp. 96-100., 1995.

[16] Woods, L., "The current melt-wave model," *IEEE Trans. Magn.,* VOL.33, pp. 152-156, 1997.

[17] James, T. "Current wave and magnetic saw-effect phenomena in solid armatures," *IEEE Trans. Magn.,* VOL. 31, pp. 622-627, 1995.

[18] Benton, T., F. Stefani, S. Satapathy, and K. Hsieh, "Numerical modeling of melt-wave erosion in conductors," *IEEE Trans. Magn.,* VOL. 39, pp. 129-133, 2003.

[19] Merrill, R. and F. Stefani, "Electrodynamics of the current melt-wave erosion boundary in a conducting half-space," *IEEE Trans. Magn.,* VOL. 39, pp. 66-71, 2003.

[20] Granta Design Limited. CES EduPack 2009 [computer software]. Cambridge, United Kingdom.

[21] Subramanian, P.R. and D.E. Laughlin, "Cu-W (Copper-Tungsten)," Phase Diagrams of Binary Tungsten Alloys. Edited by S.V. Nagender Naidu and P. Rama Rao, Indian Institute of Metals, Calcutta, pp. 76-79, 1991.

[22] Subramanian, P.R. and D.E. Laughlin, "The Cu-Ta (Copper-Tantalum) System,"*Bulletin of Alloy Phase Diagrams*, pp. 652-655, VOL. 10, 1989.

[23] Subramanian, P.R. and D.E. Laughlin, "The Cu-Mo (Copper-Molybdenum) System, *Bulletin of Alloy Phase Diagrams,* pp. 169-172, VOL. 11, 1990.

[24] Povov, I.A., and N.V. Shiryayeva, "State Diagram of the System Nb-Cu," VOL. 6 No. 10, pp. 2334-2340, 1961.

[25] Bandyopadhyay, N. R., S. Ghosh, and A. Basumallick, "New Generation Metal Matrix Composites," *Materials and Manufacturing Processes,* VOL. 22, 2007.

[26] Kaczmar, J.W., K. Pietrzak, W. Wlosinski, "The production and application of metal matrix composite materials," *Journal of Materials Processing Technology,* VOL. 106, 2000.

[27] Slipenyuk, A., V. Kuprin, Yu. Milman, V. Goncharuk, J. Eckert, "Properties of P/M processed particle reinforced metal matrix composites specified by reinforcement concentration and matrix-to-reinforcement particle size ratio," *Acta Materialia,* VOL. 54, 2006.

[28] Li, S. B., J. X. Xie and Z. Y. Zhao, "Fabrication of ultrafine W–Cu powders by Mechanical Alloying," *Materials Science and Technology*, VOL.. 20, 2004.

[29] Clyne, T.W., "An Introduction to Metal Matrix Composites," *Cambridge University Press,* 1993.

[30] Jankovic, D., J. Fiscina, C. J. R. Gonzalez-Oliver, N. Ilic, F. Mucklich, "Electrical and elastic properties of Cu-W graded material produced by vibro compaction," *Journal of Material Science,* VOL. 43, pp. 6777-6783, 2008.

[31] Liu, B-B., J-X Xie, X-H Qu, "Fabrication of W-Cu functionally graded materials with high density by particle size adjustment and solid state hot press," *Composites Science and Technology,* VOL. 68, pp. 1539-1547, 2008.

[32] Slipenyuk, A., Kuprin, V., Milman, Yu., Goncharuk, V., Eckert, J., "Properties of P/M processed particle reinforced metal matrix composites specified by reinforcement concentration and matrix-to-reinforcement particle size ratio," *Acta Materialia,* VOL. 54, 2006.

[33] Liao, T-T., C. Kung, "High-temperature mechanical and electrical properties of W-particle-reinforced Cu-matrix composites from improved electroless plated powders," *Journal of Mechanical Engineering Science,* VOL. 223, pp. 1285-1295, 2009.

[34] Zhang, J., L. He, and Y. Zhou, "Highly conductive and strengthened copper matrix composite reinforced by Zr2Al3C4 particulates," *Scripta Materiallia,* VOL. 60, pp. 976-979, 2009.

[35] Wang, C., Min, G., Kang, S-B, "The microstructure and mechanical properties of SiCp-reinforced Copper matrix composites by hot pressing," *J. of Comp. Mater.,* VOL. 44, pp. 347-354, 2010.

[36] Moustafa, S.F., Abdel-Hamid, Z., Adb-Elhay, A.M., "Copper matrix SiC and Al_2O_3 particulate composites by powder metallurgy technique," *Materials letters,* VOL. 53, pp. 244-239, 2002.

[37] Ivănuş, R., "Effect of processing parameters, particle characteristics and metallic coating on properties of SiCp Copper alloy matrix composites," *Mater. and Tech.*, 2007.

[38] Du, J., Hoschen, T., Rasinski, M., You, J.-H., "Interfacial fracture behavior of tungsten wire/tungsten matrix composites with copper-coated interfaces," *Materials Science and Engineering A,* VOL. 527, pp. 1623-29, 2010.

[39] Davidson, A.M., Regener, D., "A comparison of aluminum-based metal-matrix composites reinforced with coated and uncoated particulate silicon carbide," *Composites Science and Technology*, VOL. 60, 2000.

[40] Chang, S.Y., Lin, S. J., "Fabrication of SiC$_w$ Reinforced Copper Matrix Composite By Electroless Copper Plating," Scripta Materialla, VOL.. 35, pp. 225-231, 1996.

[41] Korthäuer, M. Ataya, S., Salem, A., El-Magd, E., "Size effects of the deformation beaviour of W-Cu Composites under shear loading," *Comp. Mat. Sci.,* VOL.. 39, pp. 219-223, 2007.

[42]. López, A., Corredor, D., Ramam, K., Jiménez, J. A., and Ruano, O., "Performance of new dispersion-precipitation strengthened copper-ceramic materials made by mechanical alloying," *Phys. Stat. Sol.,* VOL. 11, 2007.

[43] Eisenmenger-Sittner, C., Schrank, C., Neubauer, E.,. Eiper, E, Keckes, J., "Modification of wetting of copper (Cu) on carbon (C) by plasma treatment and molybdenum (Mo) interlayers," Applied *Surface Science* VOL. 252, 2006.

[44] Schwarz, B., Schrank, C., Eisenmenger-Sittner, C., Stoger-Pollach, M., Rosner, M., Neubauer, E., "Molybdenum interlayers as adhesion promoters for thin copper films on plasma treated glassy carbon," *Surface & Coatings Technology*, VOL. 200, 2006.

[45] Wu, T.F., Lee, S.L., Chen, M.H., Li, Z.G., Lin, J.C., "Effects of tungsten carbide and cobalt particles on corrosion and wear behavior of copper matrix composite," *Inst. of Materials, Minerals and Mining,* 2005.

[46] Trueman, A.R., Schweinsberg, D.P., Hope, G.A., "A study of the effect of cobalt additions on the corrosion of tungsten carbide/carbon steel metal matrix composites," *Corros. Sci.,* VOL. 41, pp. 1377-1389, 1999.

[47] Köck, T., Brendel, A., Bolt, H., "Interface reactions between silicon carbide and interlayers in silicon carbide-copper metal-matrix composites," *J. of Nuclear Mat.,* VOL. 362, pp. 197-201, 2007.

[48] Wang, Yu-Cling and Ben-Lian Zhou, "Behaviour of coatings on reinforcements in some metal matrix composites," *Composites Part A*, VOL. 27A, 1996.

[49] Voigt, W., "Numerical relation between the two elasticity constants of isotropic substances according to the molecular theory," *Annalen der Physik,* VOL. 4, pp. 187-196, 1901.

[50] Ledbetter, H.M., Datta, S. K., "Young's modulus and the internal friction of an SiC-Particle-Reinforced Aluminum Composite." *Mat. Sci. Engr.* VOL. 67, pp 25-30, 1984

[51] Hashin, Z., "Analysis of composite materials—a survey." *J. Appl. Mech.,* VOL. 50, pp. 481-505, 1983.

[52] Paul, B. "Prediction of Elastic Constants of Multiphase Materials," *Transactions of the ASME,* VOL. 218, pp. 36-41, 1960.

[53] Walpole L.J., "On bounds for the overall elastic moduli of inhomogeneous systems," *Journal of Mech. Phys. Solids*, VOL. 14, pp. 151-162; 289-301, 1966.

[54] Hashin Z., S. Shtrikman, "A variational approach to the theory of the elastic behaviour of multiplephase materials," *Journal of Mechanical Physics,* VOL. 11, pp. 127-140, 1963.

[55] Hashin Z., S. Shtrikman, "On some variational principles in Anisotropic and Nonhomogeneous and Elasticity,"*Journal of the Mechanics and Physics of Solids,* VOL. 10, pp. 335-342, 1962.

[56] Ansell, G.S., Lenel, F.V., "Criteria for Yielding of Dispersion-Strengthened Alloys," *Acta Metallurgica,* VOL. 8, pp. 612-616, 1960.

[57] Ochiai, S., "Mechanical Properties of Metallic Composites," Marcel Dekker, 1993.

[58] Nadkarni, A.V., "Dispersion Strengthened Copper – Properties and Applications,"

[59] Orwan, E., *Symposium on internal Stresses in Metals and Alloys,* Inst. of Metals, London 1948.

[60] Orwan, E., *Dislocations in Metals,* Am. Inst. of Mining, Met. and Petrol. Eng., New York 1954.

[61] Tjong, S. C., "Novel Nanoparticle-Reinforced Metal Matrix Composites with Enhanced Mechanical Properties," *Adv. Eng. Mat.,* VOL. 9, pp. 639-652, 2007.

[62] Hull, D, and T.W. Clyne, "An introduction to composite materials," Cambridge University Press, Cambridge, UK, 1996.

[63] Zhao, M, L. Zhu, Y. Liu, "A Simple Model to Estimate the Yield Strength of Silicon Carbide Particulate Reinforced Aluminum Alloy Matrix Composites," *J. Mater. Sci. Techno.l*, VOL. 18, No.3, pp. 193-194, 2002.

[64] Varma, V., Y.R. Mahajan, V.V. Kutumbarao, "Ageing behaviour of Al-Cu-Mg alloy matrix composites with SiC_p of varying sizes," *Scripta Metall. Mater.*, VOL. 37, pp. 485-489, 1997.

[65] Bao, G., J.W. Hutchinson, R.M. McMeeking, "Particle Reinforcement of Ductile Matrices Against Plastic Flow and Creep," *Acta Metall. Mater.*, VOL. 39, pp. 1871-1882, 1991.

[66] Majumdar, B.S., A. B. Pandey, "Deformation and Fracture of a Particle-Reinforced Aluminum Alloy Composite: Part II. Modeling,"*Metallurgical and Materials Transactions A,* VOL. 31A, pp. 937-950, 2000.

[67] Irwin, G. R., "Fracture Dynamics," *Fracturing of Metals,* ASM, pp. 147-166, 1948.

[68] Chermant, J. L., Osterstock, F., "Fracture toughness and fracture of WC-Co composites," *J. Mater. Sci.,* VOL. 11, pp. 1939-1951, 1976.

[69] Wahi, R. P., B. Ilschner, "Fracture behaviour of composites based on Al_2O_3-TiC," *J. Mater. Sci.,* VOL. 15, pp. 875-885, 1980.

[70] Rice, J.R., Johnson, M.A., "The Role of Large Crack Tip Geometry Changes in Plane Strain Fracture," *Inelastic Behaviour of Solids,* McGraw-Hill, New York, pp. 641-672, 1970.

[71] Hahn, G.T., A.R. Rosenfield, "Metallurgical Factors Affecting Fracture Toughness of Al Alloys," *Metall. Trans.,* VOL. 6A, pp. 653-670, 1975.

[72] Sapate, S.G., A. Uttarwar, R.C. Rathod, R.K. Paretkar, "Analyzing dry sliding wear behaviour of copper matrix composites reinforced with pre-coated SiC_p particles," *Materials and Design,* VOL. 30, pp. 376-386, 2009.

[73] Khruschov, M.M., and M.A. Babichev, "Resistance to abrasive wear of structurally heterogeneous materials," *Friction Wear Mach.*, VOL. 12, pp. 5-24, 1958.

[74] Zum-Gahr, K.H., "Abrasive wear of two-phase metallic materials with a course microstructure," K.C. Ludema (Ed.), International Conference on Wear of Materials, *American Society of Engineering,* p. 793, 1985.

[75] Lee, G.Y., C.K.H. Dharan, R.O. Ritchie, "A physically-based abrasive wear model for composite materials," *Wear*, VOL. 252, pp. 322-331, 2002.

[76] Bhansali, K.J., R. Mehrabian, "Abrasive wear of aluminum-matrix composites," *J. Metals,* VOL. 34, 1982.

[77] Stauffer, D., A. Aharony, Introduction to Percolation Theory, 2nd Ed., Taylor & Francis, London, 1992.

[78] McLachlan, D.S., M. Blaskiewicz, R.E Newnham, "Electrical Resistivity of Composites," *J. Am. Ceram. Soc.,* VOL. 73, pp. 2187-2203, 1990.

[79] Kovacik, J., "Electrical conductivity of two-phase composite material," *Scripta Materialia,* VOL. 2, pp. 153-157, 1998.

[80] Landauer, "Electrical transport and optical properties of inhomogeneous media," *AIP Conf. Proc.,* VOL. 40 p.2, AIP, New York, 1978.

[81] Bruggeman, D.A.G., "Calculation of various physical constants of heterogeneous substances," *Ann. Phys.* VOL. 24, p. 636, 1935.

[82] Isichenko, M.B., "Percolation, statistical topography, and transport in random media," *Rev. Mod. Phys.,* VOL. 64, p. 961, 1992.

[83] Zhang, J., L. He, Y. Zhou, "Highly conductive and strengthened copper matrix composites reinforced by Zr2Al3C4 particulates," *Scripta Materialia*, VOL. 60, pp. 976-979, 2009.

[84] Fan, Z., "A New Approach to the Electrical Resistivity of Two-Phase Composites," *Acta Metall. Mater*, VOL. 43, pp. 43-49, 1995.

[85] Werner, E. and H.P. Stuwe, "Phase boundaries as obstacles to dislocation motion," *Mater. Sci. Engng.*, VOL. 68, pp. 175, 1984.

[86] Chang, Shou-Yi, Chi-Fang Chen, Su-Jien Lin a, Theo Z. Kattamis, "Electrical resistivity of metal matrix composites," *Acta Materialia,* VOL. 51, pp. 6291-6302, 2003.

[87] Arsenault, R.J., Shi, N., "Microstructure of fiber and particulate metal matrix composites," *Scripta Metall.,* VOL. 17, p. 67, 1983.

[88] Arsenault, R.J., Shi, N., "Dislocation generation due to differences in coefficients of thermal expansion," *Mater. Sci. Eng.,* VOL. 81, p. 175, 1986.

[89] North American Electrical Components, LLC (NAECO), Peachtree City, Georgia, personal communication, 2010.

[90] Granta Design Limited. CES EduPack 2010 [computer software]. Cambridge, United Kingdom.

[91] Hull, D.,"Fractography: observing, measuring, and interpreting fracture surface topography," *Cambridge University Press,* 1999.

[92] Cleveringa, H.H.M., E. Van Der Giessen, A. Needleman, "Comparison of discrete dislocation and continuum plasticity predictions for a composite material," *Acta. Mater.,* VOL. 45, pp.3163-3179, 1997.

[93] Hayt, W., "Engineering Electromagnetics", *McGraw Hill,* 2006.